






α -Parvin Defines a Specific Integrin Adhesome to Maintain the Glomerular Filtration Barrier

Manuel Rogg ¹, Jasmin I. Maier ¹, Clara Van Wymersch,¹ Martin Helmstädter,² Alena Sammarco,¹ Maja Lindenmeyer,³ Paulina Zareba,¹ Eloi Montanez ⁴, Gerd Walz,² Martin Werner,¹ Nicole Endlich ^{5,6}, Thomas Benzing,⁷ Tobias B. Huber ³ and Christoph Schell^{1,8}

Due to the number of contributing authors, the affiliations are listed at the end of this article.

ABSTRACT

Background The cell-matrix adhesion between podocytes and the glomerular basement membrane is essential for the integrity of the kidney's filtration barrier. Despite increasing knowledge about the complexity of integrin adhesion complexes, an understanding of the regulation of these protein complexes in glomerular disease remains elusive.

Methods We mapped the *in vivo* composition of the podocyte integrin adhesome. In addition, we analyzed conditional knockout mice targeting a gene (*Parva*) that encodes an actin-binding protein (α -parvin), and murine disease models. To evaluate podocytes *in vivo*, we used super-resolution microscopy, electron microscopy, multiplex immunofluorescence microscopy, and RNA sequencing. We performed functional analysis of CRISPR/Cas9-generated *PARVA* single knockout podocytes and *PARVA* and *PARVB* double knockout podocytes in three- and two-dimensional cultures using specific extracellular matrix ligands and micropatterns.

Results We found that *PARVA* is essential to prevent podocyte foot process effacement, detachment from the glomerular basement membrane, and the development of FSGS. Through the use of *in vitro* and *in vivo* models, we identified an inherent *PARVB*-dependent compensatory module at podocyte integrin adhesion complexes, sustaining efficient mechanical linkage at the filtration barrier. Sequential genetic deletion of *PARVA* and *PARVB* induces a switch in structure and composition of integrin adhesion complexes. This redistribution of these complexes translates into a loss of the ventral actin cytoskeleton, decreased adhesion capacity, impaired mechanical resistance, and dysfunctional extracellular matrix assembly.

Conclusions The findings reveal adaptive mechanisms of podocyte integrin adhesion complexes, providing a conceptual framework for therapeutic strategies to prevent podocyte detachment in glomerular disease.

JASN 33: 786–808, 2022. doi: <https://doi.org/10.1681/ASN.2021101319>

The glomerular filtration barrier is organized as a three-layered filter, consisting of endothelial cells, the glomerular basement membrane (GBM), and specialized epithelial cells, named podocytes.^{1,2} Detachment of podocytes from the GBM has been identified as an unifying pathogenic motif in various glomerular pathologies.^{3,4} These observations and insights from genetic glomerular disease have initiated research to decipher the role of podocyte cell-matrix interactions in health and disease.^{5,6} Given the evolving complexity of the integrin *adhesome*,^{7–9} it is not completely clear how individual components of this multiprotein

Received August 10, 2021. Accepted January 17, 2022.

Published online ahead of print. Publication date available at www.jasn.org.

Correspondence: Dr. Christoph Schell, Institute of Surgical Pathology, University Medical Center Freiburg, Breisacherstr. 115a, D-79106 Freiburg, Germany. Email: christoph.schell@uniklinik-freiburg.de

Copyright © 2022 by the American Society of Nephrology

complex contribute to contextual signal integration and adaptive responses to ensure physiologic homeostasis.

Integrin-based heterodimeric adhesion molecules represent one of the largest classes of cell-matrix adhesion receptors. A multitude of adaptor, kinase, and linker molecules are recruited to the intracytoplasmic integrin portion, commonly termed as the integrin *adhesome*.¹⁰ Interestingly, mutations in either core (*ITGA3*) or *adhesome*-associated (*CD151*, *ACTN4*) genes have been identified as disease-associated mutations, prominently affecting podocyte function, resulting in severe glomerular pathologies.^{11–13} Using cell-type-specific proteomics and transcriptome analysis, we and others expanded the knowledge about prototypical adhesion receptor proteins within specialized glomerular cell types.^{14–18} These studies contributed to a concept of balanced reciprocal crosstalk between the *adhesome* and GBM composition.^{17,19} Podocytes are characterized by a highly complex cytomorphological architecture with arborizing cellular protrusions (commonly termed podocyte foot processes; FPs).^{19,20} Functional and genetic studies highlighted the relevance of titrated cytoskeletal activity and composition to ensure FP morphology and plasticity.^{21–23} One concept proposes that adaptive responses require a well-balanced interplay between cytoskeletal and *adhesome* components to ensure efficient mechano-transductive capacity. Previous work already described the pseudo-kinase integrin-linked kinase (ILK) as a component of the podocyte *adhesome*, and demonstrated the effect of *ILK* deficiency on GBM structure and podocyte differentiation.^{24,25} Recent *in vivo* and *in vitro* data confirmed that ILK instead exerts more structural scaffolding functions than the previously claimed direct kinase properties.^{26–28} ILK is recruited to integrin-based adhesion complexes (IACs) in a ternary complex consisting of Pinch and Parvin proteins (IPP complex). Parvin proteins (α , β , γ) interact with other *adhesome* proteins (including the IPP complex) and contain an actin-binding domain facilitating actin filament recruitment toward IACs.^{29–31} Global genetic deletion of *Parvin- α* (*Parva*) resulted in embryonic lethality.²⁸

In this study, we identify the IPP component α -parvin (PARVA) as a central modulator of podocyte mechano-transductive signaling. We demonstrate that PARVA is essentially required for efficient podocyte cell-matrix adhesion and that inherent compensation within the IPP complex is involved in podocyte extracellular matrix (ECM) contextual responses. These observations provide the framework for a concept of cell-type-specific inherent *adhesome* modulation for adaptive signal integration in health and disease.

METHODS

Animals

Conditional *Parva* knockout (KO) mice (*Parva*^{fl/fl}**hNPHS2Cre*) were generated by intercrossing of a previously described

Significance Statement

Although podocyte detachment is a well-established factor driving the progression of glomerular kidney diseases, the underlying mechanisms initiating podocyte loss remain elusive. In particular, the co-occurrence of podocyte detachment and adaptive reinforcement of the actin cytoskeleton and integrin adhesion complexes presents a conundrum. The authors provide a comprehensive map of the podocyte adhesome and identify an actin-binding adhesome protein, α -parvin (PARVA), as a podocyte-specific mechanical linker. By employing a complementary approach involving both *in vivo* and *in vitro* models, they demonstrate that PARVA prevents podocyte detachment via mechano-adaptive remodeling of adhesion complexes. These observations suggest that insufficient linkage of a tensile actin cytoskeleton to integrin adhesion complexes is a causative mechanism in podocyte detachment in glomerular diseases.

conditional allele for *Parva* (*Parva*^{fl/fl}, generously provided by E. Montanez, University of Barcelona, Spain³²) with a podocyte-specific *Cre* line (generously provided by L. Holzman, University of Pennsylvania, School of Medicine, Philadelphia, USA³³). The Gt(ROSA)26Sortm4(ACTB-tTomato,-EGFP)Luo/J (*mT/mG*) reporter strain was purchased from JAX mice and crossed to *hNPHS2Cre* mice for isolation of primary podocytes. Respective colonies were maintained on a C57BL/6 mixed background. Animal models for nephrotoxic serum nephritis, *Epb4115*^{fl/fl}**Nphs1-rtTA-3G*tetOCre*, and *Nphs2*^{R231Q/A286V} were generated and described previously.^{34–36} All mouse experiments were performed according to the National Institutes of Health Guide for the Care and Use of Laboratory Animals, and the German law governing the welfare of animals. All studies were approved by the Regierungspräsidium Freiburg (G-17/127), Germany.

Cell Culture

Human immortalized podocytes (AB8/13) were generously provided by Moin A. Saleem, Bristol University, United Kingdom.³⁷ Isolation of primary podocytes with genetically proven origin from *Parva*^{fl/fl}**mT/mG***hNPHS2Cre* and *Parva*^{wt/wt}**mT/mG***hNPHS2Cre* reporter mice was performed as described before.²¹ Podocytes were cultured in RPMI 1640 cell culture medium, supplemented with Glutamine (Thermo Fisher Scientific, 61870036), 10% FCS (Sigma-Aldrich, S0615), 10 μ g/ml ITS (Sigma-Aldrich, 11074547001), 5 mM HEPES (Thermo Fisher Scientific, 15630–056), nonessential amino acids (MEM NEAA, Thermo Fisher Scientific, 11140050) 1:1000, 0.1 mM sodium-pyruvate (Thermo Fisher Scientific, 11360–039), and penicillin-streptomycin (Thermo Fisher Scientific, 15140122), according to standard human immortalized podocyte culture procedures at 33°C, 95% air, and 5% CO₂.³⁸ Human immortalized podocytes were cultured at 37°C for 8–10 days before seeding into the respective experiments. All functional experiments using podocyte cell lines were performed at 37°C. Primary podocytes were

maintained at 37°C. Cells were tested negative for mycoplasma contamination on a regular basis by PCR (*Mycoplasma* PCR Detection kit, Hiss Diagnostics GmbH, Germany) and by Hoechst 33258 staining.

Antibodies

Antibodies used in this study are described in detail in Supplemental Table 1.

CRISPR/Cas9 Genome Editing

For generation of *PARVA* and *PARVA/PARVB* double KO (dKO) cells, the CRISPR/Cas9 genome editing technology was applied on human immortalized podocytes, as described before.³⁸ Single guide RNAs targeting exons of the human *PARVA* or *PARVB* gene were designed using the web-based platform CHOPCHOP³⁹: *PARVA* sgRNA-1: 5'- ATGGTC-GAACAAGGTGTCAA(AGG) -3', *PARVA* sgRNA-2: 5'- CTGGGAGTCGAATTGGTGCG(CGG) -3', *PARVA* sgRNA-3: 5'- GTCTGGGGCATGGTGAACA(AGG) -3', *PARVA* sgRNA-4: 5'- CTTGGATTTGCCGAGACTGG(AGG) -3', *PARVB* sgRNA-1: 5'- GCACGTCATTAATCCAGTCC(AGG) -3', *PARVB* sgRNA-2: 5'- GATCGAAGCTTTCCGGAGT-C(AGG) -3'. gRNAs were cloned in a modified lentiCRISPRv2 plasmid (TLCV2), which was a gift from Adam Karpf (Addgene plasmid 87360; <http://n2t.net/addgene:87360>; RRID:Addgene_87360).⁴⁰ Control (wild-type; WT) clones were generated by using TLCV2 plasmids without gRNA sequence or nontargeting (nt) sequences (nt-sgRNA-1: 5'- GCGGGCAGAACGACCCCTGAC -3', nt-sgRNA-2: 5'- GAA-GACGTGCTGGCGTCACC -3').⁴¹ Lentiviral particles were produced in HEK293T cells according to standard procedures. Podocytes were transduced with lentiviral particles, followed by puromycin selection and doxycycline induction for 4 days. Single-cell clones were generated, screened for loss of *PARVA* and *PARVB* expression, and validated by western blot and immunofluorescence (IF) analysis. Monoclonal podocyte cell lines were generated from the polyclonal parental cell line and evaluated for differentiation capability (growth arrest, morphology), population-doubling time and podocyte cobblestone morphology. This monoclonal background was used for generation of *PARVA* WT-2 (nt-sgRNA-1), WT-3 (nt-sgRNA-2), KO-2 (*PARVA* sgRNA-3), KO-3 (*PARVA* sgRNA-3), and KO-4 (*PARVA* sgRNA-4) cell lines. In addition, the *PARVA* WT-1 (lentiCRISPRv2 without gRNA) cell line represents the polyclonal podocyte population and the *PARVA* KO-1 (*PARVA* sgRNA-1) clone was independently generated from this polyclonal background. The *PARVA* KO-2 cell line was transduced with nt-gRNA1&2 or *PARVB* gRNA1&2 to generate *PARVA* and *PARVB* dKO clones (dKO-1/-2/-3) or *PARVA* single KO (sKO-2) podocytes as control.

Expression Plasmids

The mEmerald-Parvin-C-14 plasmid was a gift from Michael Davidson (Addgene plasmid, 54214; <http://n2t.net/>

addgene:54214; RRID: Addgene 54214). Human *PARVB*. pcDNA3.1+/C-(K)-DYK plasmids for *PARVB* transcript variant 1 (*PARVB* *tv1*; NM_001003828.2) and transcript variant 3 (*PARVB* *tv-3*; NM_001243385.1) were purchased from GeneScript (Hu22058 and Hu12475). *PARVA* and *PARVB* cDNAs were subcloned into a Flag-tagged or untagged pWPXLd plasmid, which was a gift from Didier Trono (Addgene plasmid, 12258; <http://n2t.net/addgene:12258>; RRID: Addgene_12258). The FLAG.pWPXLd plasmid was used as negative control for FLAG-*PARVA*. pWPXLd and an empty pWPXLd plasmid for *PARVB*-*tv1*. pWPXLd and *PARVB*-*tv3*.pWPXLd. Lentiviral transduction of podocytes was performed according to standard procedures and protein expression was validated by western blot and IF analysis.

Western Blot Analysis

Whole-cell lysates were generated by cell lysis in RIPA buffer at 4°C for 15 minutes. Lysates were cleared by centrifugation at 16,000 g and 4°C for 15 minutes. After clearing, supernatants were mixed with Laemmli buffer (2×) with dithiothreitol, and denaturation was performed at 95°C for 5 minutes. Protein concentration was measured using the Pierce BCA Protein Assay Kit (23225, Thermo Fisher Scientific), following the manufacturer's instructions. Equalized amounts of protein were loaded and separated by SDS-PAGE, following standard procedures. Western blotting was performed using the Trans-Blot Turbo Transfer System (BioRad) and appropriate polyvinylidene difluoride membranes (1704157, BioRad). Membranes were blocked in 5% BSA in Tris-buffered saline with Tween-20 (TBST) and primary antibodies (Supplemental Table 1) were diluted in TBST and incubated on membranes for 24 hours at 4°C. After washing in TBST, secondary HRP-linked antibodies (Supplemental Table 1) were applied for 1 hour. The HRP/ECL chemiluminescence detection method (32109, Thermo Fisher Scientific) in combination with a chemiluminescence imager was used for digital signal acquisition. Densitometry and quantification of blot bands from independent replicates was performed using Fiji ImageJ v1.52.

Scanning Electron Microscopy and Transmission Electron Microscopy Procedures

Preparation of kidney samples for transmission electron microscopy (TEM) and scanning electron microscopy (SEM) were essentially performed as previously described.³⁸ After perfusion and fixation (4% paraformaldehyde (PFA) + 1% glutaraldehyde in PBS for 24 hours at 4°C), samples were stored in 0.1 M sodium cacodylate buffer at 4°C until analysis. TEM samples were postfixed in 0.5% osmium tetroxide in ddH₂O for 60 minutes on ice, and washed six times in ddH₂O. The tissue was incubated in 1% uranyl acetate in ddH₂O at room temperature for 2 hours. Dehydration was performed by 15-minute incubations in

increasing concentrations of EtOH and finally acetone. After embedding in Durcupan resin, ultrathin sections were generated using a UC7 Ultramicrotome (Leica), collected on Formvar-coated copper grids. Imaging was conducted using a Zeiss Leo 912 transmission electron microscope. Embedding, semithin sectioning, and electron microscopy was performed at the EM core facility of the Department of Nephrology, Faculty of Medicine, University of Freiburg. TEM images were analyzed for FP width and GBM thickness (FP to endothelial cell distance) using Fiji ImageJ v1.52, as previously described.³⁵ For SEM, small tissue cubes were prepared and immersion fixed in 4% PFA and 1% glutaraldehyde in PBS for 3 days. Further dehydration was performed in ethanol (50%–100%, each 10% step for 1 hour at room temperature), and subsequently transferred to hexamethyldisilazan (Sigma, Schnellendorf, Germany). Gold sputtering was performed employing a Polaron Cool Sputter Coater E 5100. Samples were imaged using a scanning electron microscope (Leo 1450 VP scanning). SEM was performed at the EM core facility of the Department of Nephrology, Faculty of Medicine, University of Freiburg.

Microscopy

IF stainings were imaged using an inverted Zeiss Axio Observer microscope equipped with an Colibri 7 illumination system, Axiocam 702 mono camera, ApoTome.2 device, scanning stage, 100×, 63×, 40×, 20×, and 10× objectives, and 49 DAPI, 38 GFP, 43 HE dsRed, and 50 Cy5 filter sets (Carl Zeiss AG). Z-stacks were converted to maximum intensity projections using the ZEN software (ZEN 2012 SP1, Carl Zeiss AG). For iterative indirect IF imaging (4i), the scanning stage was used for sample positioning and repetitive imaging. For analysis of immunohistochemistry (IHC) and histology an inverted Zeiss Axio Imager microscope equipped with an Axiocam color and 40×, 63×, 100× objective and a Ventana DP 200 slide scanner (Roche Diagnostics Deutschland GmbH, Mannheim, Germany) equipped with a 20× and a 40× objective was used.

Histology

Preparation and processing of tissue samples, formalin fixation, paraffin embedding, and microtome sectioning were performed using standardized procedures at the Institute of Surgical Pathology, Faculty of Medicine, University of Freiburg. Mouse kidneys were fixed by 4% PFA in PBS after direct perfusion *via* the renal arteries, followed by further immersion fixation for 24 hours at 4°C.

For IF staining procedures, 2 µm sections of FFPE-tissue were generated, deparaffinized, rehydrated, and underwent established heat-induced antigen retrieval (HIAR; pressure cooker, 5 or 10 minutes, depending on the individual epitope, Supplemental Table 1). Blocking of sections was performed in 5% BSA in PBS for 1 hour, followed by primary

antibody incubation in blocking solution for 24 hours. Subsequently, sections were washed in PBS and secondary fluorophore-tagged antibodies (Alexa Fluor Dyes, Thermo Fisher Scientific Inc.) were added for 45 minutes (in blocking solution). Hoechst 33342 staining was used for the visualization of nuclei (Thermo Fisher Scientific). ProLong Gold Antifade solution was used for final embedding (Thermo Fisher Scientific).

Samples for IHC were sectioned and processed as described for IF (except for performing additional peroxidase blocking for 15 minutes using 1% H₂O₂ after HIAR). HRP-linked secondary antibodies (Dako) were applied for 30 minutes in blocking solution. Visualization and staining were performed using the DAB+ Substrate Chromogen System (Dako) including counterstaining with hematoxylin. After dehydration, slides were mounted using Entellan.

Histology of FFPE-tissue sections was performed from deparaffinized sections. Periodic acid–Schiff reaction was performed by the Department of Pathology, Faculty of Medicine, University of Freiburg, according to standard procedures.

Histologic Assessment (Glomerular Sclerosis and Tubulointerstitial Damage)

Assessment of structural damage has been performed by applying semiquantitative scoring schemes on fully digitized whole slide image data. Level and extent of glomerular sclerosis was scored by employing a five-tiered score (0–4) as previously described.⁴² A minimum of 50 glomeruli per animal were analyzed and mean glomerular sclerosis score per animal was calculated. Interstitial fibrosis and tubular atrophy were assessed applying a four-tiered scoring system (0–3; 0, <5%; 1, 6%–25%; 2, 26%–50%; 3, >50%) adapted and on the basis of previously described approaches.^{43,44} Similar grading schemes were used for the assessment of interstitial immune cell infiltrates. At least four animals per genotype and time point were analyzed.

Quantification of Glomerular Podocytes

Estimation of glomerular podocytes was performed according to standard protocols.⁴⁵ Kidney sections were stained for NPHS1, WT1, and Hoechst 33342, as described above. Glomerular cells with positivity for NPHS1 and WT1 were identified as podocytes. In addition, tuft areas and nuclei diameter were measured using Fiji ImageJ v1.52. Podocyte numbers per tuft area and glomerulus were calculated (≥ 20 glomeruli per animal were analyzed). Detachment into the urine was additionally visualized by WT1 staining of urinary SDS-PAGE blots. Urine samples were balanced according to respective creatinine concentration, mixed with 2x Laemmli buffer and heat denatured (5 minutes at 95°C). SDS-PAGE was performed as described above.

In vivo Quantification of Podocyte IAC Components

IF staining of individual IAC components was performed as described above. Kidney samples used for IF quantification were processed in parallel (including preparation, fixation, staining, and imaging) to ensure comparability. NPHS1 was used as a podocyte compartment marker for subsequent image analysis and segmentation using Fiji ImageJ v1.52. In brief, threshold levels were applied on NPHS1 IF signals to obtain a segmentation mask of the podocyte compartment for individual glomeruli. Mean fluorescence intensities (MFIs) of IAC components and NPHS1 were measured and acquired within this mask. In addition, line scan profiles of representative capillaries were measured for FERMT2-ILK and ITGB1-ILK costaining. The Duolink in situ Orange Starter Kit (Sigma-Aldrich) was used for proximity ligation assay (PLA), according to the manufacturer's instructions. For PLA quantification, NPHS1 staining was used for further segmentation and the number of PLA positive dots was automatically counted within this mask of the podocyte compartment. At least 20 glomeruli per animal and marker were analyzed for mean fluorescence intensities of IAC components and 10 glomeruli for line scan analysis.

Super-resolution Microscopy (Podocyte Exact Morphology Measurement Procedure)

The evaluation of the filtration slit density was performed using a recently established super-resolution microscopy-based methodology (structured illumination microscopy, SIM; N-SIM [Nikon] with a 100 \times objective) termed as podocyte exact morphology measurement procedure (PEMP).²¹ The three-dimensional (3D) SIM (z-stack) images of slit diaphragms were colorized according to their position on the z axis. Filtration slit density values of 20 glomeruli in three mice per group were quantified.

Multiplex IF Staining and Imaging

The tyramide signal amplification based Opal detection method was used for IF staining of human kidney biopsy samples (Opal Polaris 7-Color Automation IHC Kit; Akoya Biosciences, Marlborough, MA, USA). Optimal Opal-antibody pairs were on the basis of previously optimized protocols in *uniplex* IF staining. Retrieval, primary antibody application, and detection with Opal fluorophores were performed according to the manufacturer's instructions. In brief, slides underwent standardized antigen retrieval after prior deparaffinization (Tris-EDTA buffer, pH 9). After further blocking, primary antibody incubations were performed for between 30 minutes and 1 hour, or overnight depending on individual antibodies (on the basis of previous establishment in uniplex staining). Incubation with tyramide signal amplification dyes (10 minutes) was performed after further washing (Opal 7 kit: Opal 480, Opal 520, Opal 570, Opal 620, Opal 690, and Opal 780).

Slides were counterstained with DAPI and mounted with ProLong Gold Antifade. Image acquisition was performed on a Vectra Polaris scanner (Akoya Biosciences, Marlborough, MA, USA) using 40 \times magnification and the implemented MOTiF scan. Further visualization and image analysis was performed on the Phenochart Version 1.1.0 software (Akoya Biosciences, Marlborough, MA, USA). Use of human kidney biopsy and tumor nephrectomy samples was granted by local ethics committee (Ethikkommission, Universitätsklinikum Freiburg) under the license EK512/18.

Iterative Indirect IF Imaging on Formalin-Fixed Paraffin-Embedded Tissue Sections

Iterative indirect IF imaging (4i) is a multiplex imaging technique recently developed by Gut *et al.* for *in vitro* samples.³⁹ We have previously adapted this technique for multiplex staining of 2 μ m formalin-fixed paraffin-embedded (FFPE) tissue sections, following the published protocol. In brief, FFPE tissue was sectioned, transferred on high precision microscopy glass slides (Ibidi, 10812), and processed for IF staining, as described above. HIAR was performed in Tris-EDTA buffer at pH 9 using a pressure cooker for 10 minutes. After HIAR, a staining/imaging chamber (Ibidi, 80828) was attached to the slide. All of the following buffers were prepared and applied as previously published.⁴⁶ Elution and staining procedures were repeated for each antibody until required IF plexity for the sample was reached. Image registration was performed using the Fiji ImageJ v1.52 descriptor-based registration plugin and Hoechst 33342 staining for registration. After registration, fluorescence intensities were manually adjusted for proper labeling of positive cells (excluding nonspecific background and autofluorescence signal) and QuPath image analysis software was used for cell segmentation and image analysis.⁴⁷ For 4i FFPE-tissue imaging, an automated microscope scanning stage and 20 \times objective was used for sample positioning and repetitive imaging.

In Situ Topological Adhesome Mapping

In situ topological adhesome mapping (ITAM) was utilized to describe the cell-type specific IAC composition in the human kidney. IAC specific antibodies were applied for IF analysis as described above. On the basis of IF signal levels, IAC components were classified as low or not expressed, expressed, or specifically enriched for each analyzed compartment. In addition, recently published murine podocyte RNA sequencing and glomerular proteome datasets were used for external validation of the podocyte ITAM dataset (MES, GEC, and podocyte proteome A, Hatje *et al.*; podocyte proteome-B, Schell *et al.*; podocyte proteome C, Rinschen *et al.*).^{14,48–50} IAC components were determined as "expressed" with a cutoff expression of >50 transcript per million on mRNA level or with a log₂ fold-change cell-type/other glomerular cells between -0.5 and 0.5 on a

proteome level. IAC components were determined as cell-type-specific enriched with a statistical significant \log_2 fold change cell-type/other glomerular cells >0.5 and >50 transcript per million on mRNA level, or a statistical significant \log_2 fold change podocyte/nonpodocyte >0.5 on proteome level. Proximity interactions of podocyte IAC components were recently published.⁹

Measurement of Urinary Albumin and Creatinine

Urinary albumin excretion was assessed as a direct indicator of glomerular barrier integrity. Albumin-creatinine ratios were quantified by measuring spot urine from WT and respective KO mice at defined time points. Albumin levels were determined by using a mouse specific albumin ELISA kit (ab108792, Abcam). Urinary creatinine measurements were performed by using an enzymatic creatinine kit (Creatinine PAP LT-SYS LT-CR 0106, Labor & Technik, Eberhard Lehmann, Germany). All assays were used according to manufacturer's instructions.

Analysis of Murine Blood Serum

Collected serum samples were stored at -80°C until use. For the measurement of creatinine and urea enzymatic kits were used, following the manufacturer's instructions (Creatinine PAP LT-SYS LT-CR 0106, Urea LT-UR 0010, Labor & Technik, Eberhard Lehmann, Germany).

IF Staining of Cultured Cells

For IF staining cells were cultured on collagen IV (Sigma-Aldrich, C5533) or (only if indicated) fibronectin (Corning, 354008) coated, eight-well chamber slides (Ibidi, 80827) or on circular RGD micropatterned slides (30 μm and 100 μm diameters) (Ibidi, 83851) at 37°C for 24 hours. Podocytes were washed in PBS with 1 mM CaCl_2^{2+} MgCl_2^{2+} , fixed in 4% PFA (Electron Microscopy Sciences, 15714-S) in PBS (Thermo Fisher Scientific, 10010023) for 20 minutes, washed three times in PBS, and permeabilized applying 0.1% Triton X-100 in PBS for 3 minutes. HIAR in pH 9 Tris-EDTA buffer at 90°C for 40 minutes was performed for some antibodies as indicated in Supplemental Table 1. Cells were washed in PBS and subsequently blocked in 5% BSA in PBS for 1 hour at room temperature. Primary antibodies were diluted in blocking buffer and incubated at 4°C overnight. Samples were washed three times in PBS and fluorophore-tagged secondary antibodies (Alexa Fluor Dyes, Thermo Fisher Scientific) were diluted in blocking buffer and incubated for 45–60 minutes at room temperature. Nuclei were stained using Hoechst 33342 (Thermo Fisher Scientific, H3570) and F-actin using fluorophore-labeled phalloidin (Alexa Fluor, Thermo Fisher Scientific). Cells were washed six times with PBS and imaged in PBS. The 4i staining of fixed cells was essentially performed as

described previously.⁴⁶ Images were acquired by manual positioning of podocytes using a $40\times$ objective.

Cell Spreading and Protrusion Formation Assay

Cell-spreading assays were performed as previously described.⁴⁸ Briefly, podocytes were detached by trypsinization, three times washed in culture medium, counted, diluted to required concentration, and preincubated in culture medium (floating) at 37°C in a cell culture incubator for 20 minutes. Subsequently, podocytes were spread on collagen IV coated eight-well polymer coverslips (80822, Ibidi) for 30 minutes at 37°C . Coverslips were preincubated in culture medium in parallel to the cells. Podocytes were carefully washed with PBS (1 mM CaCl_2^{2+} MgCl_2^{2+}), fixed in 4% PFA in PBS, permeabilized, and stained by fluorophore-labeled phalloidin (Alexa Fluor, Thermo Fisher Scientific). Fiji ImageJ v1.52 was used for analysis of cell morphology by cell segmentation *via* thresholding. At least 100 cells per condition and individual replicate were analyzed. The 3D protrusion formation of immortalized podocytes was performed as previously described.⁴⁸ In brief, WT or pooled dKO (dKO-1,-2, and -3) cells were seeded in Matrigel (Corning), and incubated in 0.2% FCS podocyte culture medium containing 10 μM Y27632 (Selleckchem) for 24 hours at 37°C . Maximum intensity projections of z-stack images were generated and the "main" (longest) protrusion length was measured using Fiji ImageJ v1.52.

Cell-adhesion Assay

Cell adhesion was performed on different extracellular matrix components as previously described.³⁸ Collagen IV (50 $\mu\text{g}/\text{ml}$, Sigma-Aldrich, C5533), collagen I (50 $\mu\text{g}/\text{ml}$, PureCol, Advanced BioMatrix, 5005), fibronectin (50 $\mu\text{g}/\text{ml}$, human fibronectin, Corning, 354008), basement membrane gel (50 $\mu\text{g}/\text{ml}$ Matrigel, Corning, 356231), and laminin 521 or laminin 111 (5 $\mu\text{g}/\text{ml}$, Biolaminin LN, BioLamina, LN111, LN521) were used as indicated. Briefly, 24-well cell-culture plates were coated according to the manufacturer's instructions, overnight at 4°C . Coated wells were washed in PBS and blocked with heat-denatured BSA (1% in PBS) for 1 hour, then washed again in PBS. Cells were trypsinized, counted, diluted in culture medium, and preincubated in a cell-culture incubator at 37°C for 20 minutes (floating). Equal amounts of cells were seeded for 15 minutes on the precoated 24-well cell-culture plates (tissue culture plastic control was uncoated and not blocked with heat-denatured BSA; BSA control was uncoated tissue culture plastic blocked with heat-denatured BSA). For comparison of different ECM components, dKO-1/-2/-3 clones were pooled before seeding. After carefully washing three times in PBS and fixation in 4% PFA, adherent cells were stained with 0.1% crystal violet in ddH_2O for 1 hour. The dye was solubilized in 0.5% Triton X-100 in PBS, and absorbance was measured at 570 nm using a microplate reader.

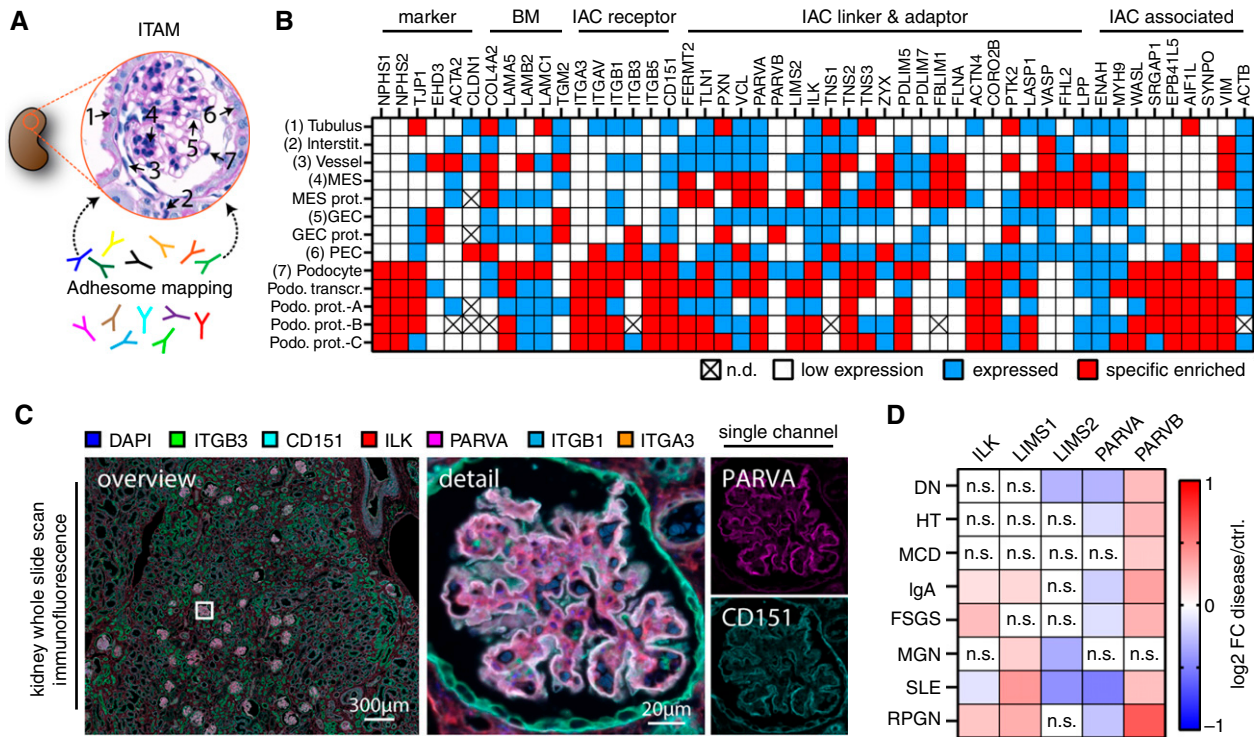


Figure 1. The IPP complex is a central constituent within the podocyte adhesome in situ. (A) and (B) Schematic depicting antibody-based *in situ* mapping of adhesome-related proteins within the human kidney (ITAM). On the basis of semiquantitative scoring, expression patterns were correlated to available cell-type-specific transcriptome and proteome data for podocytes (color code indicates semiquantitative scoring as low expressed, expressed, or specifically enriched; n.d., not detected; transcr., transcriptome; prot., proteome; podoc., podocyte; MES, mesangial cells; GEC, glomerular endothelial cells; PEC, parietal epithelial cells; see *Methods* for classification criteria). (C) Multiplex immunostaining for selected adhesome proteins on human kidney tissue validated compartment-enriched expression patterns for PARVA in the glomerulus. (D) mRNA profiles of IPP complex genes in various glomerular disease entities demonstrated almost uniform decreased levels of PARVA mRNA, whereas PARVB appeared with increased levels (n.s., nonsignificant; color-coded heatmap on the basis of log₂-fold changes between diseased tissue and healthy controls).

IAC Analysis

Quantification and analysis of IACs was performed as previously described.³⁸ Briefly, podocytes were seeded on 50 µg/ml collagen IV coated eight-well µ-slides (80827, Ibidi) and cultured for 24 hours at 37°C. Imaging and IF staining for the IAC components PXN, vinculin (VCL), PARVB, ILK, zyxin (ZYX), and F-actin (phalloidin) was performed as described above. PXN-ILK, VCL-PARVB, PXN-ZYX-phalloidin were costained on the basis of the host species of antibodies. For analysis of IACs, an image-processing macro for Fiji ImageJ v1.52 was used, as described before.²¹ In brief, individual IACs were segmented on the basis of PXN or VCL staining and analyzed for morphometric parameters and mean fluorescence intensities. In addition, the corresponding cell size was measured to calculate IAC density and the fraction of IAC covered basal surface area for individual podocytes. At least 30 cells per condition and independent experiment were analyzed. Data from PXN- and VCL-based segmentation were combined for analysis of morphometric IAC parameters.

IAC Mechano-linkage Assay

To assess the effect of extracellular mechanical preload, podocytes were cultured on collagen IV-coated PDMS substrates (CytoSoft, Advanced BioMatrix) with various rigidities (2 kPa, 16 kPa, and 64 kPa) and glass chamber slides (Ibidi). Previous work has shown that nocodazole stabilizes (force dependent) IAC maturation,^{51,52} whereas the ROCK inhibitor Y-27632 releases intracellular actomyosin tension on IACs.⁵³ Moreover, these mechanisms were demonstrated to control tension-dependent adhesion stability in an ILK-dependent manner.⁵⁴ Podocytes were precultured at 37°C for 24 hours on substrates with various rigidities, followed by addition of 20 µM nocodazole (S2775, Selleckchem), or 20 µM nocodazole and 10 µM Y-27632 (S1049, Selleckchem), or DMSO as a treatment control for 4 hours. Podocytes were stained by phalloidin and analyzed for cell morphology (cell collapse/rounding). At least 150 podocytes per condition, genotype, and replicate (total over 28,000 cells) were analyzed.

Analysis of Cell-derived Matrices

Synthesis and analysis of cell-derived matrices (CDMs) of podocytes were performed as essentially described before.³⁸ In brief, podocytes were seeded for 7 days on gelatin-coated coverslips. After decellularization, CDMs were fixed

in PFA and assayed by indirect IF staining for COL4A2 and FN1 as described above. Semiquantitative scoring of CDMs was performed on the basis of a five-tiered grading scheme, as previously described.³⁸ Microscopy z-stacks

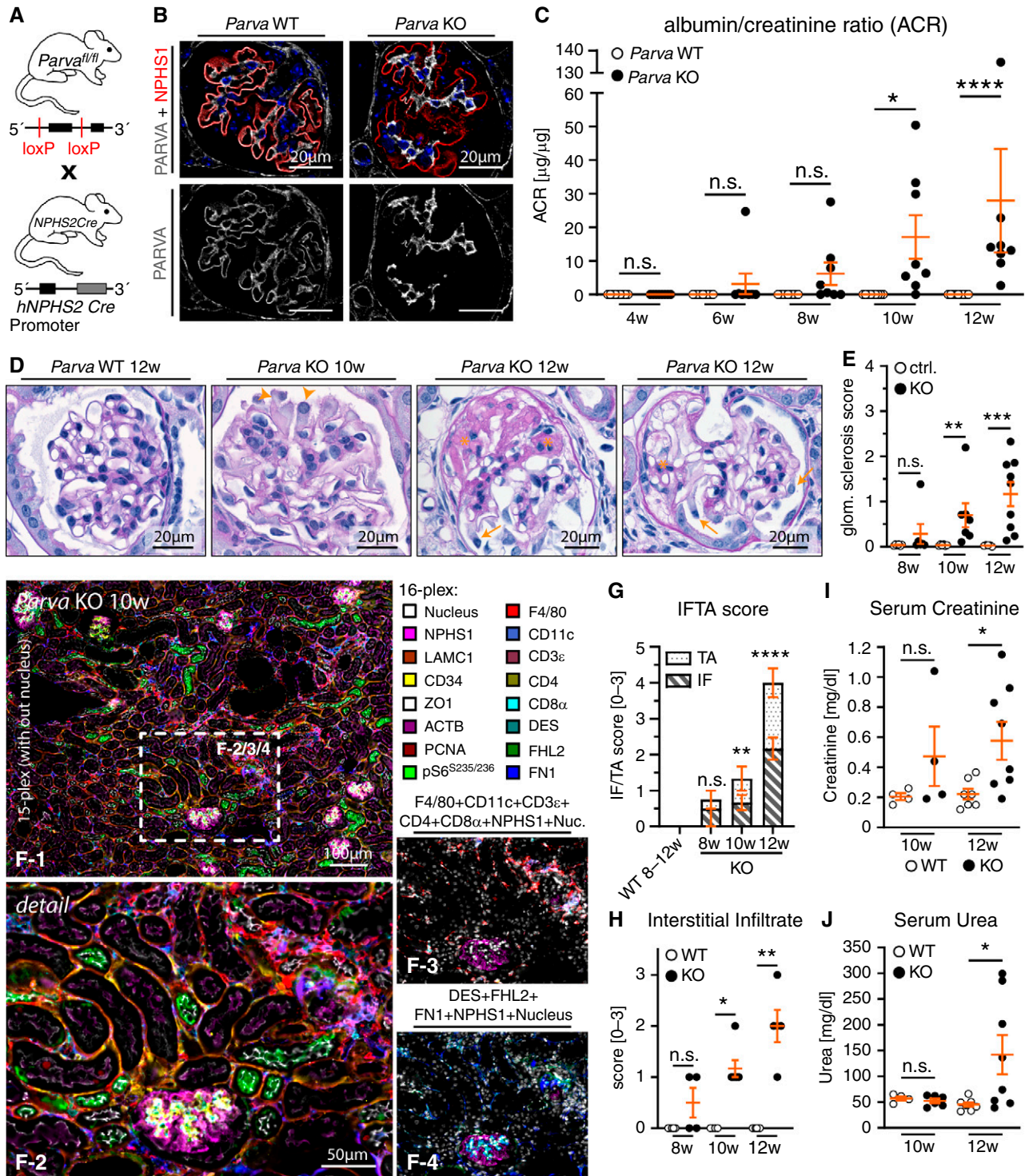


Figure 2.

Figure 2. Loss of *PARVA* results in FSGS-like glomerular disease with rapid progression to end-stage-kidney disease. (A) Schematic indicating the crossing strategy for the generation of podocyte-specific conditional KO for *Parva*. (B) IF staining for *PARVA* and the podocyte-specific marker *NPHS1* were used to validate efficient deletion of *PARVA*. Positive staining remained detectable within the mesangial and parietal cell compartment in respective KO animals. (C) Urinary albumin-creatinine ratio (ACR) measurements indicated significantly increased levels of proteinuria at the age of 10 weeks after birth (each individual dot represents one experimental animal; at least nine WT and eight KO animals were analyzed per time point). (D) and (E) Histologic evaluation of glomerular damage patterns employing Periodic acid–Schiff staining. At 10 weeks of age, only modest expansion of the mesangial compartment and incipient podocyte detachment was detectable (orange arrowheads indicate detaching podocytes). With persistent proteinuria, areas of FSGS were detectable (orange asterisks) at 12 weeks of age, accompanied by prominent podocyte swelling (orange arrows). Assessment of glomerulosclerosis confirmed progressive glomerular damage resembling FSGS-like conditions (each dot represents one individual experimental animal; at least five WT and six KO animals were analyzed per time point). (F) Employing multiplex IF imaging infiltration of individual immune cell populations was evaluated in *Parva* KO and WT mice at 10 weeks of age. Here a prominent infiltration of F4/80 positive macrophages in interstitial and periglomerular regions was detected. Insert f-3 selectively depicts immune cell infiltrates and insert f-4 mesenchymal structures/markers (see Supplemental Figure 4 for single channels and WT). Color coded index indicates individually assessed markers by multiplex imaging: *NPHS1*, podocytes; *LAMC1*, basement membranes; *CD34*, endothelial cells; *ZO1* (*TJP1*), epithelial cells; *ACTB*, cellular actin cytoskeleton; *PCNA*, proliferating cells; *pS6*^{S235/236}, mTOR pathway activation; *F4/80*, macrophages; *CD11c*, conventional dendritic cells; *CD3ε*, T lymphocytes; *CD4*, regulatory T lymphocytes, *CD8α*, cytotoxic T lymphocytes; *DES*, Desmin intermediate filament rich cells (e.g., mesangial cells and fibroblasts); *FHL2*, mesangial cells and fibroblasts; *FN1* (Fibronectin), extracellular matrix. (G) and (H) Semiquantitative assessment of structural damage in terms of tubular atrophy and interstitial fibrosis correlated to the progressive nature of glomerular disease (bar charts present mean values; at least four animals were analyzed per time point; dots present individual animals). (I) and (J) Analysis of serum creatinine and urea levels reflected the observed structural tissue damage in respective *Parva* KO animals (each individual dot represents one experimental animal; at least four animals were analyzed per time point). * $P < 0.05$, ** $P < 0.01$, *** $P < 0.001$ and **** $P < 0.0001$, n.s., nonsignificant.

were acquired using a 100× objective and processed to maximum intensity projections for image presentation.

RNA Sequencing

Isolation of glomeruli from 8- to 9-week-old male mice (with onset of proteinuria) was performed on the basis of perfusion with magnetic beads (Dynabeads), as previously described in detail.⁵⁵ RNA was isolated from whole glomeruli using the Qiagen RNeasy midi Kit (74104, Quiagen) according to the supplier's instructions. Poly(A) selection, library preparation, and Illumina NovaSeq 6000 2 × 150bp paired-end sequencing was performed by GENEWIZ Germany. The NEBNext Ultra II Directional RNA Library Prep Kit (New England Biolabs) was used. Demultiplexing and adapter trimming were performed with *bcl2fastq* v2.19. A total of 15–27 million reads per sample were sequenced. The Galaxy Europe platform was used for data analysis.⁵⁶ The build in *mus musculus* (mm10) genome and *Cutadapt* v1.16.5, *HISAT2* v2.1,⁵⁷ *featureCounts* v1.6.4,⁵⁸ and *DESeq2* v2.11.40.⁵⁹ tools were applied for read processing, mapping, and differentially expression analysis. Sequencing data have been deposited in NCBI Gene Expression Omnibus and are accessible via GEO series accession number GSE181690 (*adhesome* component analysis is enclosed in Supplemental Table 2 and differential expression analysis is enclosed in Supplemental Dataset 1).

Human Microarray Analysis

Human renal biopsy specimens were collected in an international multicenter study, the European Renal cDNA

Bank-Kröner-Fresenius biopsy bank (ERCB-KFB⁶⁰). Biopsies were obtained from patients after receiving informed consent, and with the approval of the local ethics committees. After renal biopsy, the tissue was transferred to an RNase inhibitor, and microdissected into glomeruli and tubulointerstitium. Total RNA was isolated from microdissected glomeruli, reverse transcribed, and linearly amplified according to a protocol previously reported.⁶¹ Published datasets of glomerular samples were analyzed for mRNA expression levels (GSE32591, GSE35489, GSE37463, GSE47185, GSE 99340). Analysis included gene expression profiles from patients with diabetic nephropathy (Glom: $n = 14$), hypertensive nephropathy (Glom: $n = 15$), minimal change disease (Glom: $n = 15$), IgA nephropathy (IgA; Glom: $n = 27$), FSGS (Glom: $n = 23$), membranous nephropathy (Glom: $n = 21$), lupus nephritis (SLE; Glom: $n = 32$), ANCA-associated glomerulonephritis (Glom: $n = 23$), and controls (living donors (Glom: $n = 41$)). CEL file normalization was performed with the Robust Multichip Average method using RMAExpress (Version 1.20) and the human Entrez-Gene custom CDF annotation from Brain Array version 25 (http://brainarray.mbni.med.umich.edu/Brainarray/Database/CustomCDF/CDF_download.asp). To identify differentially expressed genes, the significance analysis of microarrays method⁶² was applied using the correct function in Multiple Experiment Viewer (TiGR MeV, Version 4.9). A q -value < 5% was considered to be statistically significant. Correlation analyses (Supplemental Table 3) were performed using spearman correlations (SPSS 27.0, IBM Corp.). Bootstrapping was applied to obtain 1000

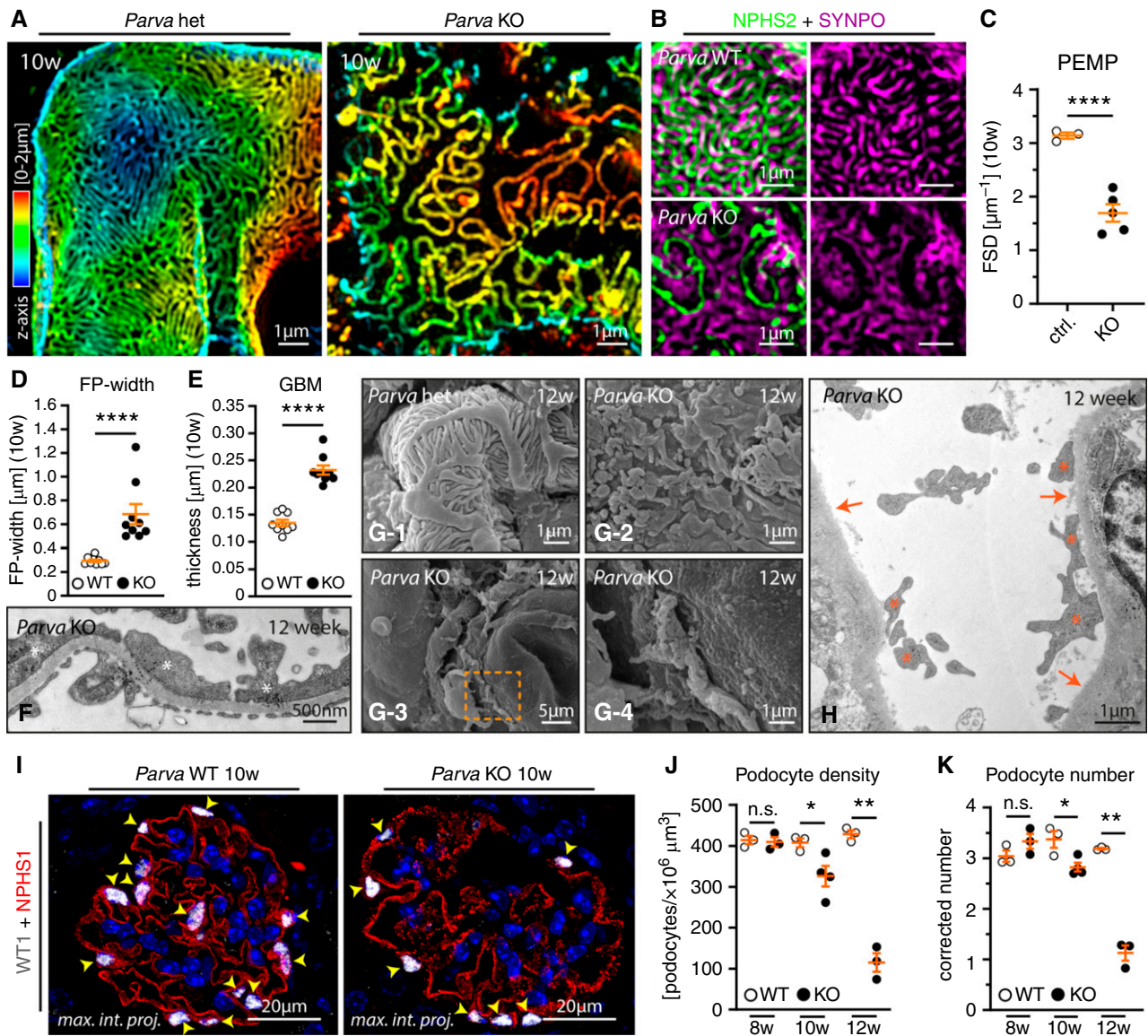


Figure 3. PARVA prevents podocyte detachment from the GBM. (A–C) 3D-SIM in respective KO animals identified a reduced filtration slit density (FSD) indicative for aberrant FP architecture (SIM data of 3 control: two WT, one heterozygous, and five KO animals were quantified by PEMP). Z-axis scales of 3D-SIM were color coded as indicated. (D–F) TEM of respective KO and WT animals demonstrated significant retraction and simplification of podocyte FPs in podocytes from KO mice (FP effacement, white asterisk). These changes were accompanied by rarefaction of slit diaphragm density (three animals per time point and genotype were analyzed for mean FP width and GBM thickness; dots indicate individual glomeruli; see Supplemental Figure 5 for additional images of WT and KO animals). (G) and (H) SEM and TEM studies at 12 weeks of age showed a pronounced denudation of the GBM due to ongoing podocyte detachment (orange dotted squared box indicates areas of zoom-in; orange asterisks highlight residual fragments of persistently linked podocyte FPs to the GBM; orange arrows indicate areas of completely denuded GBM). (I) IF microscopy employing NPHS1 to highlight the podocyte compartment, and WT1 as a specific nuclear marker for podocytes (yellow arrowheads mark individual podocyte nuclei in WT and respective KO animals). (J) and (K) Quantification of podocyte numbers at 8, 10, and 12 weeks after birth revealed a progressive decrease in parameters such as podocyte density (J) and corrected podocyte numbers (K) (each individual dot represents one experimental animal, at least three animals per time point and genotype were analyzed). * $P < 0.05$, ** $P < 0.01$ and **** $P < 0.0001$.

times resampling and derive the corresponding 95% confidence interval for the correlation coefficient. A P value < 0.05 was considered statistically significant. In addition,

the Nephroseq database (www.nephroseq.org) was used for analysis of ZYX, ACTN4, and TLN1 expression in human glomerular disease (“Ju CKD Glom” dataset).

Quantification and Statistical Analysis

If not stated otherwise, data are expressed as mean ± SEM. Scatter dots indicating individual data points were used for

statistical analysis. Statistical tests were used on the basis of data distribution and experimental design. Statistical tests and the unit of analysis used for each experiment are

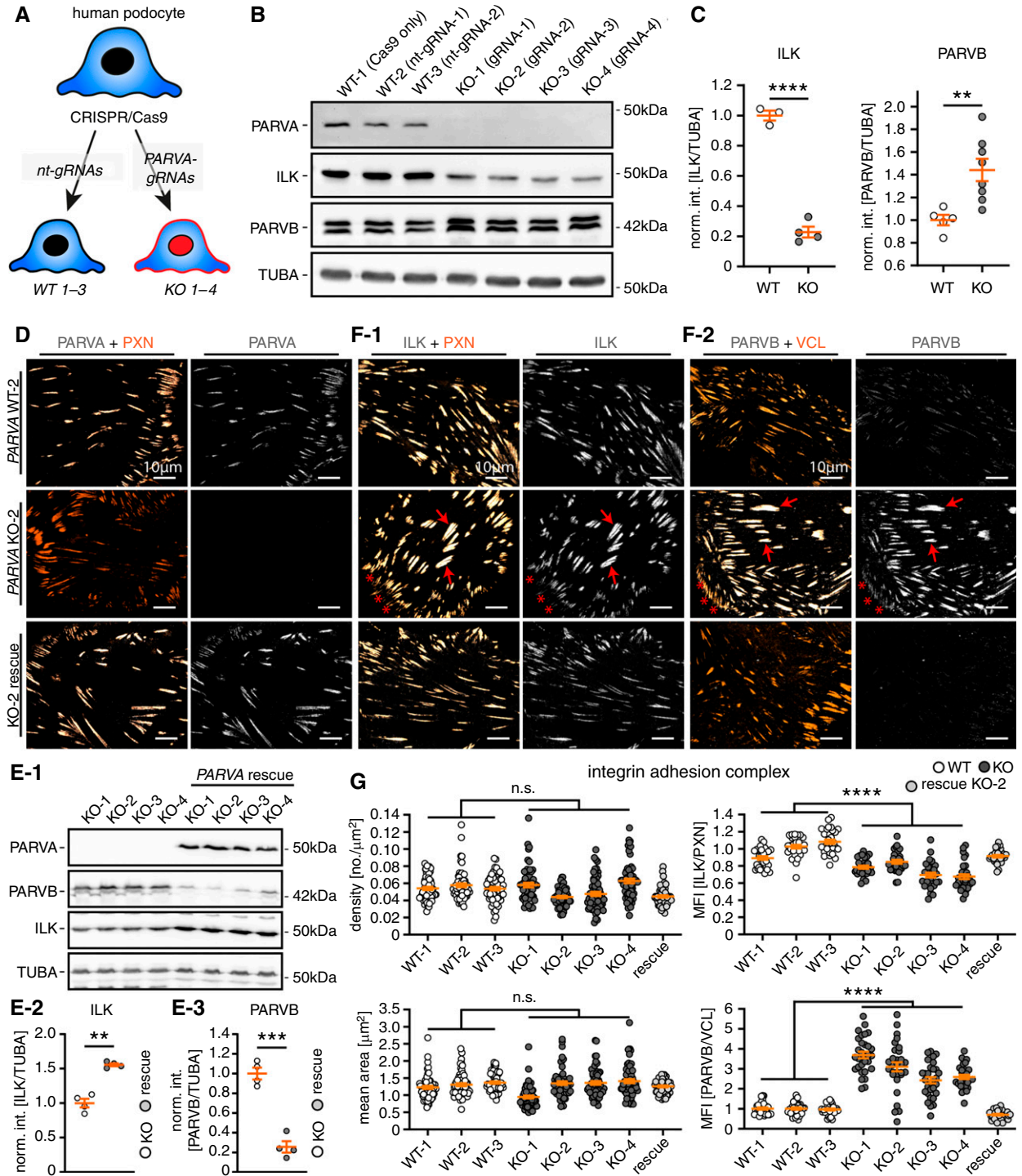


Figure 4.

Figure 4. Parvin proteins exhibit compensatory recruitment toward IAC. (A) Schematic describing the CRISPR/Cas9-based genome editing strategy to generate specific KOs for *PARVA* in immortalized human podocytes (nt-gRNA, nontargeting guide RNA; note, numbers 1–3 and 1–4 indicate respective clones for individual gRNAs). (B) and (C) Western blot analysis for *PARVA*, *ILK*, and *PARVB* confirmed complete abolishment of *PARVA* protein levels in respective individual KO clones from four independent gRNAs. In addition, *ILK* levels were significantly reduced whereas *PARVB* protein levels showed a compensatory increase in respective KO cells (dots represent individual cell lines; for *PARVB* two independent replicates for each cell line were combined for statistical analysis, int., intensity, norm., normalized to WT). (D) The specific localization of *PARVA* to the subcellular IAC compartment was demonstrated by costaining with *PXN* in either WT, *PARVA* deleted, or rescued KO cells (upper and lower panel, respectively). (E) Re-expression of a flag-tagged version of *PARVA* in *PARVA* KO 1–4 clones not only restored *PARVA* protein levels, but also reversed *ILK* decrease and *PARVB* compensatory responses (*TUBA*, tubulin alpha used as a loading control; dots represent individual cell lines; int., intensity; norm., normalized to KO). (F) IF imaging for *ILK* and *PARVB* localization patterns revealed only slightly decreased recruitment of *ILK* toward IACs accompanied by strongly increased recruitment of *PARVB* (red arrows indicated IACs with strong colocalization patterns for individual IAC proteins; *PXN* or *VCL* was used as IAC marker). (G) Morphometric analyses demonstrated that *PARVA* deficient cells do not exhibit significant alterations in numbers and mean size of IACs (individual dots represent 60 analyzed cells per clone; two independent experiments for morphometric measurements were conducted and 30 cells per clone and experiment were analyzed). Ratiometric imaging for *ILK* and *PARVB* mean fluorescence intensity (MFI) levels demonstrated significant differences in localization toward the IAC depending on *PARVA* (MFIs were normalized to the mean of WT clones; individual dots for *ILK* and *PARVA* MFI measurements represent 30 analyzed cells per clone of one representative experiment, respectively). Cells of WT and KO clones were pooled for statistical testing. ** $P < 0.01$, *** $P < 0.001$, and **** $P < 0.0001$.

collectively shown in Supplemental Table 4. The GraphPad Prism 8 software was used for statistical analysis. Statistical significance was defined as * $P < 0.05$, ** $P < 0.01$, *** $P < 0.001$, and **** $P < 0.0001$, or non-significant (ns). The number of independent experiments and total amount of analyzed cells, mice, or samples are stated in the figures and/or figure legends.

RESULTS

The IPP Complex Is a Central Constituent within the Podocyte Adhesome In Situ

We combined large-scale antibody-based staining approaches with available transcriptomic and proteomic datasets to generate an *in situ* topological adhesome mapping (ITAM) of the human kidney with a focus on the glomerular compartment (Figure 1, A and B and Supplemental Figure 1). Localization patterns for the majority of selected epitopes correlated with cell-type specific transcriptome and proteome profiles (Figure 1B). These data highlighted a subset of proteins within glomerular podocytes, where the IPP complex appeared as a central motif interconnected with a multitude of other adhesome-related proteins (Supplemental Figure 2). Using multiplex imaging techniques, we validated ITAM profiles by showing a pronounced expression pattern of the IPP component *PARVA* in human glomeruli (Figure 1C and Supplemental Figure 2). Given the importance of podocyte adhesion, we analyzed the expression of IPP complex genes in a variety of glomerular disease entities. We observed a uniform reduction in *PARVA* mRNA levels, whereas *PARVB* appeared with increased abundance (Figure 1D). Decrease of *PARVA* and increase of *PARVB* mRNA levels significantly correlated with podocyte damage (as assessed by decrease of podocyte-specific marker genes, Supplemental Table 3).

Loss of *PARVA* Results in a FSGS-like Glomerular Disease with Rapid Progression to ESKD

To test the relevance of *PARVA* in podocytes, we used a recently established conditional allele for *Parva*.^{32,63} We crossed the podocyte-specific *hNPHS2-Cre* line with a floxed allele for *Parva* and validated KO efficiency *in situ* (Figure 2, A and B). Interestingly, podocyte-specific KO did not affect glomerular morphogenesis, reflected by normal glomerular filtration barrier function until the age of 8–10 weeks. Evaluation of albumin-creatinine ratios demonstrated a sudden and fast progressive phenotype later in life, as increasing levels of proteinuria were detected until 12 weeks after birth (Figure 2C). Moreover, KO mice showed mesangial hypercellularity and extracellular matrix deposition with the onset of albuminuria. Within only 4 weeks, these histologic lesions progressed to a stage of either global or segmental sclerosis (Figure 2, D and E and Supplemental Figure 3). This severe glomerular damage also affected tubular and interstitial renal parenchyma. Employing multiplex IF imaging demonstrated a predominant presence of interstitial and periglomerular F4/80 positive macrophage populations (Figure 2, F–H and Supplemental Figure 4), whereas increased interstitial fibrosis and tubular atrophy were observed in KO animals (Figure 2, G and H). Podocyte-specific loss of *Parva* translated into an abrupt onset of FSGS-like glomerular disease and an accelerated progression to ESKD (Figure 2, I and J).

PARVA Prevents Podocyte Detachment from the GBM

The association of *PARVA* with IACs implies that podocytes might detach from the GBM translating into the observed phenotype. We used super-resolution microscopy and established ultrastructural analysis *via* electron microscopy to characterize the effect of *PARVA* on podocyte morphology. Here, we observed that with the onset of

proteinuria, respective KO animals presented a more simplified podocyte morphology, including significant retraction of podocyte FPs (Figure 3, A–F and Supplemental

Figure 5). Detachment of podocytes from the GBM became increasingly apparent with ongoing disease progression, as demonstrated by SEM and TEM (Figure 3, D–H). At the

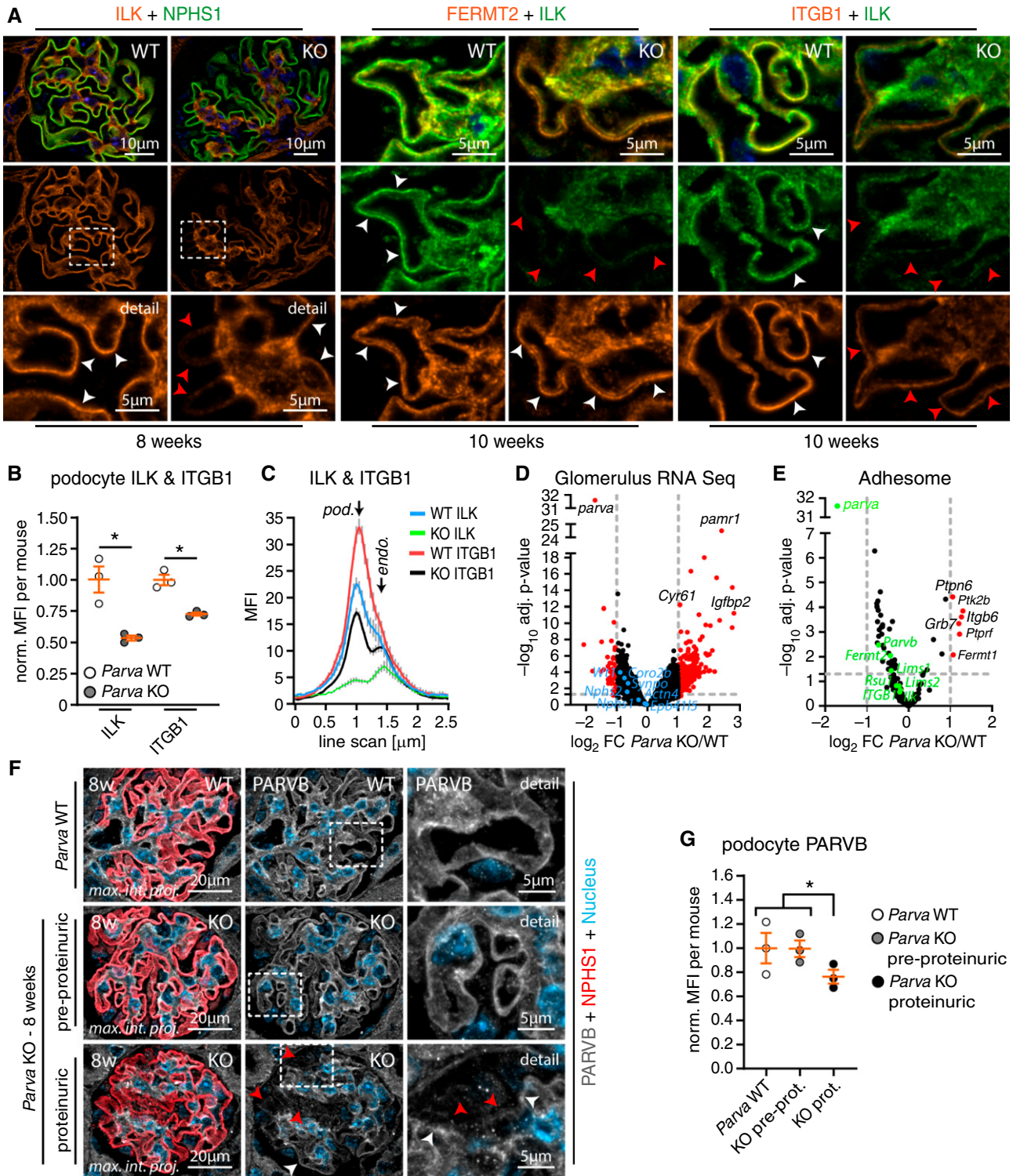


Figure 5.

Figure 5. Loss of PARVA induces degradation of the IPP complex *in vivo*. (A) IF imaging for ILK, FERMT2, and ITGB1 in WT and *Parva* KO mice after onset of proteinuria (8 weeks and 10 weeks, respectively). FERMT2 showed preserved signal and localization patterns, whereas ITGB1 and more pronounced ILK were reduced in the podocyte compartment (white dashed boxes indicate zoomed-in areas in the lower panel, white arrowheads indicate preserved signal intensities, red arrowheads mark decreased signals). (B) Quantification of MFIs in the podocyte compartment showed a significant reduction in signal intensities of ITGB1 and ILK (NPHS1 staining was used to segment for the podocyte compartment; dots indicate mean values of individual animals; three WT and three KO animals and ≥ 20 glomeruli per animal were analyzed; see Supplemental Figure 13 for analysis of ILK, ITGB1, and NPHS1 per glomerulus; norm., normalized to WT). (C) Representative line scans demonstrated reduced signal intensities for ITGB1 and ILK in the podocyte compartment (MFIs of representative line scans of respectively 10 glomeruli from one WT and one KO animal are shown). (D) and (E) Volcano plots of bulk glomerular RNA-sequencing experiments in 8–9-week-old animals (with onset of proteinuria) confirmed the efficient deletion of *Parva*. Further subfiltering for podocyte *adhesome* genes did not detect significant downregulations of respective genes at this age (pooled analysis from three WT and three *Parva* KO animals; blue dots indicate podocyte-specific marker genes, green dots indicate IPP complex proteins and associated IAC components). (F) and (G) IF analysis of PARVB signal intensities in the podocyte compartment of respective 8-week-old *Parva* KO animals detected decreased PARVB levels in animals at the onset of proteinuria, but not in pre-proteinuric KO animals (dashed boxes highlight areas of zoom-in; red arrowheads indicate glomerular podocytes with reduced signals; white arrowheads highlight podocyte compartments with preserved signal level intensities; NPHS1 staining was used to segment for the podocyte compartment; dots indicate mean values of individual animals; three WT, three preproteinuric, and three proteinuric KO animals and ≥ 20 glomeruli per animal were analyzed; norm, normalized MFI to WT; nonproteinuric (WT and preproteinuric KO animals were pooled for statistical analysis). * $P < 0.05$.

age of 10–12 weeks, loss of PARVA was characterized by a denudation (Figure 3, G and H and Supplemental Figure 5) and thickening of the GBM (Figure 3E and Supplemental Figure 5). We quantitatively evaluated the glomerular numbers and density of podocytes using IF microscopy. Quantitative analysis showed podocyte numbers decreased at 10 weeks after birth. This trend progressed even further with increasing age (Figure 3, I–K and Supplemental Figure 5). Interestingly, the decrease of podocytes per glomerulus was accompanied by a slight increase in glomerular volume, implying that podocytes exert buttress forces on the underlying glomerular capillary convolute (as also recently described³⁶). Altogether, these data demonstrate that a specific loss of PARVA in glomerular podocytes results in an accelerated loss of podocytes with overt denudation of the GBM.

Parvin Proteins Exhibit Compensatory Recruitment toward IACs

To further characterize the mechanistic effect of PARVA on podocytes, we used CRISPR/Cas9 genome engineered podocytes (including nontargeting guide controls, and four individual *PARVA* gRNAs and KO clones). Initial validation of these cell clones demonstrated the complete loss of PARVA and indicated degradation of ILK protein levels in respective KO clones (Figure 4, A–C). More interestingly, this reduction of ILK protein abundance was accompanied by increased levels of PARVB, indicative of an inherent compensatory mechanism within the IPP complex (Figure 4, B and C). Reintroduction and rescue of PARVA protein reversed this compensatory phenotype for degradation of ILK and upregulation of PARVB (Figure 4, D and E and Supplemental Figure 6). These observations indicated a potential effect on *adhesome* composition corresponding to

respective PARVA protein levels. Therefore, we used a recently established multiplex IF imaging approach to evaluate the *in situ* distribution and localization patterns of selected IAC components.⁴⁶ We observed a pronounced signal decrease for ILK at individual IAC sites, other core *adhesome* components such as ZYX, ACTN4, or paxillin (PXN) appeared unaffected (Supplemental Figure 6).

Further evaluation of WT, *PARVA* KO, and respective rescue clones demonstrated a preferential redistribution of ILK toward centrally localized IACs. In contrast, IACs that are more peripheral showed reduced levels of ILK. More interestingly, the altered subcellular localization of ILK was characterized by a pronounced increase in PARVB signals at internally localized IAC sites (Figure 4F). Ratio- and morphometric imaging studies furthermore demonstrated the sole loss of *PARVA* had no significant effect on structural parameters of IACs (Figure 4G and Supplemental Figure 7), but instructed the recruitment of IPP complex components such as PARVB, thereby sustaining recruitment of ILK to podocyte IACs (Figure 4G and Supplemental Figure 6).

Loss of PARVA Induces Degradation of the IPP Complex *In Vivo*

The detailed analysis of our *in vivo* model revealed a sudden disease onset and rapid progression to FSGS due to the pronounced detachment of podocytes (Figures 2 and 3). However, further *in vitro* modeling highlighted compositional changes at individual IACs (Figure 4). Therefore, we aimed to translate these observations toward the more complex situation *in vivo*. Employing IF microscopy at different disease time points revealed that decreased signal intensities for ILK only became evident with disease onset, and even preceded changes for NPHS1 (as a highly sensitive marker for podocyte damage, Figure 5A). The

heterogeneous pattern of ILK decrease within the capillary convolute might reflect the compensational nature of ongoing IPP dissolution under *in vivo* conditions. Interestingly, other core *adhesome* proteins such as FERMT2 were

unaffected, overall supporting the specificity of this observed shift in *adhesome* composition *in vivo* (Figure 5, A–C and Supplemental Figure 8). To elucidate whether these early effects depend on transcriptional alterations or

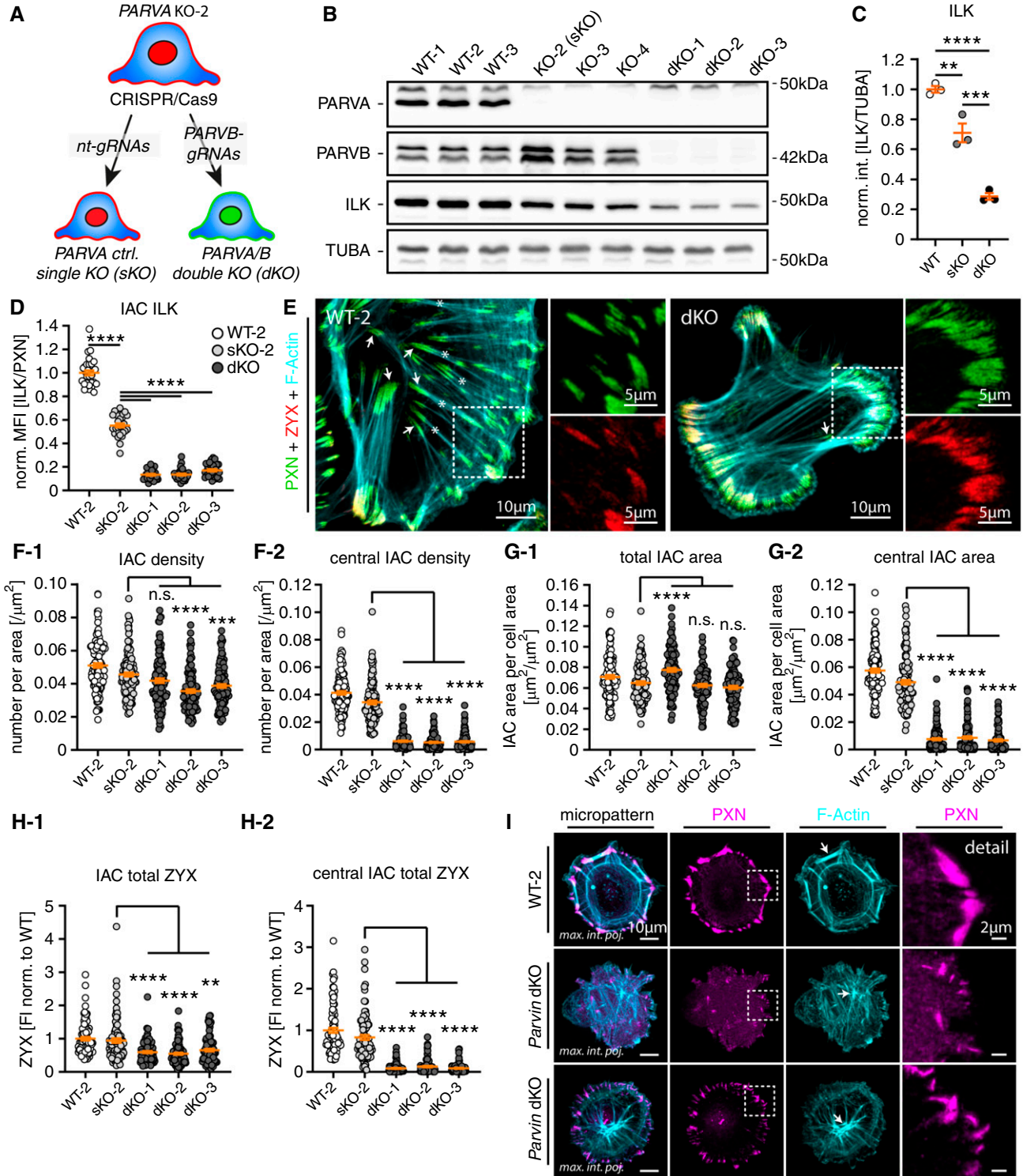


Figure 6.

Figure 6. Dissolution of the podocyte IPP complex translates into the IAC class switch. (A) Schematic describing genome engineering to generate control *PARVA* sKO-2 and dKO podocyte clones for *PARVA* and *PARVB*. (B) and (C) Western blot experiments confirmed the efficient deletion for *PARVA* and *PARVB* accompanied by progressive decrease in ILK protein abundance (individual dots indicate independent monoclonal clones). (D) Ratiometric analysis for ILK signal levels at individual IACs demonstrated progressive signal reduction, depending on *PARVA* and *PARVB* presence (dots represent individual cells; 30 cells per clone of one representative experiment were analyzed; MFIs were normalized to WT-2). (E) IF microscopy for the IAC marker PXN and Zyxin (ZYX) showed a pronounced shift in IAC classes. Control cells exhibited centrally localized IACs coupled to ventral F-actin stress fibers (white asterisks and arrows respectively; F-actin was stained by phalloidin). Respective dKO cells showed only feathered, peripherally localized IACs connected with thin actin fibers (white dashed boxes indicate zoomed-in areas). (F) and (G) Morphometric analysis and clustering of IAC size and distribution demonstrated a nearly complete loss of internal IACs in dKO cells (dots present individual cells derived from four independent experiments; 30 cells per experiment and clone, total of 120 cells per clone, were analyzed; sKO-2 cells were compared with individual dKO clones for statistical testing). (H) Ratiometric imaging indicated overall decreased levels of IAC bound ZYX related to nearly absent binding to central IACs in respective dKO cells (total IAC ZYX FI per cell was analyzed; dots represent individual cells derived from three independent experiments; 30 cells per experiment and clone (total of 90 cells per clone) were analyzed; sKO-2 cells were compared with individual dKO clones for statistical testing). (I) IF microscopy on space restricted micropatterned surfaces revealed diminished IAC formation in dKO cells accompanied by a diffuse and loosely interweaved actin network (white arrows indicate F-actin fibers; white dashed boxes indicate zoomed-in areas). ** $P < 0.01$, *** $P < 0.001$, and **** $P < 0.0001$.

post-translational events, we isolated glomeruli from WT and *Parva* KO animals and performed RNA sequencing (Figure 5, D and E, Supplemental Table 2, and Supplemental Dataset 1). These analyses confirmed the very efficient deletion of *Parva* in respective KO animals (Figure 5D). Interestingly, a subanalysis of *adhesome*-related genes did not demonstrate pronounced alterations, further indicating that observed changes in ILK, ITGB1, and *PARVB* are related to post-transcriptional alterations (Figure 5E). This was furthermore supported by PLA showing decreased levels of ITGB1-ILK complexes at IACs within the podocyte compartment *in situ* (Supplemental Figure 8). Our previous *in-vitro* modeling approaches implied that *PARVB* partially compensates for the genetic deletion of *PARVA* (see Figure 4). Interestingly, *PARVB* signal levels within the podocyte compartment concomitantly decreased with the onset of albuminuria in respective KO animals, indicating that an intact IPP complex including *PARVA*/*PARVB* is required to maintain podocyte function (Figure 5, F and G).

Dissolution of the Podocyte IPP Complex Translates into IAC Class Switch

The complementary analysis of *in vitro* and *in vivo* models for genetic deletion of *PARVA* implied compensational responses at the podocyte IAC. To dissect underlying mechanisms and functional consequences, we further modified our *in vitro* models by sequential deletion of *PARVB* in *PARVA* single KO (sKO) podocytes (Figure 6A and Supplemental Figure 9). We selected three double KO (dKO) clones, which demonstrated a further decrease in ILK protein levels when compared with sKO clones for *PARVA* or WT cells (Figure 6, B and C). These observations were validated by rescue cell lines for either *PARVA* or *PARVB*, and by analysis on the individual IAC ILK levels using IF microscopy, demonstrating

an almost complete loss of ILK from IAC sites in dKO cells (Figure 6D and Supplemental Figure 9). Morphometric analysis revealed the overall density and area of IACs not to be consistently altered in all clones on combined deletion of *PARVA* and *PARVB* (Figure 6, E–G). However, dKO clones showed a pronounced change of IAC distribution patterns, where central IACs were almost completely absent (Figure 6, E–G and Supplemental Figure 9). These centrally localized IACs are commonly linked to ventral actin cytoskeleton stress fibers (VSFs) and are involved in cellular processes, such as mechano-transduction and force transmission.^{64,65} To better characterize mechano-linkage in dKO cells, we used ratiometric imaging using IF microscopy for F-actin, ZYX, and PXN. These experiments demonstrated that peripheral IACs in dKO cells have a more confluent morphology accompanied by dysbalanced recruitment of mechano-transductive *adhesome* components, such as ZYX and F-actin (Figure 6H and Supplemental Figure 9). As the development of VSFs is highly dependent on cellular morphology, we made use of micropatterned surfaces to synchronize cells. Under these harmonized conditions, respective dKO cells formed only punctuate and misaligned IACs at the cellular periphery, accompanied by a weakly interconnected and disordered actin cytoskeleton (Figure 6I and Supplemental Figure 10). Together, these observations demonstrate that *PARVA*/*PARVB* critically determine the assembly of IAC subclasses (peripheral versus central) and structure of the related actin cytoskeleton.

PARVA/B are Critically Required for Establishing Efficient Mechano-linkage

Integrin receptor engagement is one main axis in establishing efficient cell-matrix interactions involving outside-in and inside-out signaling. Evaluating cellular adhesion, dKO cells showed drastically reduced adhesion capabilities when compared with *PARVA* sKO cells and WT control cells

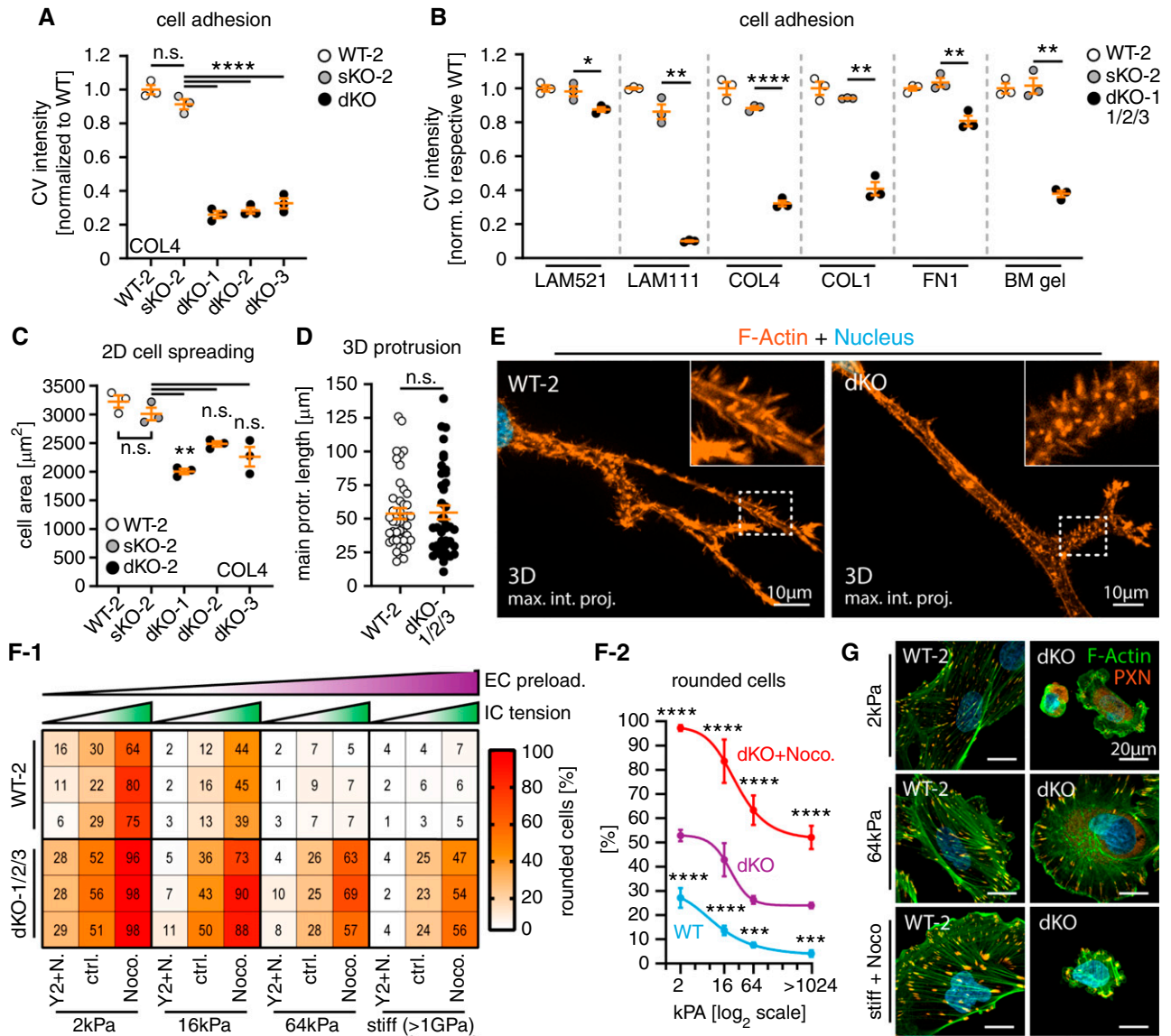


Figure 7. PARVA/B are critically required for establishing efficient mechano-linkage. (A) and (B) PARVA/B dKO podocytes showed drastically reduced cell adhesion on specific ECM ligands (each dot presents one individual replicate per genotype, relative numbers of adherent cells were determined by crystal violet [CV] staining). (C) Cell spreading assays demonstrated only slightly impaired dynamic spreading capacity of dKO cells on collagen IV (COL4), whereas sKO-2 showed only mild differences to respective WT-2 controls (each dot presents mean size of one individual replicate and experiment per genotype; ≥ 100 cells per clone and experiment were analyzed). (D) and (E) Analysis of 3D protrusion generation in basement membrane gels (matrigel) showed no obvious alterations of protrusion formation of dKO podocytes (each dot presents one cell per genotype; dKO-1/2/3 clones were pooled for analysis; ≥ 40 cells per genotype were analyzed; white dashed boxes zoomed-in areas; cells were stained for F-actin by phalloidin). (F) and (G) Podocyte morphology depending on sufficient mechano-linkage by IACs integrating extracellular (substrate) mechanical preload and intracellular cytoskeleton tension. Disruption of the IPP complex in dKO cells caused impaired adaptation to low substrate preload and high cytoskeleton tension reflected by morphologic collapse (rounding) and detachment of podocytes (values indicate percentage of rounded cells per individual replicate; three independent experimental replicates and ≥ 205 cells per condition and replicate were analyzed; EC, extracellular; IC, intracellular; Noco. or N., Nocodazole; Y2, Y-27632). Shown statistical significances (F-2) refer to comparison of WT-2 to dKO and dKO-nocodazole to dKO cells for indicated experimental conditions (three independent replicates per experimental condition). Images show representative experimental conditions and cells with collapsed (rounded) or spread morphology stained for F-actin and PXN (see Supplemental Figure 12 for overview images). Error bars indicate SEM (A)–(D) or SD for graph (G); * $P < 0.05$, ** $P < 0.01$, *** $P < 0.001$, and **** $P < 0.0001$.

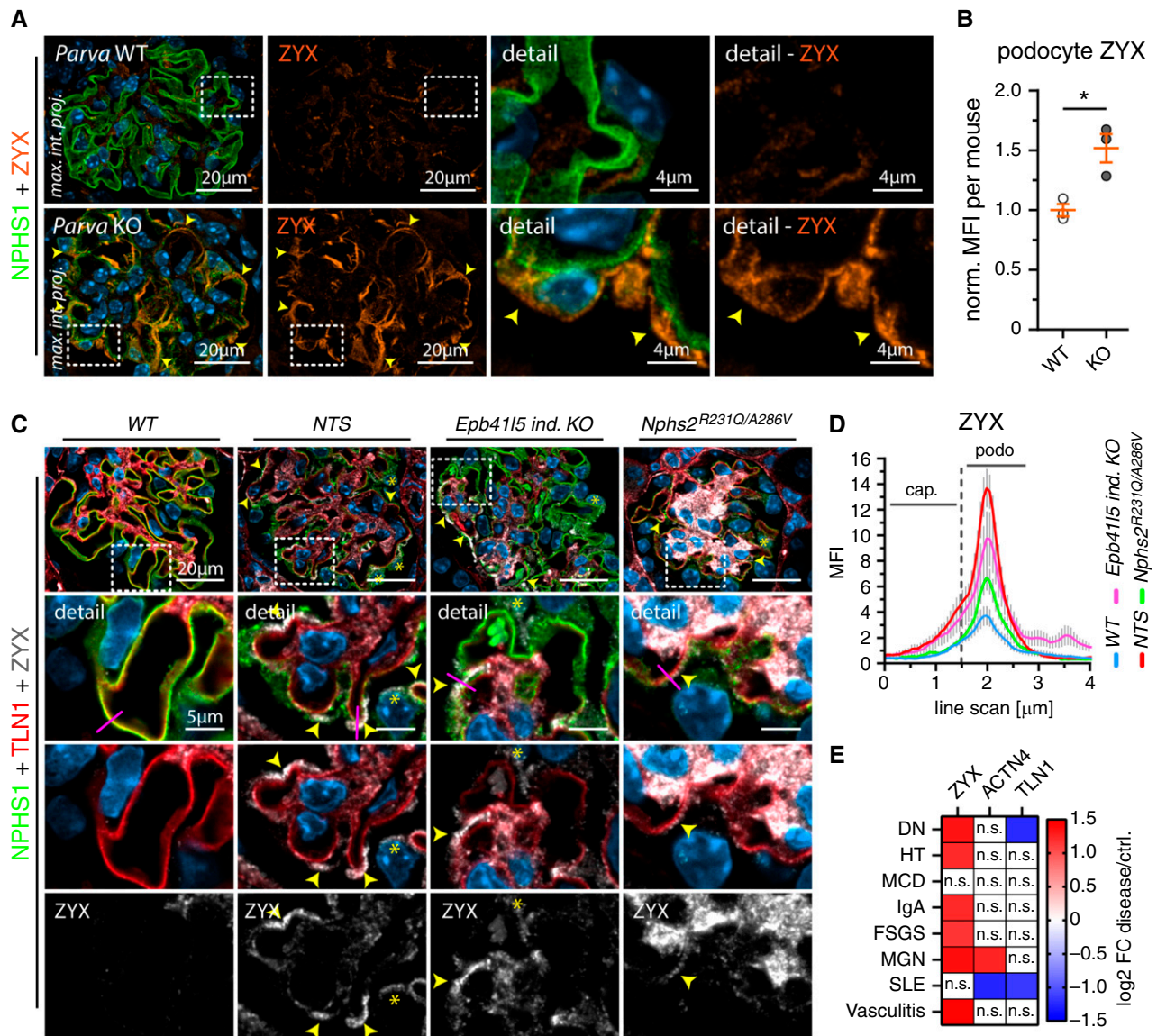


Figure 8. PARVA controls adhesome composition and mechano-adaptive ZYX expression *in vivo*. (A) and (B) IF analysis revealed altered patterns (yellow arrowheads) and increased intensity levels for ZYX in *Parva* deficient podocytes (10 weeks of age). Quantitative assessment of MFI in the podocyte compartment confirmed significant increase of ZYX levels (NPHS1 staining was used to segment for the podocyte compartment; dots indicate mean values of individual animals; three WT and three KO animals and ≥ 20 glomeruli per animal were analyzed; norm., normalized to WT; see Supplemental Figure 13 for analysis of ZYX per glomerulus). (C) and (D) Analysis of ZYX expression in murine disease models indicates upregulation of ZYX as a common pattern in podocyte disease. ZYX accumulation (yellow arrowheads) was detected slightly proximal of the SD and IAC layer as indicated by costaining of NPHS1 and TLN1, respectively (yellow asterisks indicate ZYX expression in the cytoplasm of podocytes; representative line scan analysis [purple lines] of 10 glomeruli per genotype was performed; error bars indicate SEM; NTS, nephrotoxic serum; cap., capillary; podo., podocyte). (E) Analysis of human glomerular disease (Nephroseq database) further substantiated increased expression on mRNA levels of ZYX in varying glomerular disease entities. * $P < 0.05$.

(Figure 7A). Furthermore, we tested different ECM ligands and observed that adhesion defects were influenced in a ligand-dependent manner (Figure 7B and Supplemental Figure 10). However, overall expression levels of integrin receptors and adaptors appeared unaltered in dKO cells, whereas IAC patterns were disrupted for all tested integrin

receptors (Supplemental Figures 10 and 11). Therefore, observed adhesion defects might be caused by reduced integrin receptor activation due to IPP complex disruption, than by modulation of specific integrin receptors.⁶⁶ Next, we used cell-spreading assays to test if impaired adhesion in sKO and dKO podocytes translates into defective

protrusion generation. However, loss of only *PARVA* or *PARVA* and *PARVB* exerted mild to moderate effects on cell spreading, most likely explained by delayed adhesion (Figure 7C and Supplemental Figure 12). In line with these observations, no obvious alterations in protrusion generation were detectable in dKO cells under 3D cell culture conditions (Figure 7, D and E). To finally test whether disruption of the IPP complex translates into impaired mechano-linkage in podocytes, we set up a complementary assay evaluating external matrix rigidity levels (external IAC preload) and internal cytoskeletal tension (internal IAC/cytoskeleton tension, Figure 7, F and G and Supplemental Figure 12). Integrative analysis of these two essential parameters allowed to deduce that mechano-adaptive capacities are significantly impaired on deletion of *PARVA/B*, further supporting the notion that the IPP complex is centrally involved in IAC-cytoskeleton coupling in podocytes (Figure 8, C-D). This model is furthermore substantiated by drastically impaired matrix assembly function in dKO cells (Supplemental Figure 12, a phenotype directly related to IAC-mechano-linkage³⁸).

PARVA Controls Adhesome Composition and Mechano-adaptive ZYX Expression *In Vivo*

Given the rapid detachment phenotype in our mouse model, we wondered whether an IPP dependent IAC composition switch is also responsible for this significant loss of podocytes *in vivo* (Figure 3). Notably, we observed increased signal intensities for mechano-transductive IAC components such as ZYX in respective KO animals, whereas other *adhesome* components were either unaffected or exhibited reduced signal levels, such as integrin receptors (Figure 8, A and B, Figure 5, and Supplemental Figure 13). Moreover, analysis of murine models of glomerular disease and human disease datasets indicated ZYX expression as a common mechano-adaptive response in podocyte disease entities (Figure 8, C - E). Interestingly, ZYX expression was increased in IAC-triggered podocyte disease (*Parva* KO animals), but only modestly affected in (primarily not detaching) disease entities caused by slit diaphragm dysfunction (*Nphs2*^{R231Q/A286V}).³⁶ These findings suggest specific alterations of the podocyte IAC composition *in vitro* and *in vivo* caused on impaired IPP complex function.

DISCUSSION

Podocyte detachment is a unifying theme in a variety of glomerular diseases, ranging from genetic to acquired pathologies.⁶⁷⁻⁶⁹ However, it is still not clear whether dynamic compensation occurs at podocyte IACs, or how such modulations might affect efficient mechano-linkage to the GBM and influence the integrity of the glomerular filtration barrier.

In this study, a comprehensive topological *in situ* staining approach highlighted the central role and enrichment of the IPP complex within the podocyte compartment (Figure 1). Moreover, decreased mRNA levels of *PARVA* were observed in a variety of glomerular disease entities (Figure 1). Previous work already focused on the role of ILK in podocytes demonstrating that loss of ILK results in podocytopathy and proteinuria starting 2–3 weeks after birth.^{24,25} Of note, detailed analysis of our conditional KO model for *Parva* showed a relatively late onset of podocyte disease with albuminuria occurring not before 8–10 weeks of age (Figure 2). The phenotype in *Parva*-deficient animals rapidly progressed and exhibited classic histologic features resembling human FSGS (Figure 2). This difference in disease onset and progression between *Parva*- and *Ilk*-deficient animal models might be attributable to differing molecular function of *PARVA* in the IPP complex, involved in actin cytoskeleton linkage and IPP complex stabilization. However, also varying genetic backgrounds and/or differential compensation (*e.g.*, *via PARVB*) at the podocyte IAC site might also influence these phenotypic differences.

One main finding of our attempts to model sequential disruption of the IPP complex is the observation that deletion of *PARVA/PARVB* resulted in a complete IAC class switch (Figures 4 and 6). Respective dKO cells only assembled peripheral adhesion sites, whereas central IACs linked to the ventral actin cytoskeleton were vastly reduced, compared with single KO cells for *PARVA*. This switch of IAC classes functionally translated into impaired cellular adhesion, indicating a defect in efficient mechanical linkage between IACs and the cytoskeleton (Figure 7). Although prior studies have observed that the sole deletion of *PARVA* already resulted in impaired cellular adhesion, altered cytoskeletal architecture, and adhesion site formation,^{32,63} compensatory upregulation of *PARVB* in podocytes largely prevented any overt cellular dysfunction. In fact, a counterbalancing regulation of *Parvin* proteins has been previously demonstrated.⁷⁰

Integrating the observations from our *in vitro* studies raises the question of whether this podocyte loss is really caused by dissolution of receptor complexes or, rather, IAC functionality. Conventional ultrastructural studies and very recent super-resolution microscopy approaches described the formation of sarcomeric actin networks in conditions of podocyte foot process effacement.^{71,72} This adaptive cytoskeletal rearrangement is considered as a proxy for the formation of ventral actin cytoskeleton fibers (VSFs).⁶⁴ The drastic reduction of VSFs in dKO podocytes due to an IAC class switch might therefore imply insufficient IAC-cytoskeleton coupling as the underlying mechanism for podocyte detachment observed *in vivo* (Figures 3, 6, and 7). The IAC components ZYX and α -actinin (*e.g.*, ACTN4) have been shown to stabilize actin stress-fiber integrity, and thereby force transmission.^{73,74} Interestingly, recruitment of α -actinin to VSF occurred in a ZYX-dependent manner

and previous studies in human and murine glomerular disease also documented increasing levels of ACTN4,^{75,76} which potentially reflect increased integrin cytoskeleton coupling to overcome impaired podocyte adhesion.⁷⁷ In line with that, we discovered similar adaptive responses in IAC components (e.g., ZYX) in our *in vitro* and *in vivo* models, further supporting the concept of adaptive VSF and IAC remodeling in podocyte disease (Figures 7 and 8 and Supplemental Figure 13). Despite this significant adaptive response, loss of PARVA led to exaggerated podocyte detachment. These observations indicate insufficient linkage of reinforced tensile VSFs to IACs as a causative mechanism for podocyte detachment in glomerular disease (see also schematic Supplemental Figure 14).

In conclusion, in this investigation we provide combined *in vitro* and *in vivo* evidence for balanced compensatory events at podocyte IACs, ensuring the integrity of the glomerular filtration barrier. Future studies on specific compositional signatures in IACs might provide a conceptual framework for subclassification or substratification of glomerular pathologies and lead to the identification of potential therapeutic strategies to prevent podocyte detachment.

DISCLOSURES

E. Montanez reports being supported by the Spanish Ministry of Science, Innovation and Universities (PID2019-108902GB-I00). G. Walz reports being a scientific advisor for or member of the Meona Group. N. Endlich declares that PEMP, which has been used for this manuscript, is registered for a patent; reports being among the founders of the start-up NIPOKA, which commercializes PEMP; and reports having an advisory or leadership role as a Plos One Editor. T. Benzing reports consultancy through advisory activity for Otsuka in the field of cystic kidney disease and hyponatremia; reports receiving research funding for the autosomal dominant polycystic kidney disease registry by Otsuka; reports receiving honoraria and travel support from Amgen, Hexal, Novartis, Otsuka, Roche, and Sanofi-Genzyme; and reports having an advisory or leadership role on the Editorial Board of *JASN*, Nephrology Dialysis Transplantation, and Science Signaling. T. Huber reports being a consultant for AstraZeneca, Bayer, Boehringer-Ingelheim, DaVita, Deerfield, Fresenius Medical Care, GoldfinchBio, Mantrabio, Novartis, and Retrophin; reports receiving research funding from Amicus Therapeutics, Fresenius Medical Care; reports receiving honoraria from AstraZeneca, Bayer, Boehringer-Ingelheim, DaVita, Deerfield, Fresenius Medical Care, GoldfinchBio, Mantrabio, Novartis, and Retrophin; and reports having an advisory or leadership role with *Kidney International* (Editorial Board); *Nature Review Nephrology* (Journal, Advisory Board). All remaining authors have nothing to disclose.

FUNDING

This study was supported by the German Research Foundation (Deutsche Forschungsgemeinschaft, SCHE 2092/1-2, SCHE 2092/3-1, SCHE 2092/4-1 [RP9, CP2, CP3] and CRU329, Project-ID 43198400-SFB1453 (to C. Schell), CRC1192–HU1016/8-2, HU1016/11, HU 1016/12-1 (to T. Huber), CRU329 (to T. Benzing), the Else Kröner-Fresenius-Stiftung (2016_Kolleg.03 to M. Rogg), the Federal Ministry of Education and

Research (BMBF grant STOP-FSGS 01GM101C, 01GM1518B (to N. Endlich and T. Huber), Freiburg Institute for Advanced Studies (FRIAS) within the research focus MatrixCode (to C. Schell) and Else Kröner-Fresenius-Stiftung Matriglom (EKFS A_09 to C. Schell).

ACKNOWLEDGMENTS

We would like to thank Katja Gräwe, Severine Kayser, and Charlotte Meyer for expert technical assistance. We thank Veran Drenic and Nihal Telli (NIPOKA) for excellent work regarding SIM imaging. The ERCB-KFB was supported by the Else Kröner-Fresenius Foundation. We also thank all participating centers of the ERCB-KFB and their patients for their cooperation. For active members at the time of the study see ref.⁷⁸ In addition, we would like to express our gratitude to all members of our laboratories for helpful discussions and support.

AUTHOR CONTRIBUTIONS

M. Rogg and C. Schell conceptualized the study; J. I. Maier, M. Lindenmeyer and M. Rogg were responsible for data curation; N. Endlich, J. I. Maier, M. Rogg, and C. Schell were responsible for formal analysis; C. Schell was responsible for the funding acquisition; M. Helmstädter, J. I. Maier, M. Rogg, A. Sammarco, C. Schell, C. Van Wymersch, and P. Zareba were responsible for the investigation; T. Benzing, N. Endlich, M. Lindenmeyer, E. Montanez, and M. Rogg were responsible for the methodology; T. Benzing, T. B. Huber, M. Lindenmeyer, E. Montanez, G. Walz, and M. Werner were responsible for the resources; C. Schell provided supervision; M. Rogg was responsible for the validation and visualization; and M. Rogg and C. Schell wrote the original draft and reviewed and edited the manuscript.

SUPPLEMENTAL MATERIAL

This article contains the following supplemental material online at <http://jasn.asnjournals.org/lookup/suppl/doi:10.1681/ASN.2021101319/-/DCSupplemental>.

Supplemental Figure 1. Representative stainings for ITAM analysis, corresponding to Figure 1.

Supplemental Figure 2. Illustration of the mapped podocyte adhesome, corresponding to Figure 1.

Supplemental Figure 3. Histological analysis of *Parva* KO mice, corresponding to Figure 2.

Supplemental Figure 4. 4i multiplex imaging of *Parva* KO mice, corresponding to Figure 2.

Supplemental Figure 5. 3D-SIM and TEM analysis of *Parva* KO mice, corresponding to Figure 3.

Supplemental Figure 6. Analysis of human *PARVA* KO podocytes, corresponding to Figure 4.

Supplemental Figure 7. Analysis of primary murine *Parva* KO podocytes, corresponding to Figure 4.

Supplemental Figure 8. IPP complex analysis in *Parva* KO mice, corresponding to Figure 5.

Supplemental Figure 9. Functional analysis of *PARVA/B* dKO cells, corresponding to Figure 6.

Supplemental Figure 10. Functional analysis of *PARVA/B* dKO cells, corresponding to Figures 6 and 7.

Supplemental Figure 11. Functional analysis of *PARVA/B* dKO cells, corresponding to Figure 7.

Supplemental Figure 12. Functional analysis of *PARVA/B* dKO cells, corresponding to Figure 7.

Supplemental Figure 13. IAC component analysis in *Parva* KO mice, corresponding to Figure 8.

Supplemental Figure 14. Schematic.

Supplemental Table 1. Antibodies.

Supplemental Table 2. RNAseq: Adhesome analysis of *Parva* KO mice, corresponding to Figure 5.

Supplemental Table 3. Correlation analysis, corresponding to Figure 1.

Supplemental Table 4. Statistical methods.

Supplemental Dataset 1. RNAseq of *Parva* KO mice.

REFERENCES

- Grahammer F, Schell C, Huber TB: The podocyte slit diaphragm—from a thin grey line to a complex signalling hub. *Nat Rev Nephrol* 9: 587–598, 2013
- Benzing T, Salant D: Insights into glomerular filtration and albuminuria. *N Engl J Med* 384: 1437–1446, 2021
- Trimarchi H: Mechanisms of podocyte detachment, podocyturia, and risk of progression of glomerulopathies. *Kidney Dis* 6: 324–329, 2020
- Kriz W, Lemley KV: A potential role for mechanical forces in the detachment of podocytes and the progression of CKD. *J Am Soc Nephrol* 26: 258–269, 2015
- Sever S, Schiffer M: Actin dynamics at focal adhesions: A common endpoint and putative therapeutic target for proteinuric kidney diseases. *Kidney Int* 93: 1298–1307, 2018
- Lennon R, Randles MJ, Humphries MJ: The importance of podocyte adhesion for a healthy glomerulus. *Front Endocrinol (Lausanne)* 5: 160, 2014
- Humphries JD, Chastney MR, Askari JA, Humphries MJ: Signal transduction via integrin adhesion complexes. *Curr Opin Cell Biol* 56: 14–21, 2019
- Horton ER, Byron A, Askari JA, Ng DHJ, Millon-Frémillon A, Robertson J, et al.: Definition of a consensus integrin adhesome and its dynamics during adhesion complex assembly and disassembly. *Nat Cell Biol* 17: 1577–1587, 2015
- Chastney MR, Lawless C, Humphries JD, Warwood S, Jones MC, Knight D, et al.: Topological features of integrin adhesion complexes revealed by multiplexed proximity biotinylation. *J Cell Biol* 219: 202003038, 2020
- Michael M, Parsons M: New perspectives on integrin-dependent adhesions. *Curr Opin Cell Biol* 63: 31–37, 2020
- Has C, Spartà G, Kiritsi D, Weibel L, Moeller A, Vega-Warner V, et al.: Integrin $\alpha 3$ mutations with kidney, lung, and skin disease. *N Engl J Med* 366: 1508–1514, 2012
- Karamatic Crew V, Burton N, Kagan A, Green CA, Levene C, Flinter F, et al.: CD151, the first member of the tetraspanin (TM4) superfamily detected on erythrocytes, is essential for the correct assembly of human basement membranes in kidney and skin. *Blood* 104: 2217–2223, 2004
- Kaplan JM, Kim SH, North KN, Renke H, Correia LA, Tong HQ, et al.: Mutations in ACTN4, encoding alpha-actinin-4, cause familial focal segmental glomerulosclerosis. *Nat Genet* 24: 251–256, 2000
- Schell C, Rogg M, Suhm M, Helmstädter M, Sellung D, Yasuda-Yamahara M, et al.: The FERM protein EPB41L5 regulates actomyosin contractility and focal adhesion formation to maintain the kidney filtration barrier. *Proc Natl Acad Sci U S A* 114: E4621–E4630, 2017
- Rogg M, Yasuda-Yamahara M, Abed A, Dinse P, Helmstädter M, Conzelmann AC, et al.: The WD40-domain containing protein CORO2B is specifically enriched in glomerular podocytes and regulates the ventral actin cytoskeleton. *Sci Rep* 7: 15910, 2017
- Yasuda-Yamahara M, Rogg M, Yamahara K, Maier JI, Huber TB, Schell C: AIF1L regulates actomyosin contractility and filopodial extensions in human podocytes. *PLoS One* 13: e0200487, 2018
- Yasuda-Yamahara M, Rogg M, Frimmel J, Trachte P, Helmstädter M, Schroder P, et al.: FERMT2 links cortical actin structures, plasma membrane tension and focal adhesion function to stabilize podocyte morphology. *Matrix Biol* 68–69: 263–279, 2018
- Randles MJ, Lausecker F, Humphries JD, Byron A, Clark SJ, Miner JH, et al.: Basement membrane ligands initiate distinct signalling networks to direct cell shape. *Matrix Biol* 90: 61–78, 2020
- Schell C, Huber TB: The evolving complexity of the podocyte cytoskeleton. *J Am Soc Nephrol* 28: 3166–3174, 2017
- Kriz W, Shirato I, Nagata M, Le Hir M, Lemley KV: The podocyte's response to stress: The enigma of foot process effacement. *Am J Physiol Renal Physiol* 304: F333–F347, 2013
- Schell C, Sabass B, Helmstaedter M, Geist F, Abed A, Yasuda-Yamahara M, et al.: ARP3 controls the podocyte architecture at the kidney filtration barrier. *Dev Cell* 47: 741–757.e8, 2018
- Matsuda J, Asano-Matsuda K, Kitzler TM, Takano T: Rho GTPase regulatory proteins in podocytes. *Kidney Int* 99: 336–345, 2021
- Schiffer M, Teng B, Gu C, Shchedrina VA, Kasaikina M, Pham VA, et al.: Pharmacological targeting of actin-dependent dynamin oligomerization ameliorates chronic kidney disease in diverse animal models. *Nat Med* 21: 601–609, 2015
- Dai C, Stolz DB, Bastacky SI, St-Arnaud R, Wu C, Dedhar S, et al.: Essential role of integrin-linked kinase in podocyte biology: Bridging the integrin and slit diaphragm signaling. *J Am Soc Nephrol* 17: 2164–2175, 2006
- El-Aouini C, Herbach N, Blattner SM, Henger A, Rastaldi MP, Jarad G, et al.: Podocyte-specific deletion of integrin-linked kinase results in severe glomerular basement membrane alterations and progressive glomerulosclerosis. *J Am Soc Nephrol* 17: 1334–1344, 2006
- Vaynberg J, Fukuda K, Lu F, Bialkowska K, Chen Y, Plow EF, et al.: Non-catalytic signaling by pseudokinase ILK for regulating cell adhesion. *Nat Commun* 9: 4465, 2018
- Ghatak S, Morgner J, Wickström SA: ILK: A pseudokinase with a unique function in the integrin-actin linkage. *Biochem Soc Trans* 41: 995–1001, 2013
- Lange A, Wickström SA, Jakobson M, Zent R, Sainio K, Fässler R: Integrin-linked kinase is an adaptor with essential functions during mouse development. *Nature* 461: 1002–1006, 2009
- Mishra YG, Manavathi B: Focal adhesion dynamics in cellular function and disease. *Cell Signal* 85: 110046, 2021
- Revach OY, Grosheva I, Geiger B: Biomechanical regulation of focal adhesion and invadopodia formation. *J Cell Sci* 133: jcs244848, 2020
- Olski TM, Noegel AA, Korenbaum E: Parvin, a 42 kDa focal adhesion protein, related to the alpha-actinin superfamily. *J Cell Sci* 114: 525–538, 2001
- Fraccaroli A, Pitter B, Taha AA, Seebach J, Huvneers S, Kirsch J, et al.: Endothelial alpha-parvin controls integrity of developing vasculature and is required for maintenance of cell-cell junctions. *Circ Res* 117: 29–40, 2015
- Moeller MJ, Sanden SK, Soofi A, Wiggins RC, Holzman LB: Two gene fragments that direct podocyte-specific expression in transgenic mice. *J Am Soc Nephrol* 13: 1561–1567, 2002
- Schell C, Kretz O, Bregenzner A, Rogg M, Helmstädter M, Lisewski U, et al.: Podocyte-specific deletion of murine CXADR does not impair podocyte development, function or stress response. *PLoS One* 10: e0129424, 2015
- Maier JI, Rogg M, Helmstädter M, Sammarco A, Walz G, Werner M, et al.: A novel model for nephrotic syndrome reveals associated dysbiosis of the gut microbiome and extramedullary hematopoiesis. *Cells* 10: 1509, 2021
- Butt L, Unnersjö-Jess D, Höhne M, Edwards A, Binz-Lotter J, Reilly D, et al.: A molecular mechanism explaining albuminuria in kidney disease. *Nat Metab* 2: 461–474, 2020
- Saleem MA, O'Hare MJ, Reiser J, Coward RJ, Inward CD, Farren T, et al.: A conditionally immortalized human podocyte cell line demonstrating nephrin and podocin expression. *J Am Soc Nephrol* 13: 630–638, 2002

38. Maier JI, Rogg M, Helmstädter M, Sammarco A, Schilling O, Sabass B, et al.: EPB41L5 controls podocyte extracellular matrix assembly by adhesion-dependent force transmission. *Cell Rep* 34: 108883, 2021
39. Labun K, Montague TG, Krause M, Torres Cleuren YN, Tjeldnes H, Valen E: CHOPCHOP v3: Expanding the CRISPR web toolbox beyond genome editing. *Nucleic Acids Res* 47[W1]: W171–W174, 2019
40. Barger CJ, Branick C, Chee L, Karpf AR: Pan-cancer analyses reveal genomic features of FOXM1 overexpression in cancer. *Cancers (Basel)* 11: 251, 2019
41. Doench JG, Fusi N, Sullender M, Hegde M, Vaimberg EW, Donovan KF, et al.: Optimized sgRNA design to maximize activity and minimize off-target effects of CRISPR-Cas9. *Nat Biotechnol* 34: 184–191, 2016
42. el Nahas AM, Bassett AH, Cope GH, Le Carpentier JE: Role of growth hormone in the development of experimental renal scarring. *Kidney Int* 40: 29–34, 1991
43. Bienaimé F, Muorah M, Yammine L, Burtin M, Nguyen C, Baron W, et al.: Stat3 controls tubulointerstitial communication during CKD. *J Am Soc Nephrol* 27: 3690–3705, 2016
44. Mariani LH, Martini S, Barisoni L, Canetta PA, Troost JP, Hodgins JB, et al.: Interstitial fibrosis scored on whole-slide digital imaging of kidney biopsies is a predictor of outcome in proteinuric glomerulopathies. *Nephrol Dial Transplant* 33: 310–318, 2018
45. Venkatarreddy M, Wang S, Yang Y, Patel S, Wickman L, Nishizono R, et al.: Estimating podocyte number and density using a single histologic section. *J Am Soc Nephrol* 25: 1118–1129, 2014
46. Gut G, Herrmann MD, Pelkmans L: Multiplexed protein maps link sub-cellular organization to cellular states. *Science* 361: eear7042, 2018
47. Bankhead P, Loughrey MB, Fernández JA, Dombrowski Y, McArt DG, Dunne PD, et al.: QuPath: Open source software for digital pathology image analysis. *Sci Rep* 7: 16878, 2017
48. Rogg M, Maier JI, Dotzauer R, Artelt N, Kretz O, Helmstädter M, et al.: SRGAP1 controls small Rho GTPases to regulate podocyte foot process maintenance. *J Am Soc Nephrol* 32: 563–579, 2021
49. Rinschen MM, Gödel M, Grahmmer F, Zschiedrich S, Helmstädter M, Kretz O, et al.: A multi-layered quantitative in vivo expression atlas of the podocyte unravels kidney disease candidate genes. *Cell Rep* 23: 2495–2508, 2018
50. Hatje FA, Wedekind U, Sachs W, Loreth D, Reichelt J, Demir F, et al.: Tripartite separation of glomerular cell types and proteomes from reporter-free mice. *J Am Soc Nephrol* 32: 2175–2193, 2021
51. Kaverina I, Krylyshkina O, Small JV: Microtubule targeting of substrate contacts promotes their relaxation and dissociation. *J Cell Biol* 146: 1033–1044, 1999
52. Ezratty EJ, Partridge MA, Gundersen GG: Microtubule-induced focal adhesion disassembly is mediated by dynamin and focal adhesion kinase. *Nat Cell Biol* 7: 581–590, 2005
53. Lavelin I, Wolfenson H, Patla I, Henis YI, Medalia O, Volberg T, et al.: Differential effect of actomyosin relaxation on the dynamic properties of focal adhesion proteins. *PLoS One* 8: e73549, 2013
54. Stanchi F, Grashoff C, Nguemeni Yonga CF, Grall D, Fässler R, Van Obberghen-Schilling E: Molecular dissection of the ILK-PINCH-parvin triad reveals a fundamental role for the ILK kinase domain in the late stages of focal-adhesion maturation. *J Cell Sci* 122: 1800–1811, 2009
55. Boerries M, Grahmmer F, Eiselein S, Buck M, Meyer C, Goedel M, et al.: Molecular fingerprinting of the podocyte reveals novel gene and protein regulatory networks. *Kidney Int* 83: 1052–1064, 2013
56. Afgan E, Baker D, van den Beek M, Blankenberg D, Bouvier D, Čech M, et al.: The Galaxy platform for accessible, reproducible and collaborative biomedical analyses: 2016 update. *Nucleic Acids Res* 44[W1]: W3–W10, 2016
57. Kim D, Langmead B, Salzberg SL: HISAT: A fast spliced aligner with low memory requirements. *Nat Methods* 12: 357–360, 2015
58. Liao Y, Smyth GK, Shi W: featureCounts: An efficient general purpose program for assigning sequence reads to genomic features. *Bioinformatics* 30: 923–930, 2014
59. Love MI, Huber W, Anders S: Moderated estimation of fold change and dispersion for RNA-seq data with DESeq2. *Genome Biol* 15: 550, 2014
60. Cohen CD, Frach K, Schlöndorff D, Kretzler M: Quantitative gene expression analysis in renal biopsies: A novel protocol for a high-throughput multicenter application. *Kidney Int* 61: 133–140, 2002
61. Cohen CD, Klingenhoff A, Boucherot A, Nitsche A, Henger A, Brunner B, et al.: Comparative promoter analysis allows de novo identification of specialized cell junction-associated proteins. *Proc Natl Acad Sci U S A* 103: 5682–5687, 2006
62. Tusher VG, Tibshirani R, Chu G: Significance analysis of microarrays applied to the ionizing radiation response. *Proc Natl Acad Sci U S A* 98: 5116–5121, 2001
63. Altstätter J, Hess MW, Costell M, Montanez E: α -parvin is required for epidermal morphogenesis, hair follicle development and basal keratinocyte polarity. *PLoS One* 15: e0230380, 2020
64. Lehtimäki JI, Rajakylä EK, Tojkander S, Lappalainen P: Generation of stress fibers through myosin-driven reorganization of the actin cortex. *eLife* 10: e60710, 2021
65. BurrIDGE K, Guilluy C: Focal adhesions, stress fibers and mechanical tension. *Exp Cell Res* 343: 14–20, 2016
66. Huet-Calderwood C, Brahmé NN, Kumar N, Stiegler AL, Raghavan S, Boggon TJ, et al.: Differences in binding to the ILK complex determines kindlin isoform adhesion localization and integrin activation. *J Cell Sci* 127: 4308–4321, 2014
67. Naik AS, Le D, Aqeel J, Wang SQ, Chowdhury M, Walters LM, et al.: Podocyte stress and detachment measured in urine are related to mean arterial pressure in healthy humans. *Kidney Int* 98: 699–707, 2020
68. Feng D, Notbohm J, Benjamin A, He S, Wang M, Ang LH, et al.: Disease-causing mutation in α -actinin-4 promotes podocyte detachment through maladaptation to periodic stretch. *Proc Natl Acad Sci U S A* 115: 1517–1522, 2018
69. Feng D, DuMontier C, Pollak MR: Mechanical challenges and cytoskeletal impairments in focal segmental glomerulosclerosis. *Am J Physiol Renal Physiol* 314: F921–F925, 2018
70. Zhang Y, Chen K, Tu Y, Wu C: Distinct roles of two structurally closely related focal adhesion proteins, alpha-parvins and beta-parvins, in regulation of cell morphology and survival. *J Biol Chem* 279: 41695–41705, 2004
71. Shirato I, Sakai T, Kimura K, Tomino Y, Kriz W: Cytoskeletal changes in podocytes associated with foot process effacement in Masugi nephritis. *Am J Pathol* 148: 1283–1296, 1996
72. Suleiman HY, Roth R, Jain S, Heuser JE, Shaw AS, Miner JH: Injury-induced actin cytoskeleton reorganization in podocytes revealed by super-resolution microscopy. *JCI Insight* 2: e94137, 2017
73. Smith MA, Blankman E, Gardel ML, Luettjohann L, Waterman CM, Beckerle MC: A zyxin-mediated mechanism for actin stress fiber maintenance and repair. *Dev Cell* 19: 365–376, 2010
74. Hoffman LM, Jensen CC, Chaturvedi A, Yoshigi M, Beckerle MC: Stretch-induced actin remodeling requires targeting of zyxin to stress fibers and recruitment of actin regulators. *Mol Biol Cell* 23: 1846–1859, 2012
75. Goode NP, Shires M, Khan TN, Mooney AF: Expression of alpha-actinin-4 in acquired human nephrotic syndrome: A quantitative immunoelectron microscopy study. *Nephrol Dial Transplant* 19: 844–851, 2004
76. Smoyer WE, Mundel P, Gupta A, Welsh MJ: Podocyte alpha-actinin induction precedes foot process effacement in experimental nephrotic syndrome. *Am J Physiol* 273: F150–F157, 1997
77. Dandapani SV, Sugimoto H, Matthews BD, Kolb RJ, Sinha S, Gerszten RE, et al.: Alpha-actinin-4 is required for normal podocyte adhesion. *J Biol Chem* 282: 467–477, 2007
78. Shved N, Warsaw G, Eichinger F, Hoogewijs D, Brandt S, Wild P, et al.: Transcriptome-based network analysis reveals renal cell type-specific dysregulation of hypoxia-associated transcripts. *Sci Rep* 7: 8576, 2017

AFFILIATIONS

¹Institute of Surgical Pathology, Faculty of Medicine, Medical Center-University of Freiburg, Freiburg, Germany

²Department of Medicine IV, Faculty of Medicine, Medical Center-University of Freiburg, Freiburg, Germany

³III. Department of Medicine, University Medical Center Hamburg-Eppendorf, Hamburg, Germany

⁴Department of Physiological Sciences, Faculty of Medicine, University of Barcelona and Health Sciences and Bellvitge Biomedical Research Institute (IDIBELL), Barcelona, Spain

⁵Department of Anatomy and Cell Biology, University Medicine Greifswald, Greifswald, Germany

⁶Center of High-End Imaging, NIPOKA GmbH, Greifswald, Germany

⁷Department II of Internal Medicine and Center for Molecular Medicine Cologne, University of Cologne, Faculty of Medicine and University Hospital Cologne, Cologne, Germany

⁸Freiburg Institute for Advanced Studies (FRIAS), University of Freiburg, Freiburg, Germany

Supplemental Table of Contents

- Supplemental Figure S1. Representative stainings for ITAM analysis, corresponding to Figure 1.
- Supplemental Figure S2. Illustration of the mapped podocyte adhesome, corresponding to Figure 1.
- Supplemental Figure S3. Histological analysis of *Parva* KO mice, corresponding to Figure 2.
- Supplemental Figure S4. 4i multiplex imaging of *Parva* KO mice, corresponding to Figure 2.
- Supplemental Figure S5. 3D-SIM and TEM analysis of *Parva* KO mice, corresponding to Figure 3.
- Supplemental Figure S6. Analysis of human *PARVA* KO podocytes, corresponding to Figure 4.
- Supplemental Figure S7. Analysis of primary murine *Parva* KO podocytes, corresponding to Figure 4.
- Supplemental Figure S8. IPP complex analysis in *Parva* KO mice, corresponding to Figure 5.
- Supplemental Figure S9. Functional analysis of *PARVA/B* dKO cells, corresponding to Figure 6.
- Supplemental Figure S10. Functional analysis of *PARVA/B* dKO cells, corresponding to Figure 6&7.
- Supplemental Figure S11. Functional analysis of *PARVA/B* dKO cells, corresponding to Figure 7.
- Supplemental Figure S12. Functional analysis of *PARVA/B* dKO cells, corresponding to Figure 7.
- Supplemental Figure S13. IAC component analysis in *Parva* KO mice, corresponding to Figure 8.
- Supplemental Figure S14. Schematic.
- Table S1. Antibodies.
- Table S2. RNAseq: Adhesome analysis of *Parva* KO mice, corresponding to Figure 5.
- Table S3. Correlation analysis, corresponding to Figure 1.
- Table S4. Statistical Methods.
- Dataset S1. RNAseq of *Parva* KO mice.

Supplemental Figures

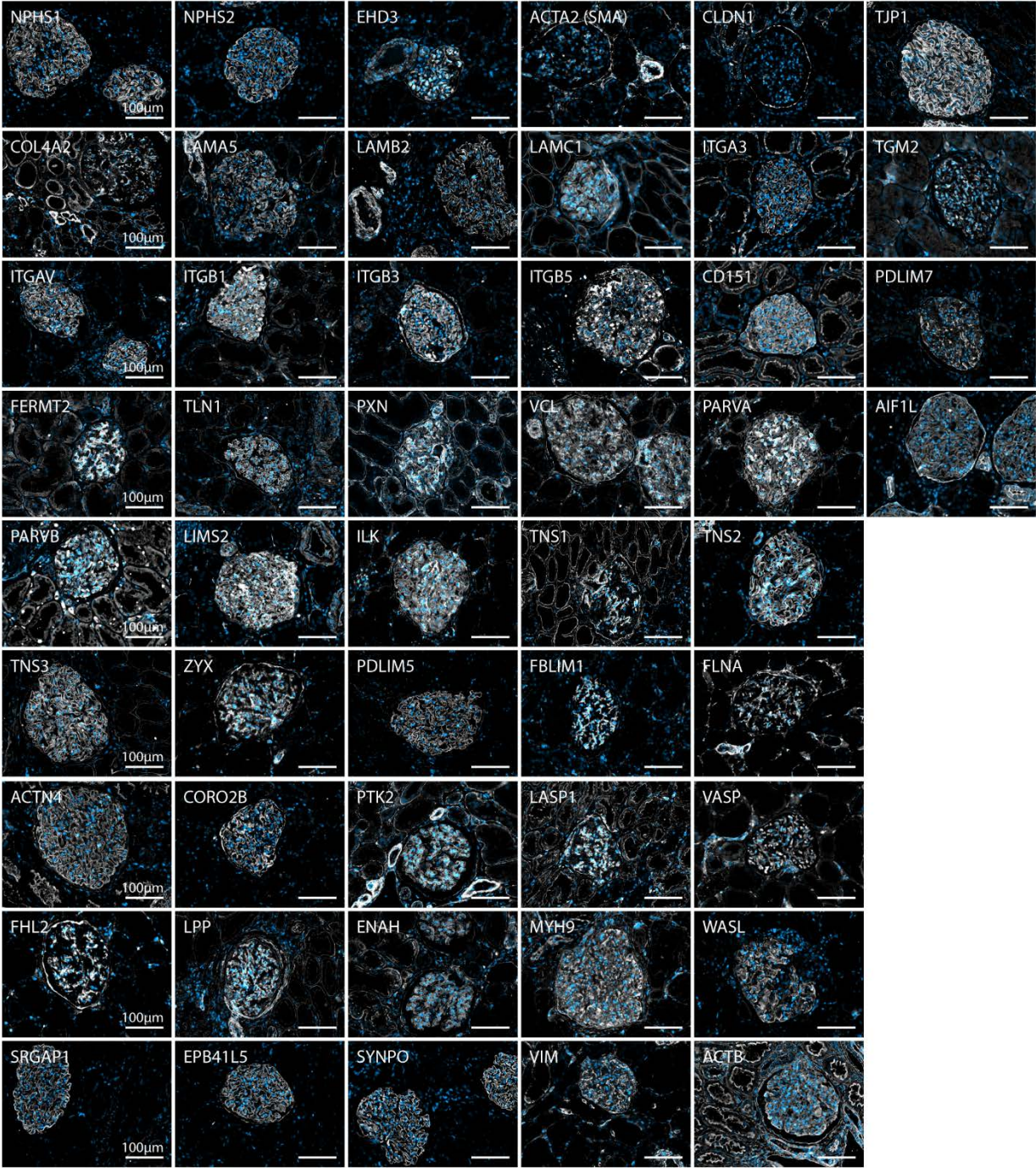
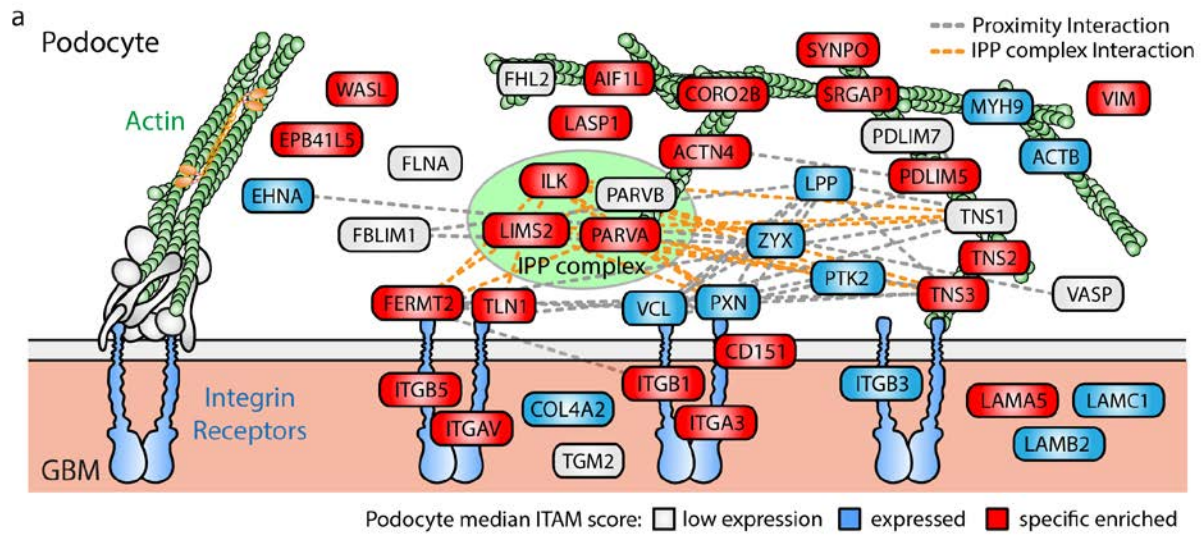


Figure S1. Individual antibody stainings corresponding to main Figure 1. Collage depicting representative immunofluorescence stainings for assessed and evaluated integrin adhesome (related) proteins and compartment markers on human kidney tissue (Hoechst 33258 stain was used as a counterstain for cell nuclei – all other stainings are presented in grey as indicated).



b single channels corresponding to Figure 1c

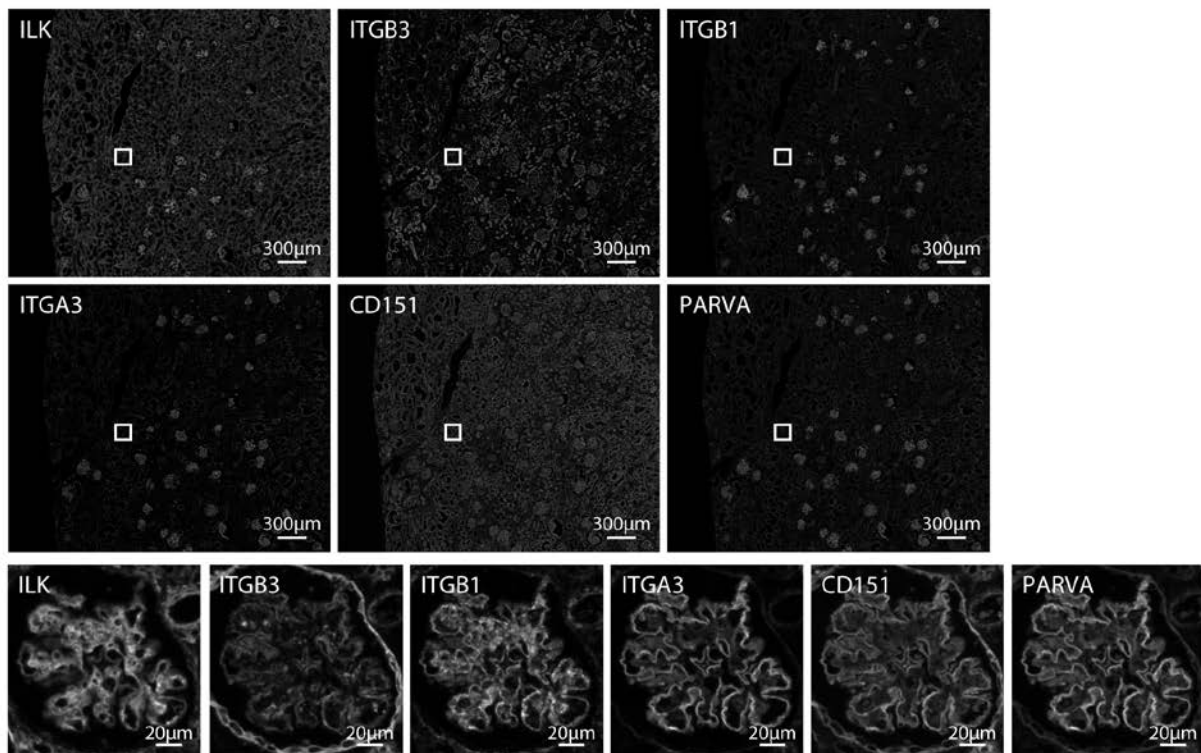


Figure S2. Individual antibody stainings corresponding to main Figure 1. **(A)** Illustration of podocyte adhesome proteins (color-coded) according to ITAM scoring were analyzed for described protein-protein interactions. The IPP complex appeared as a central node embedded within the adhesome protein network. IAC components were defined as low expressed, expressed or specifically enriched based on the median ITAM score for the podocyte compartment as presented in Figure 1 (expression categories were color-coded as indicated; please see methods section for classification criteria). **(B)** Single channels corresponding to multiplex analysis in main Figure 1C. Representative podocyte IAC components were stained on human kidney tissue (white boxes indicate zoom-in regions).

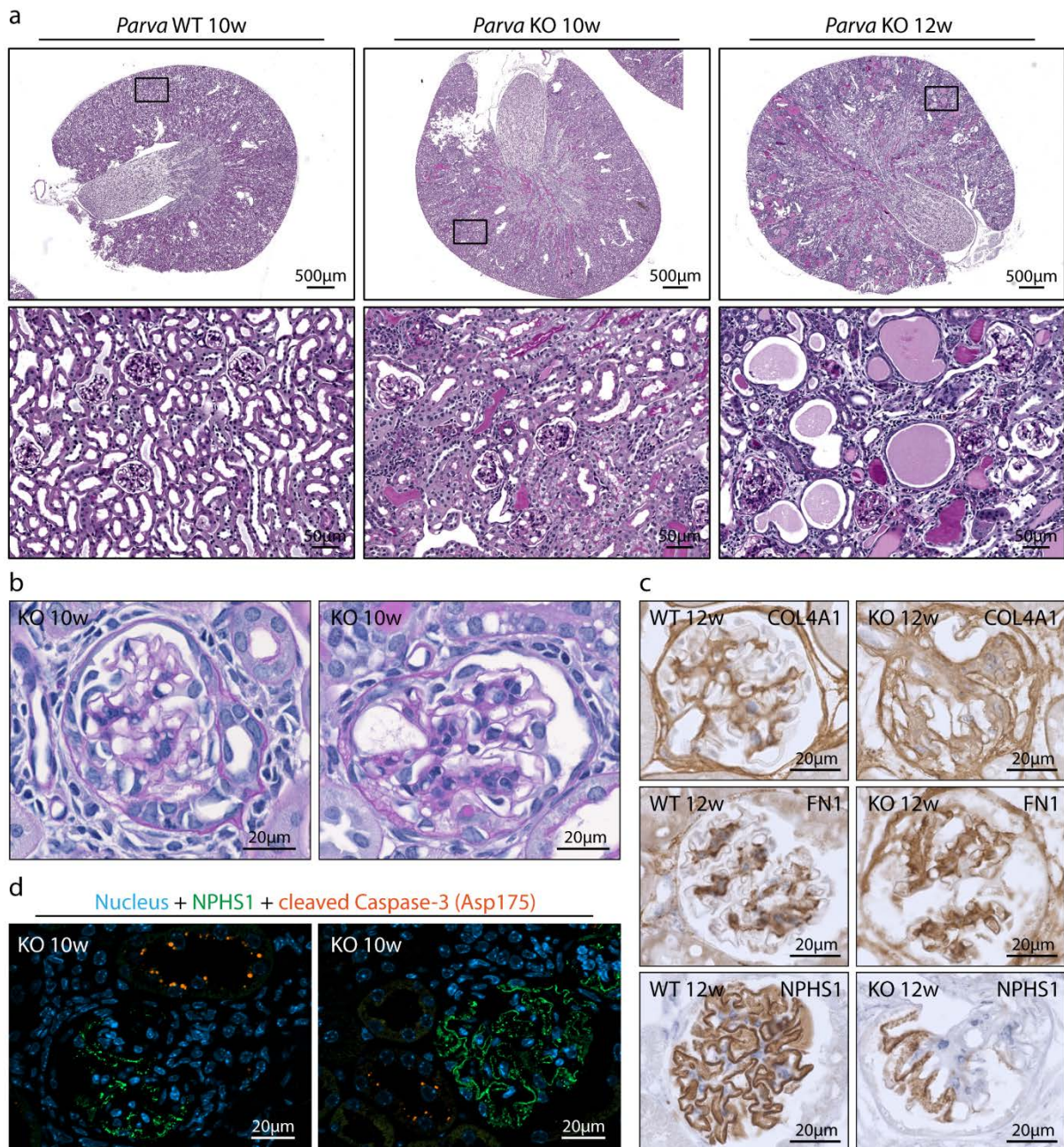


Figure S3. Additional data corresponding to main Figure 2. **(A&B)** PAS staining of *Parva* WT and KO mice (black boxes indicate zoom-in regions). *Parva* KOs showed proteinaceous casts, progressing tubular dilation as well as interstitial infiltration of lymphocytes. Glomeruli showed dilated capillaries, moderate mesangial sclerosis and focal proliferation of parietal epithelial cells. **(C)** Immunohistochemistry on 12-week-old *Parva* KO mice demonstrated increased deposition of FN1 as well as COL4A1 within the mesangium and scarred regions of affected glomeruli. With ongoing sclerosis, also staining levels for the slit diaphragm marker NPHS1 decreased. **(D)** Representative staining for cleaved Caspase-3 indicated apoptosis in the tubular but not in the podocyte compartment of *Parva* KO mice (podocytes were co-stained by NPHS1 and nuclei by Hoechst).

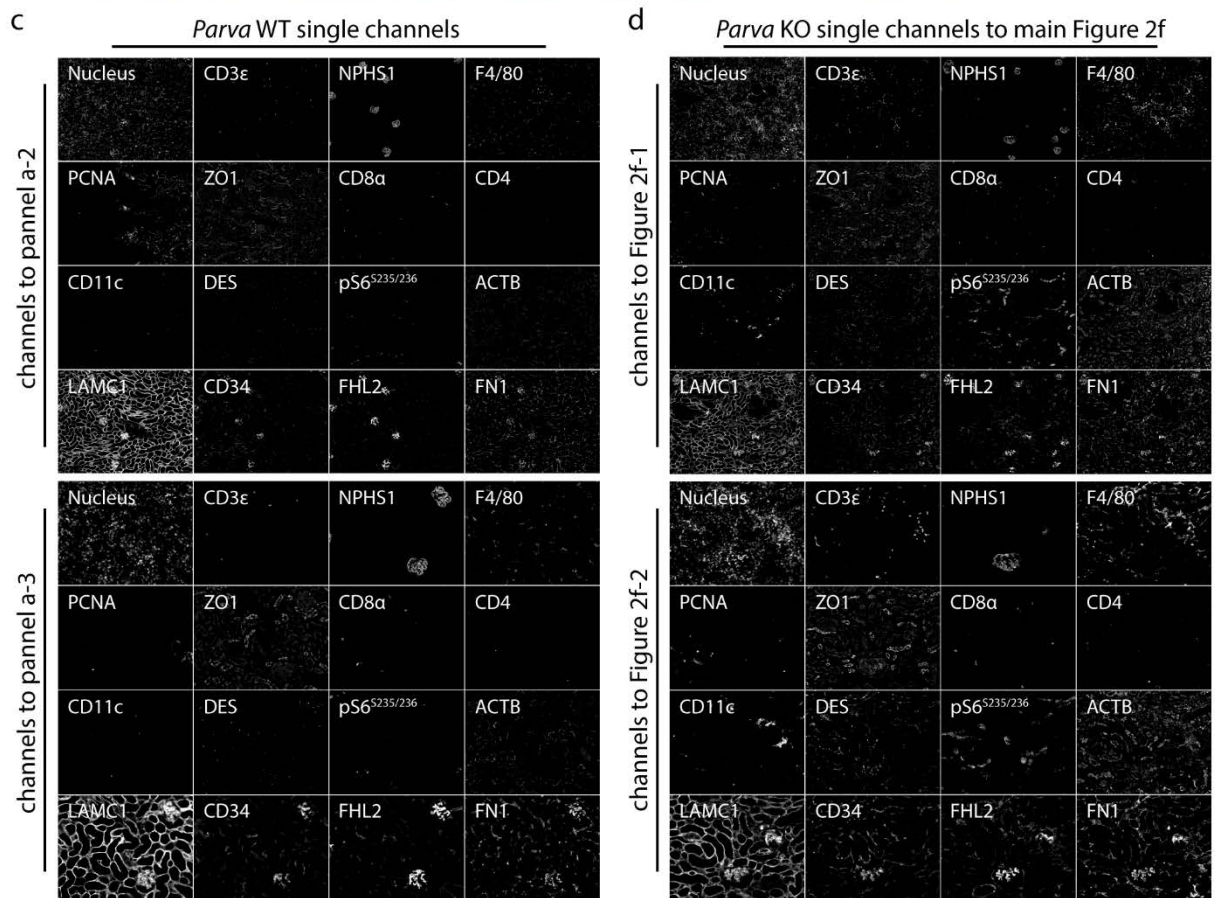
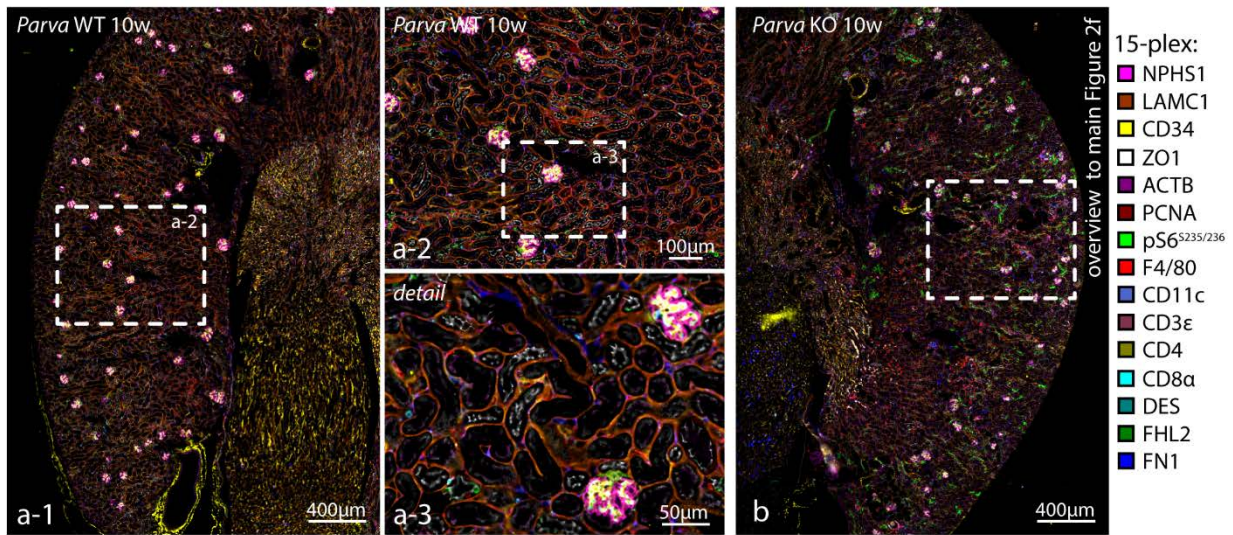


Figure S4. Additional data corresponding to main Figure 2. **(A&C)** Representative multiparametric immunofluorescence staining and single channels of whole slide scanned *Parva* WT kidney is shown (white dashed boxes indicate zoom-in regions for panel A-2&A-3). **(B&D)** Overview and single channels corresponding to main Figure 2F. Representative multiparametric immunofluorescence staining of a whole slide scanned *Parva* KO kidney is shown (white dashed boxes indicate zoom-in regions presented in main Figure 2F). Panel C&D depicts individual single channels. Color coded index indicates individually assessed markers: NPHS1 – podocytes, LAMC1 – basement membranes, CD34 – endothelial cells, ZO1 (TJP1) – epithelial cells, ACTB – cellular actin cytoskeleton, PCNA – proliferating cells, pS6^{S235/236} – mTOR pathway activation, F4/80 – macrophages, CD11c – conventional dendritic cells (and to some extent NK cells & monocytes), CD3ε – T lymphocytes, CD4 – regulatory T lymphocytes, CD8α – cytotoxic T lymphocytes, DES – Desmin intermediate filament rich cells (e.g. mesangial cells and fibroblasts), FHL2 – mesangial cells and fibroblasts, FN1 (Fibronectin) – extracellular matrix.

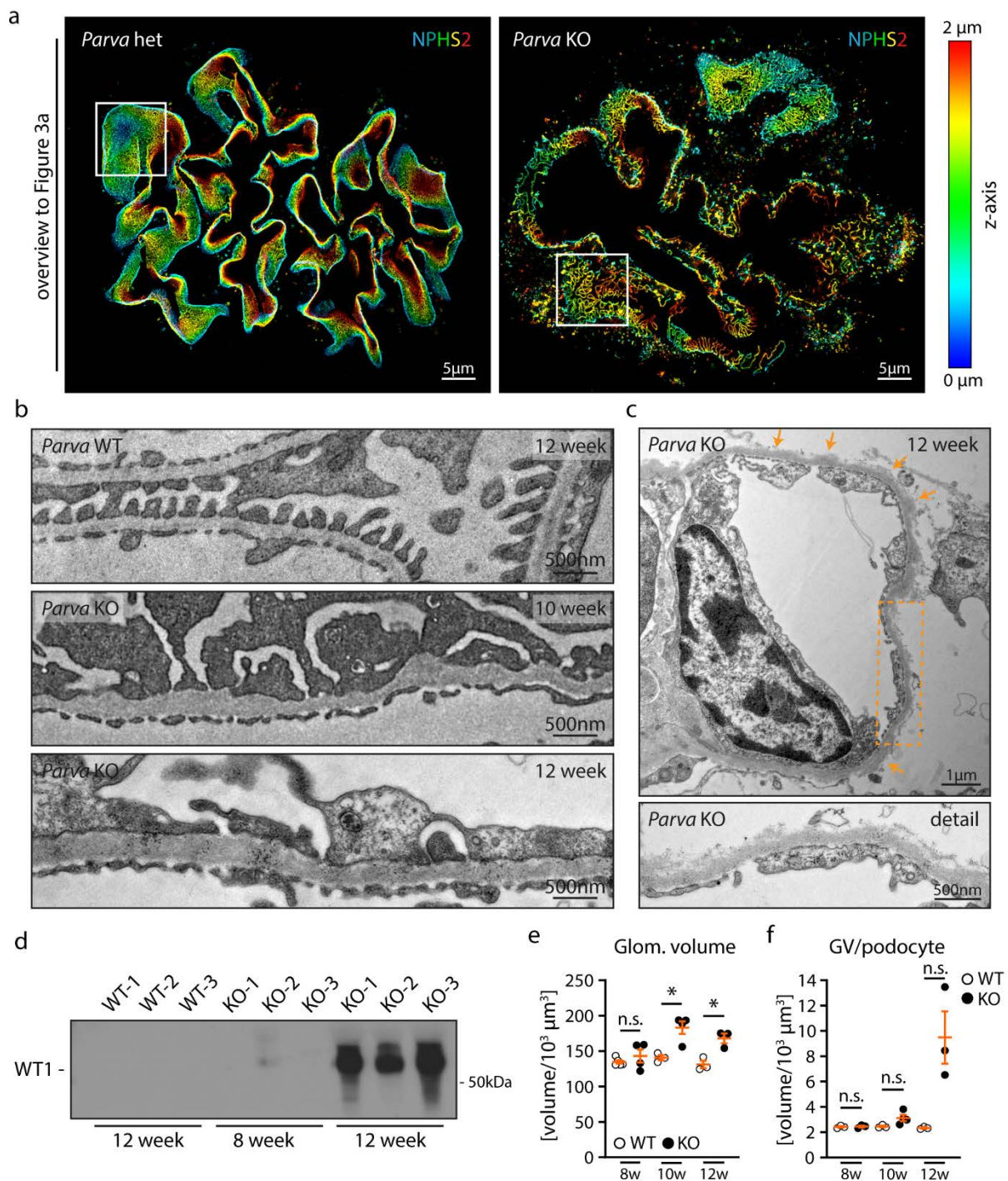
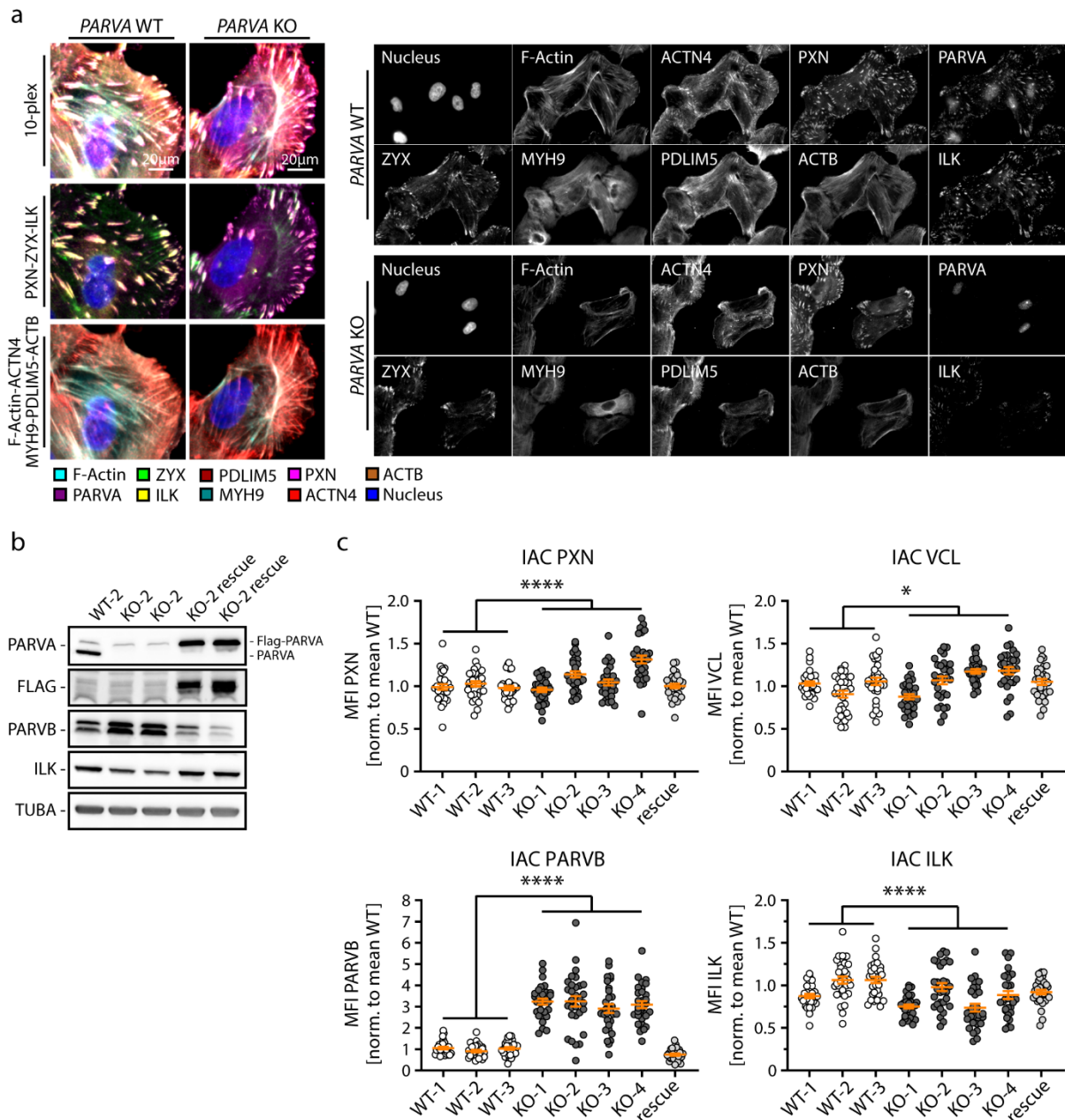


Figure S5. Additional data corresponding to main Figure 3. **(A)** Overview corresponding to main Figure 3A. 3D-SIM microscopy in respective *Parva* heterozygous (het) and KO animals identified disrupted filtration slits in KO mice. Z-axis scales of 3D-SIM were color-coded as indicated. **(B)** TEM of respective KO and WT animals demonstrated significant retraction of podocyte foot processes (FPs) and glomerular basement membrane (GBM) thickening in KO mice. **(C)** TEM at 12 weeks of age showed a pronounced denudation of the GBM due to ongoing podocyte detachment (orange dotted squared box indicates area of zoom-in; orange arrows indicate areas of completely denuded GBM). **(D)** Western blot for WT1 on urine samples derived from individual *Parva* WT and KO animals at indicated time points demonstrated shedding of WT1-positive cells with progression of the phenotype. **(E&F)** Quantification of podocyte numbers at 8, 10 and 12 weeks after birth revealed a modest increase in glomerular volume and glomerular volume per podocyte (each individual dot represents one experimental animal, at least 3 animals per time point and genotype were analyzed; * $p < 0.05$, n. s. – non-significant).



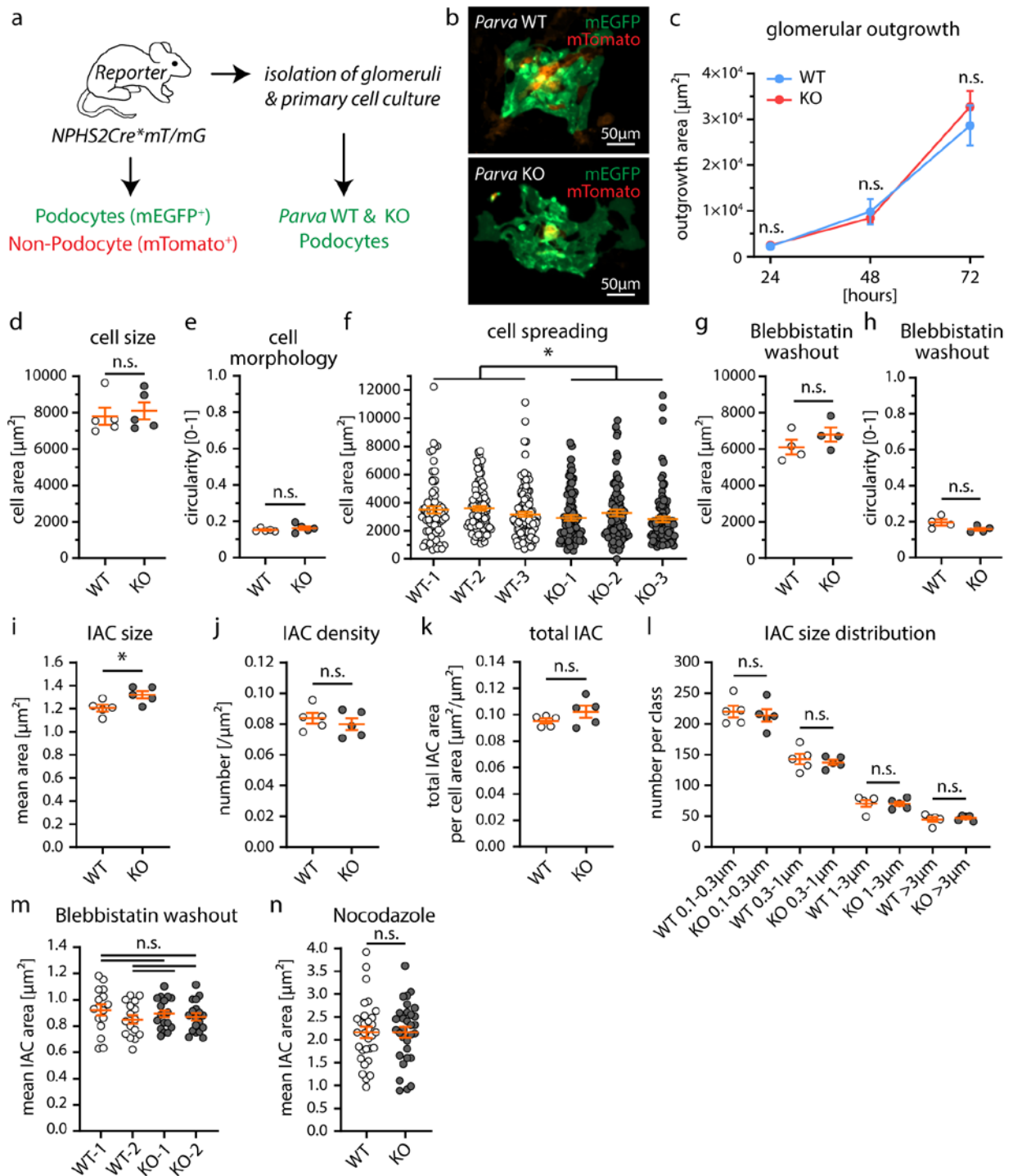


Figure S7. Additional data corresponding to main Figure 4. **(A)** Schematic illustrating the isolation of primary podocytes from *Parva* WT and KO mice using the *hNPHS2Cre**mT/mG** reporter system. **(B&C)** Glomerular outgrowth of podocytes (mEGFP positive cells) from 5 WT and 5 KO mice was not influenced by loss of PARVA. **(D&E)** Cell size and morphology did not reveal major differences between *Parva* KO podocytes and respective wild type control cells (dots indicate mean values of cells from 5 WT and 5 KO animals; at least 48 cells per animal were analyzed). **(F)** Cell spreading of primary *Parva* KO podocytes (Collagen IV, 45 minutes) was slightly reduced, but not consistently affected over all clones (dots indicate individual cells derived from 3 WT and 3 KO animals; WT and KO cells were pooled for statistical analysis; at least 70 cells per animal were analyzed). **(G&H)** Re-establishment of cell size and morphology was not impaired in primary *Parva* KO podocytes after washout of the Non-Muscle Myosin II complex inhibitor Blebbistatin. Podocytes were treated with 50 μM Blebbistatin for 60 minutes, Blebbistatin was removed (washout) and cells were analyzed after additional 60 minutes (dots indicate mean values of cells from 4 WT and 4 KO animals; at least 37 cells per animal were analyzed). **(I-L)**

Mean IAC area was slightly increased in primary *Parva* KO podocytes but neither IAC density, total IAC area nor distribution of IAC size classes was significantly affected by loss of PARVA (dots indicate mean values of cells from 5 WT and 5 KO animals, at least 16 cells per animal were analyzed). **(M)** Re-establishment of IAC size was not altered in primary KO podocytes after Non-Muscle Myosin II complex inhibition via Blebbistatin as described above (dots indicate individual cells derived from 2 WT and 2 KO animals; at least 16 cells per animal were analyzed). **(N)** IACs size was not different between WT and KO podocytes after 4 hours of 20 μ M Nocodazole treatment (dots indicate individual cells derived from 1 WT and 1 KO animal; 31 cells per animal were analyzed). * $p < 0.05$ and n. s. – non-significant.

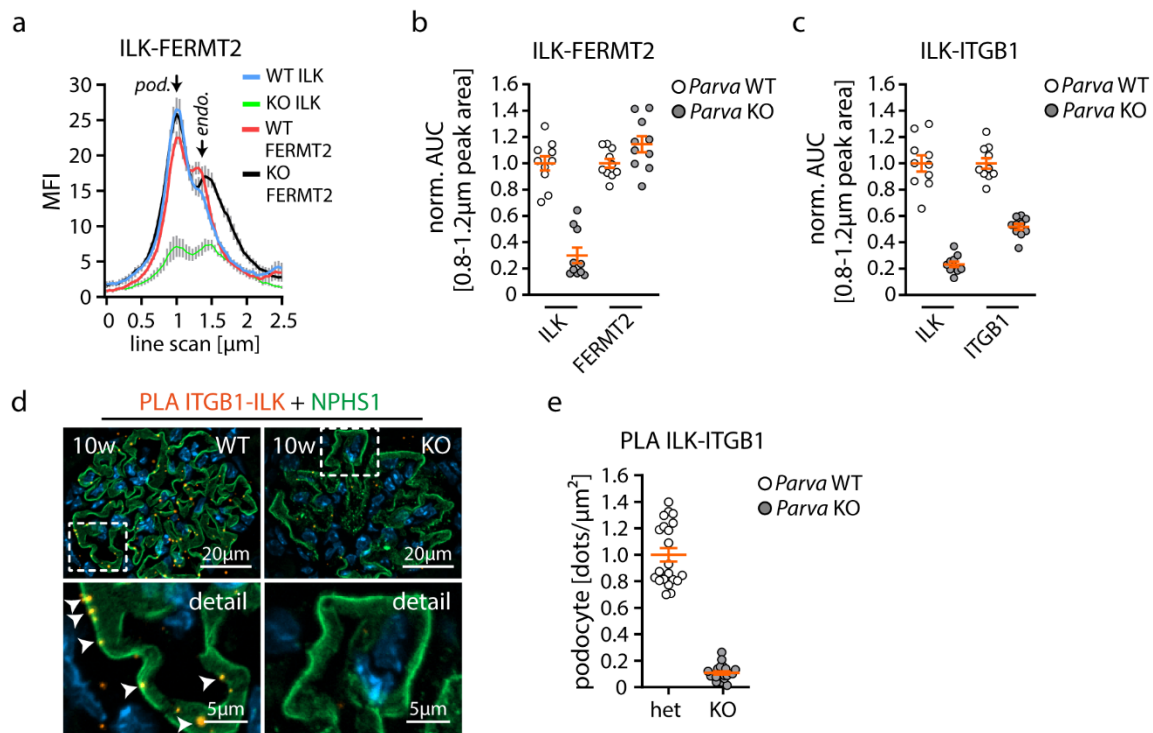


Figure S8. Additional data corresponding to main Figure 5. **(A)** Line scans demonstrate reduced glomerular podocyte ILK signals, whereas FERMT2 signal intensities were not significantly affected in *Parva* KO (representative line scan analysis of 10 glomeruli from 1 *Parva* WT and 1 KO animal; MFI - mean fluorescence intensity). **(B)** Area under the curve (AUC) analysis of line scans shown in panel A. AUCs were normalized to WT. **(C)** Area under the curve (AUC) analysis of line scans shown in main Figure 5C. AUCs were normalized to WT. **(D&E)** Proximity-ligation assays (PLAs) demonstrated a significant decrease in detectable signals for ILK-ITGB1 complexes within the podocyte compartment of respective knockout animals. NPHS1 was used as a segmentation mask for analysis of PLA dots (white arrows indicate individual complexes; each dot in (E) represents one analyzed glomerulus; 21 glomeruli from 1 *Parva* WT and 22 glomeruli from 1 *Parva* KO animal were quantified).

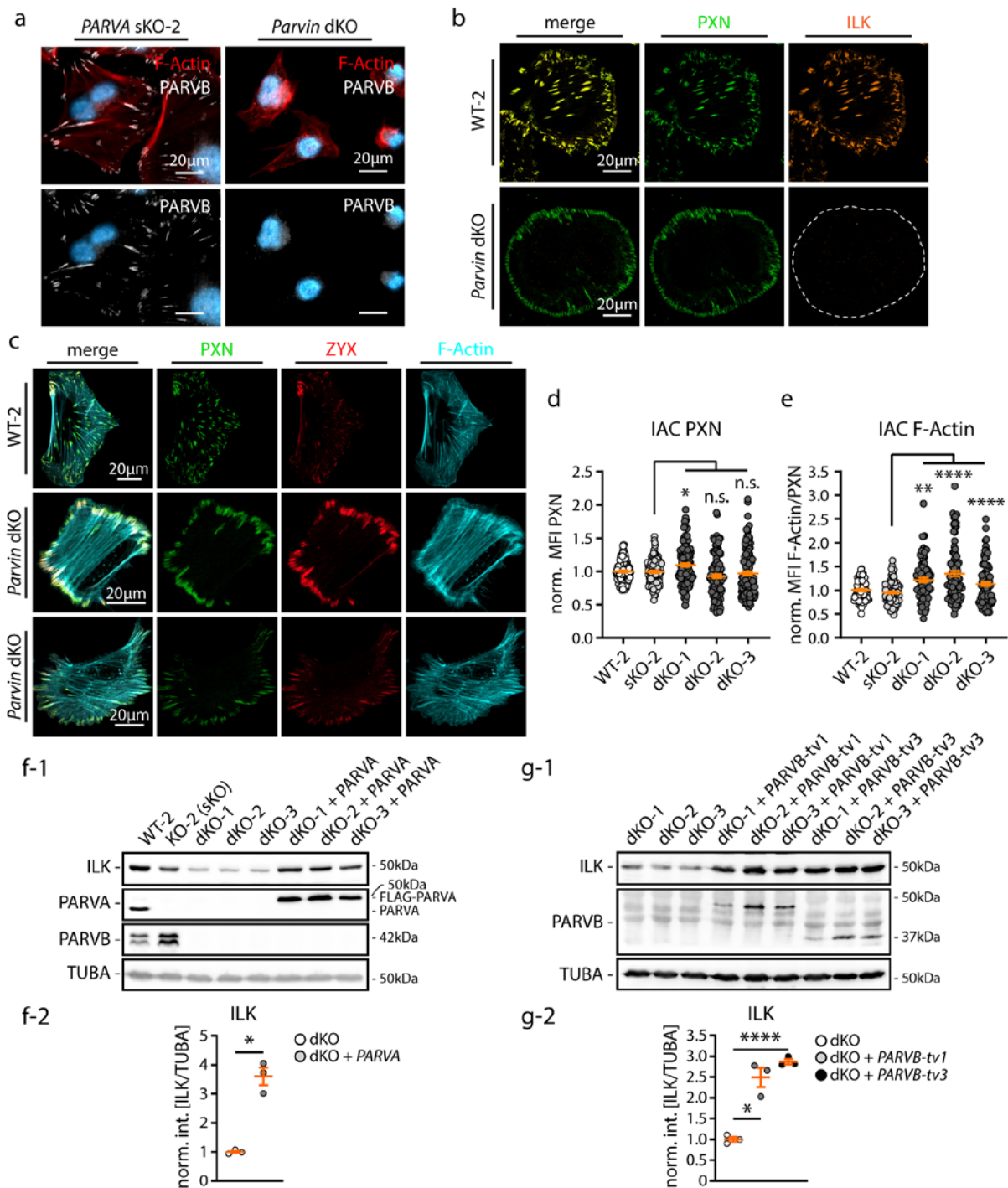


Figure S9. Additional data corresponding to main Figure 6. **(A)** Immunofluorescence staining for PARVB in either *PARVA* single (sKO-2) or *PARVA* and *PARVB* double knockout (dKO) podocytes demonstrated efficient deletion of *PARVB* in sequentially deleted cells. **(B)** Representative immunofluorescence images showed a pronounced IAC class switch characterized by loss of ILK from IACs as well as internal IACs (stained with PXN), while peripheral IACs were still detectable in dKO cells (dotted line indicates the outline of the depicted cell in the ILK staining channel). **(C)** Immunofluorescence microscopy demonstrated increased recruitment of ZYX towards peripheral IACs accompanied by a diffuse actin cytoskeleton with only sparse actin stress fibers. **(D&E)** Quantitative analysis of mean fluorescence intensities (MFIs) demonstrated increased levels of F-Actin recruitment towards IACs in dKO cells, whereas *PARVA* sKO cells did not show this phenotype. (Dots indicate analyzed cells; 4 independent replicates were analyzed for IAC Paxillin (PXN) MFIs and 3 independent replicates for IAC F-Actin (Phalloidin) MFIs; 30 cells per clone and replicate were analyzed, total of 120 (PXN) or 90 (F-Actin) cells per clone; MFIs were normalized to WT). **(F&G)** Re-expression of a flag-tagged version of *PARVA* or *PARVB* transcript variants -1 or -3 (tv1 or tv3) in dKO cells restored ILK protein levels (TUBA – tubulin

alpha was used as a loading control; dots represent western blot analysis of individual cell clones; int. – intensity, norm. – normalized to WT intensity). * $p < 0.05$, ** * $p < 0.01$ and **** $p < 0.0001$, n. s. – non-significant.

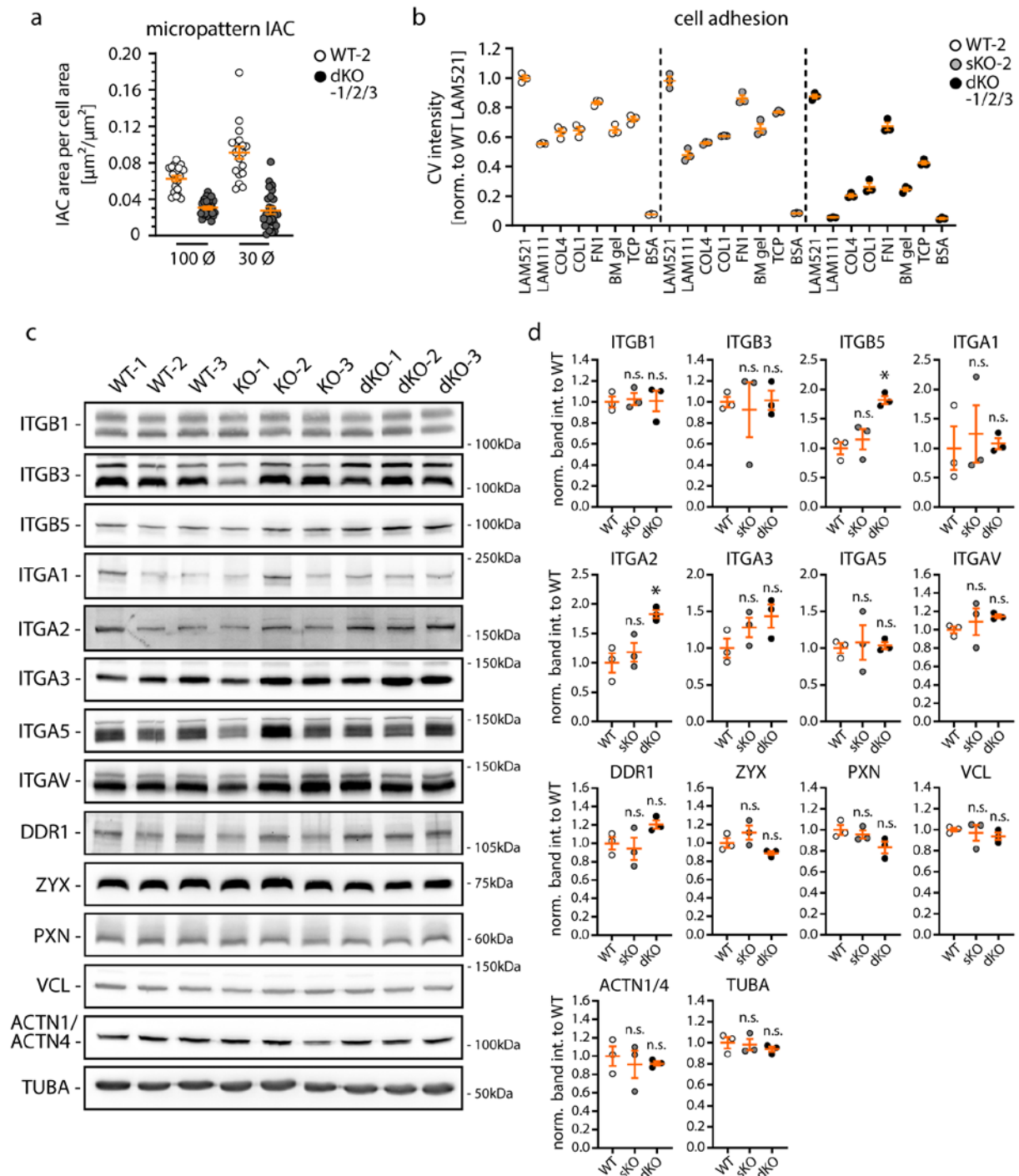


Figure S10. Additional data corresponding to main Figure 6&7. **(A)** Analysis of podocytes on micropatterned surfaces related to main Figure 6I. Morphometric quantification confirmed significantly reduced IAC areas related to the provided adhesion areas (at least 19 cells per condition were analyzed). **(B)** Alternative analysis of adhesion assay data presented in main Figure 7B. *PARVA* and *PARVB* double KO-1/2/3 (dKO) podocytes showed reduced cell adhesion on specific ECM ligands (each dot presents one independent replicate per genotype, relative numbers of adherent cells were determined by crystal violet - CV staining). Experiments were normalized to WT on LAM521. **(C&D)** Western blot analysis of Integrin receptors and IAC components expression in whole cell lysates of WT (WT1-3), *PARVA* KO (KO1-3) as well as *PARVA* and *PARVB* dKO (dKO1-3) podocytes showed no concordant regulation (dots represent western blot analysis of individual cell lines; int. – intensity, norm. – normalized to WT intensity). Statistical testing compares sKO to WT and dKO to WT, * $p < 0.05$, n. s. – non-significant.

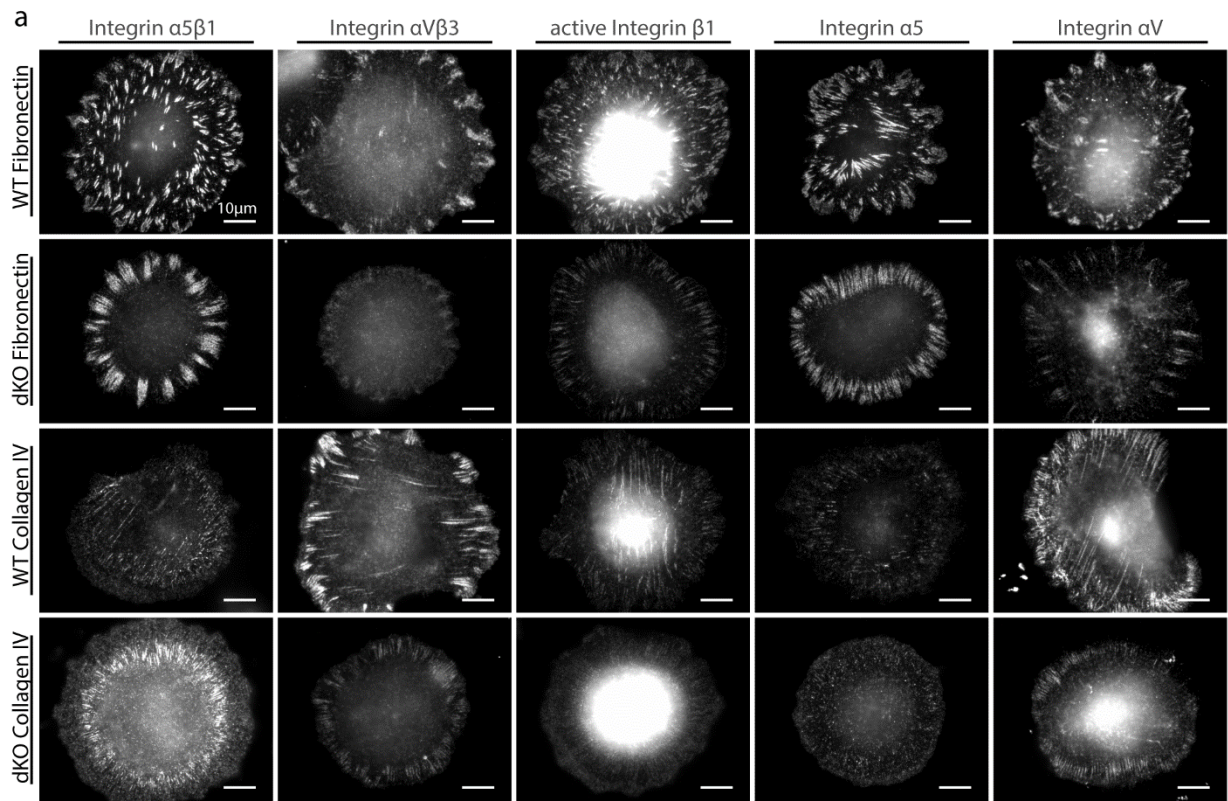


Figure S11. Additional data corresponding to main Figure 7. **(A)** Representative staining of Integrin $\alpha 5 \beta 1$ heterodimers, Integrin $\alpha V \beta 3$ heterodimers, active Integrin $\beta 1$, Integrin $\alpha 5$ and Integrin αV in WT-2 and dKO-1 podocytes seeded on Fibronectin or Collagen IV coated surfaces for 60 minutes. *PARVA* and *PARVB* dKO-1 podocytes showed a strong reduction of internal integrin adhesions and overall reduced recruitment of integrin receptors to adhesion sides.

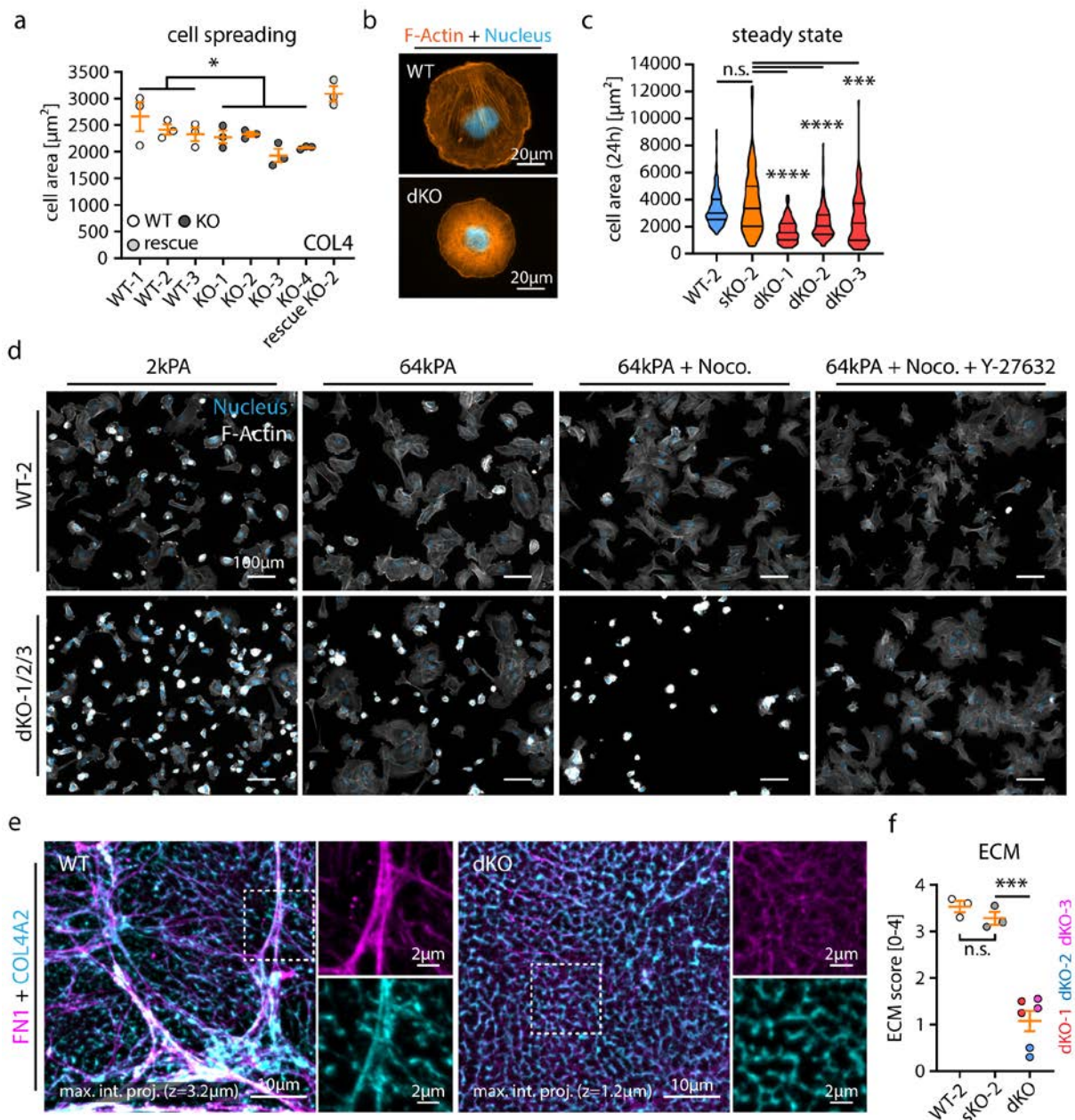


Figure S12. Additional data corresponding to main Figure 7. **(A)** Cell spreading analysis of several independent *PARVA* WT and single knockout (sKO) clones showed only minimal differences to respective controls on Collagen IV (COL4). Re-expression of *PARVA* in KO-2 cells resulted in slight hyper-compensation (each dot presents the mean spread cell size of one independent experiment per clone; WT and KO clones were combined for statistical analysis). **(B)** Immunofluorescence analysis showed no obvious alterations of cell morphology, protrusion formation or polarity of *PARVA* and *PARVB* double KO (dKO) podocytes during cell spreading (IF analysis corresponding to main Figure 7c; Hoechst 33258 stain was used as a counterstain for cell nuclei and F-Actin was visualized by Phalloidin staining). **(C)** Under steady state conditions, independent dKO clones showed reduced cell areas compared to WT-2 cells and sKO-2 podocytes (at least 133 cells per clone were analyzed; data are presented as violin plots). **(D)** Percentage of cells in a rounded and partially detached state is strongly influenced by extra- and intracellular mechanical cues. Representative overview images of WT-2 and dKO-1/2/3 cells on substrates with different rigidities and additional treatment with Nocodazol and Y-27632 (IF staining corresponding to main Figure 7F&G; Hoechst 33258 stain was used as a counterstain for cell nuclei and F-Actin was stained by Phalloidin). **(E&F)** Immunofluorescence microscopy demonstrated impaired ECM network density in dKO-1/2/3 cells (maximum intensity projections of de-cellularized cell-derived-matrices (CDM); dashed white boxes indicate zoom-in areas for individual ECM stainings; Fibronectin (FN1) and Collagen IV (COL4A2)). Semi-quantitative ECM-

scoring confirmed reduced ECM assembly in respective dKO cells compared to control and single knockout (sKO) clones (each dot presents individual replicates per genotype derived from two independent experiments; individual dKO clones are color-coded). * $p < 0.05$, *** $p < 0.001$ and **** $p < 0.0001$, n. s. – non-significant.

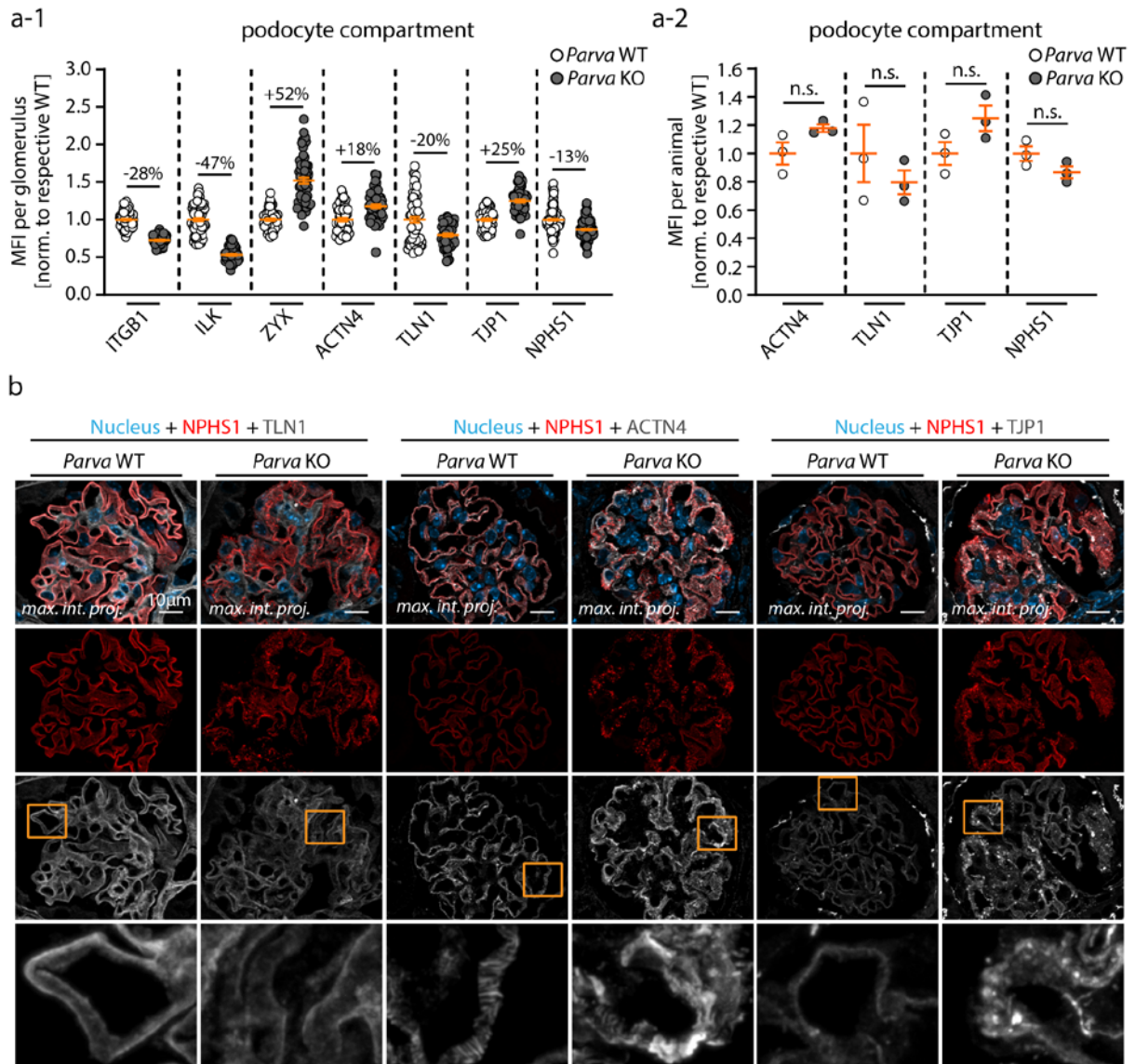


Figure S13. Additional data corresponding to main Figure 5&8. **(A&B)** Immunofluorescence analysis demonstrated altered signal patterns and intensity levels for adhesion related proteins such as ITGB1, ILK, ZYX, ACTN4, TLN1 or cell-cell contact proteins TJP1 as well as NPHS1 in *Parva* deficient podocytes at 10 weeks of age. (mean fluorescence intensity (MFI) was normalized to WT; NPHS1 was used for segmentation of the podocyte compartment; dots in A-1 present individual assessed glomeruli for 3 WT and 3 KO animals; dots in A-2 present mean values for individual assessed animals; at least 20 glomeruli per animal were analyzed). Orange boxes indicate zoom-in regions. Data for ITGB1, ILK and ZYX were presented in main Figure 5&8 as mean value per analyzed animal. n.s. - non-significant.

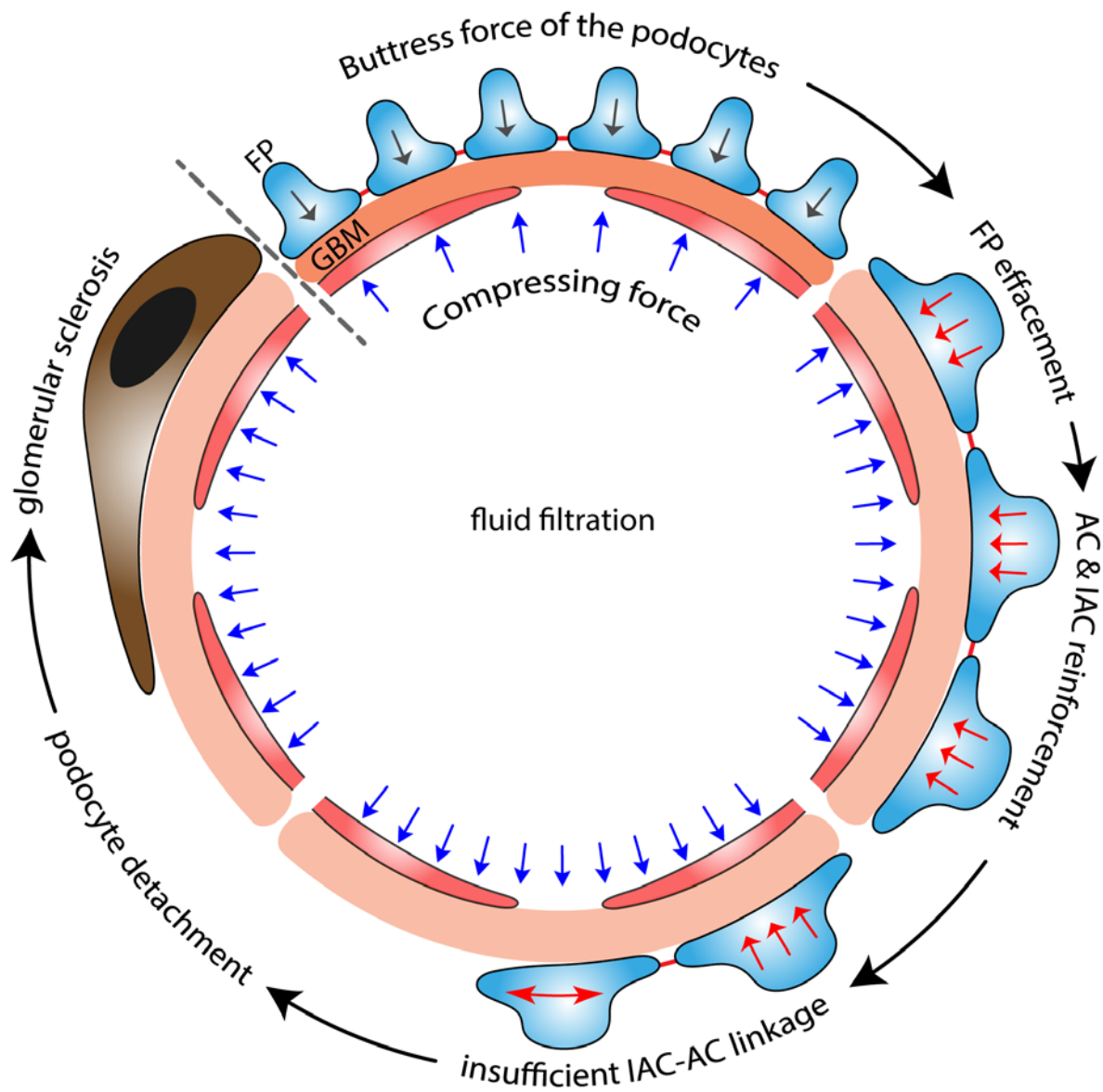


Figure S14. Schematic: impaired mechano-linkage at IACs results in podocyte detachment in glomerular disease. Insufficient integrin adhesion complex (IAC) to actin cytoskeleton (AC) linkage in podocyte disease lead to disturbed and misdirected transduction of contractile mechanical forces. Blue arrows indicate compressing forces of the fluid filtration and to the glomerular basement membrane (GBM). Dark gray and red arrows indicate buttress forces towards the GBM by healthy (gray) or diseased (red) podocytes. FP – podocyte foot processes.

Table S1. Antibodies

Primary Antibodies

Protein	Species	ID	Manufacturer	human FFPE sections	murine FFPE sections	cell IF	WB	external AB validation	KO/KD validated
ACTA2 (SMA)	mouse IgG2a, kappa	GA611	Dako	HIAR Tris-EDTA pH9; ready to use dilution				Manufacturer; in vitro diagnostic certification (CE-IVD)	
ACTB	mouse	A5441	Sigma-Aldrich/Merck KGaA	HIAR Tris-EDTA pH9; 1:400	HIAR Tris-EDTA pH9; 1:500	HIAR Tris-EDTA pH9; 1:600		referenced in >8900 publications; 4i - PMID: 34203913	
ACTN1/4 (alpha-Actinin-1, -2, -4)	mouse	sc-166524	Santa Cruz				1:1000	Manufacturer; referenced in >17 publications	
ACTN4	rabbit	ab108198	Abcam	HIAR Tris-EDTA pH9; 1:400	HIAR Tris-EDTA pH9; 1:400	1:600		Manufacturer; PMID: 32737144	https://www.abcam.com/alp-ha-actinin-4-antibody-epr25332-ab108198.html
AIF1L	rabbit	HPA020522	Atlas Antibodies	HIAR Citrat pH6; 1:100				Human Protein Atlas; PMID: 30001384	PMID: 30001384; PMID: 32107417
CD11c	rabbit	#97585	Cell Signaling		HIAR Tris-EDTA pH9; 1:150			Manufacturer; referenced in >10 publications; PMID: 31315923; 4i - PMID: 34203913	
CD151	rabbit	HPA011906	Atlas Antibodies	HIAR Tris-EDTA pH9; 1:200				Human Protein Atlas; PMID: 29138120	
CD34	mouse	M7165	Dako		HIAR Tris-EDTA pH9; 1:150			Manufacturer; in vitro diagnostic certification (CE-IVD)	
CD3e	rabbit	#99940	Cell Signaling		HIAR Tris-EDTA pH9; 1:250			Manufacturer; referenced in >10 publications; PMID: 31792381; PMID: 32727899; 4i - PMID: 34203913	
CD4	rabbit	#25229	Cell Signaling		HIAR Tris-EDTA pH9; 1:150			Manufacturer; referenced in >20 publications; PMID: 31792381; PMID: 32727899; PMID: 34099645; 4i - PMID: 34203913	
CD8α	rabbit	#98941	Cell Signaling		HIAR Tris-EDTA pH9; 1:150			Manufacturer; referenced in >70 publications; PMID: 31511695; PMID: 31792381; PMID: 32727899; PMID: 30918400; 4i - PMID: 34203913	
CLDN1	rabbit	ab15098	Abcam	HIAR Tris-EDTA pH9; 1:100				Manufacturer; referenced in >150 publications	
Cleaved Caspase-3 (Asp175)	rabbit	#9661	Cell Signaling		HIAR Citrat pH6; 1:200			Manufacturer; referenced in >6900 publications	
COL4A1	rabbit	ab6586	Abcam		HIAR Tris-EDTA pH9; 1:200			Manufacturer; referenced in >700 publications; PMID: 24436468	
COL4A2	mouse IgG1	MAB1910	Merck Millipore	HIAR Tris-EDTA pH9; 1:200		1:500		referenced in >30 publications	
CORO2B	rabbit	HPA017960	Atlas Antibodies	HIAR Tris-EDTA pH9; 1:300				Human Protein Atlas; PMID: 29162887	PMID: 29162887

DDR1 (Total-DDR1)	rabbit	#5583	Cell Signaling					1:1000	Manufacturer; referenced in >32 publications	PMID: 34893587
DES	mouse IgG1	M0760	Dako		HIAR Tris-EDTA pH9; 1:200				Manufacturer; in vitro diagnostic certification (CE-IVD); 4i - PMID: 34203913	
EHD3	rabbit	HPA049986	Atlas Antibodies	HIAR Tris-EDTA pH9; 1:400					Human Protein Atlas	
ENAH	rabbit	HPA028448	Atlas Antibodies	HIAR Tris-EDTA pH9; 1:200					Human Protein Atlas	PMID: 34854809
EPB41L5	rabbit	HPA037564	Atlas Antibodies	HIAR Tris-EDTA pH9; 1:300					Human Protein Atlas; PMID: 33761352; PMID: 28536193	PMID: 33761352; PMID: 28536193
F4/80	rabbit	70076	Cell Signaling		HIAR Tris-EDTA pH9; 1:400				Manufacturer; referenced in >80 publications; PMID: 31511695; PMID: 31315923; PMID: 30918400; 4i - PMID: 34203913	
FBLIM1	rabbit	HPA025287	Atlas Antibodies	HIAR Tris-EDTA pH9; 1:200					Human Protein Atlas	PMID: 29114925
FERMT2	rabbit	HPA040505	Atlas Antibodies	HIAR Tris-EDTA pH9; 1:200	HIAR Tris-EDTA pH9; 1:200				Human Protein Atlas	PMID: 29337051
FHL2	rabbit	HPA006028	Atlas Antibodies	HIAR Tris-EDTA pH9; 1:300	HIAR Tris-EDTA pH9; 1:300				Human Protein Atlas	PMID: 27742790
FLAG M2	mouse	F3165	Sigma-Aldrich/Merck KGaA					1:3000	Manufacturer; referenced in >8000 publications	
FLNA	rabbit	ab51217	Abcam	HIAR Tris-EDTA pH9; 1:200					Manufacturer; PMID: 33860543	
FN1	rabbit	A0245	Dako		HIAR Tris-EDTA pH9; 1:500	HIAR Tris-EDTA pH9; 1:200	HIAR Tris-EDTA pH9; 1:200	1:1000	Manufacturer; in vitro diagnostic certification (CE-IVD)	
ILK	rabbit	#3862	Cell Signaling	HIAR Tris-EDTA pH9; 1:200	HIAR Tris-EDTA pH9; 1:200	HIAR Tris-EDTA pH9; 1:200		1:1000	Human Protein Atlas; referenced in >40 publications	PMID: 30254023
ITGA1	mouse IgG1	AMAb91460	Atlas Antibodies					1:1000	Human Protein Atlas	https://www.atlasantibodies.com/products/antibodies/primary-antibodies/precisamonoclonals/itga1-antibody-amab91460/
ITGA2	rabbit	AB1936	Merck Millipore					1:1000	Manufacturer; referenced in >49publications	PMID: 20592186
ITGA3	rabbit	HPA008572	Atlas Antibodies	HIAR Tris-EDTA pH9; 1:300				1:1000	Human Protein Atlas	PMID: 28415821
ITGA5	mouse IgG2b	AMAb91449	Atlas Antibodies					1:1000	Human Protein Atlas	https://www.atlasantibodies.com/products/antibodies/primary-antibodies/precisamonoclonals/itga5-antibody-amab91449/
ITGA5 clone mAb11	rat	MABT822	Merck Millipore				1:100		Manufacturer	
ITGAV	rabbit	ab179475	Abcam	HIAR Tris-EDTA pH9; 1:200	HIAR Tris-EDTA pH9; 1:300			1:1000	Manufacturer; referenced in >40 publications; PMID: 33859325	
ITGAV	rabbit	HPA004856	Atlas Antibodies				1:100		Human Protein Atlas	

ITGAVB3	mouse	MAB1976	Merck Millipore			1:100		Referenced in >432 publications; PMID: 28783156; PMID: 28592635	
ITGB1	mouse IgG1	#610467	BD Biosciences	HIAR Tris-EDTA pH9; 1:300	HIAR Tris-EDTA pH9; 1:200		1:1000	referenced in >80 publications	PMID: 23863477
ITGB1 (CD29) Clone 9EG7	rat	553715	BD Pharmingen			1:100		Referenced in >185 publications; PMID: 32004443, PMID: 33558312	
ITGB3	rabbit	#13166S	Cell Signaling	HIAR Tris-EDTA pH9; 1:200	HIAR Tris-EDTA pH9; 1:200		1:1000	Manufacturer; referenced in >40 publications; PMID: 32709711	PMID: 32709711
ITGB5	rabbit	HPA001820	Atlas Antibodies	HIAR Citrat pH6; 1:200				Human Protein Atlas	
ITGB5	rabbit	#3629	Cell Signaling				1:1000	Manufacturer; referenced in >20 publications;	
LAMA5	mouse IgG1	AMAb91124	Atlas Antibodies	HIAR Tris-EDTA pH9; 1:200				Human Protein Atlas	https://www.atlasantibodies.com/products/antibodies/primary-antibodies/precisamonoclonals/lama5-antibody-amab91124/
LAMB2	mouse	AMAb91097	Sigma-Aldrich/Merck KGaA	HIAR Tris-EDTA pH9; 1:200				Human Protein Atlas	
LAMC1	rabbit	ab233389	Abcam	HIAR Tris-EDTA pH9; 1:400	HIAR Tris-EDTA pH9; 1:400			Manufacturer; PMID: 30810063; PMID: 32076639	
LASP1	rabbit	HPA012072	Atlas Antibodies	HIAR Tris-EDTA pH9; 1:200				Human Protein Atlas	
LIMS2	rabbit	HPA058340	Atlas Antibodies	HIAR Citrat pH6; 1:200				Human Protein Atlas	
LPP	rabbit	HPA017342	Atlas Antibodies	HIAR Tris-EDTA pH9; 1:200				Human Protein Atlas	
MYH9	rabbit	PRB-440P; 909801	Covance; BioLegend	HIAR Tris-EDTA pH9; 1:400		HIAR Tris-EDTA pH9; 1:600		PMID: 28993503; PMID: 33506761	PMID: 34374341
NPHS1	guinea pig	GP-N2	Progene	HIAR Tris-EDTA pH9; 1:300	HIAR Tris-EDTA pH9 or Citrat pH6; 1:400			Manufacturer; referenced in >140 publications; PMID: 30425988	
NPHS2	rabbit	P0372	Sigma-Aldrich/Merck KGaA	HIAR Tris-EDTA pH9; 1:400				Manufacturer; referenced in >110 publications; PMID: 19917779; PMID: 26802179; PMID: 27350175	
PARVA	rabbit	#4026	Cell Signaling	HIAR Tris-EDTA pH9; 1:200	HIAR Tris-EDTA pH9; 1:200	HIAR Tris-EDTA pH9; 1:150	1:500	Manufacturer	This study
PARVB	rabbit	PA5-89039	Invitrogen	HIAR Tris-EDTA pH9; 1:100	HIAR Tris-EDTA pH9; 1:100			Manufacturer	
PARVB (OTI1B7)	mouse	NBP2-46327	Novus Biologicals			1:150	1:1000	Manufacturer	This study
PCNA	mouse	M0879	Dako		HIAR Tris-EDTA pH9; 1:400			Manufacturer; referenced in >500 publications; 4i - PMID: 34203913	
PDLIM5	rabbit	HPA016740	Atlas Antibodies	HIAR Tris-EDTA pH9; 1:200		HIAR Tris-EDTA pH9; 1:150		Human Protein Atlas	PMID: 30404826; PMID: 28045035; PMID: 33761352

PDLM7	rabbit	HPA018794	Atlas Antibodies	HIAR Citrat pH6; 1:100				Human Protein Atlas	
phospho-S6 Ribosomal Protein (Ser235/236)	rabbit	#2211	Cell Signaling		HIAR Tris-EDTA pH9; 1:200			Manufacturer; referenced in >900 publications; 4i - PMID: 34203913	
PTK2 (FAK)	rabbit	06-543	Upstate/Millipore	HIAR Tris-EDTA pH9; 1:200				referenced in >70 publications; PMID: 28348210; PMID: 29249464; PMID: 22270917	PMID: 19297531
PXN	mouse IgG1	#610051	BD Biosciences	HIAR Tris-EDTA pH9; 1:200		native or HIAR Tris-EDTA pH9; 1:300	1:1000	referenced in >180 publications; PMID: 26821125; PMID: 28202690	
SRGAP1	rabbit	13252-I-AP	Proteintech	HIAR Tris-EDTA pH9; 1:300				PMID: 33514561	PMID: 33514561
SYNPO	mouse IgG1	#65194	Progene	HIAR Tris-EDTA pH9; 1:200				Manufacturer; PMID: 32188698; PMID: 30425988	
TGM2	rabbit	HPA021019	Atlas Antibody	HIAR Citrat pH6; 1:100				Human Protein Atlas; PMID: 28198360	
TJP1 (ZO-1)	rat IgG2a	sc-33725	Santa Cruz		HIAR Tris-EDTA pH9; 1:100			referenced in >100 publications; PMID: 31025935	
TJP1 (ZO-1) (D6L1E)	rabbit	#13663	Cell Signaling	HIAR Citrat pH6; 1:200				Manufacturer; referenced in >40 publications	
TLN1	mouse IgG1	T3287	Sigma-Aldrich/Merck KGaA	HIAR Tris-EDTA pH9; 1:200	HIAR Tris-EDTA pH9; 1:150			PMID: 33860543	PMID: 23977051
TNS1	rabbit	HPA036089	Atlas Antibodies	HIAR Tris-EDTA pH9; 1:200				Human Protein Atlas	https://www.atlasantibodies.com/products/antibodies/primary-antibodies/triple-a-polyclonals/tns1-antibody-hpa036089/
TNS2	rabbit	HPA034659	Atlas Antibodies	HIAR Tris-EDTA pH9; 1:200				Human Protein Atlas	PMID: 28955049
TNS3	rabbit	HPA056015	Atlas Antibodies	HIAR Tris-EDTA pH9; 1:200	HIAR Tris-EDTA pH9; 1:200			Human Protein Atlas	
TUBA	mouse IgG1	T9026 (DM1A)	Sigma-Aldrich/Merck KGaA				1:5000	Manufacturer; referenced in >4000 publications	
VASP	rabbit	#3132	Cell Signaling	HIAR Tris-EDTA pH9; 1:200				Manufacturer; referenced in >40 publications	PMID: 30373894
VCL	rabbit	HPA063777	Atlas Antibodies	HIAR Tris-EDTA pH9; 1:300		1:150	1:1000	Human Protein Atlas	https://www.atlasantibodies.com/products/antibodies/primary-antibodies/triple-a-polyclonals/vcl-antibody-hpa063777/?q=HPA063777&t=Z2ZORuUylwiRcnEQZ4Hd8g=#References
VIM	mouse IgG1	#550513	BD Biosciences	HIAR Tris-EDTA pH9; 1:200				referenced in >180 publications	

VLA-5 (ITGA5/ITGB1)	mouse	MAB1999	Merck Millipore			1:100		Referenced in >54 publications; PMID: 28783156; PMID: 28592635
WASL	rabbit	#4848S	Cell Signaling	HIAR Tris-EDTA pH9; 1:200				referenced in >40 publications; PMID: 31668663; PMID: 23471198
WT1	rabbit	ab15249	Abcam		HIAR Citrat pH6; 1:400			Manufacturer; referenced in >30 publications
ZYX	rabbit	HPA004835	Atlas Antibodies	HIAR Tris-EDTA pH9; 1:200	HIAR Tris-EDTA pH9; 1:150	1:100	1:1000	Human Protein Atlas; PMID: 25860875; PMID: 31882643

Secondary Antibodies

Protein	ID	Manufacturer	Application
Alexa Fluor 488 Phalloidin	A12379	Thermo Fisher Scientific	1:200
Alexa Fluor 546 Phalloidin	A22283	Thermo Fisher Scientific	1:200
Hoechst 33342, Trihydrochloride, Trihydrate	H3570	Thermo Fisher Scientific	1:1000
Alexa Fluor 555, Goat anti-Rat IgG	A-21434	Thermo Fisher Scientific	1:500
Alexa Fluor 555, donkey anti-rabbit IgG	A-31572	Thermo Fisher Scientific	1:500
Alexa Fluor 488, goat anti-guinea pig IgG	A-11073	Thermo Fisher Scientific	1:500
Alexa Fluor 555, goat anti-mouse IgG1	A-21127	Thermo Fisher Scientific	1:500
Alexa Fluor 555, donkey anti-mouse IgG	A31570	Thermo Fisher Scientific	1:500
Alexa Fluor 647, goat anti-rabbit IgG	A21245	Thermo Fisher Scientific	1:400
Alexa Fluor 647, goat anti-guinea pig IgG	A-21450	Thermo Fisher Scientific	1:500
Alexa Fluor 647, goat anti-mouse IgG	A-21236	Thermo Fisher Scientific	1:400
Swine Anti-Rabbit Immunoglobulins/HRP	P0217	Dako	IHC 1:500
Goat anti-mouse Immunoglobulins/HRP	P0447	Dako	IHC 1:500; WB 1:10000
Goat anti-rabbit IgG, HRP-linked Antibody	#7074	Cell Signaling	WB 1:5000
Rabbit Anti-Guinea Pig Immunoglobulins/HRP	P0141	Dako	IHC 1:500

Table S2. RNAseq: consensus integrin adhesome & literature-curated adhesome proteins^{1,2}

GeneID	SYMBOL	Base mean counts [only >100]	DESeq2 log2 (FC) Parva KO/WT	P-adj
57342	Parva	4760.5735	-1.70796319	2.5418E-32
18186	Nrp1	21085.1477	-0.81222594	5.2927E-07
50768	Dlc1	4295.48816	-0.67694099	2.4167E-05
15170	Ptpn6	168.956705	1.05817655	3.9063E-05
19122	Prnp	1429.81341	0.88947338	4.7807E-05
16401	Itga4	952.908348	-0.73600388	5.6686E-05
14200	Fhl2	2300.07608	-0.76109712	7.2195E-05
241226	Itga8	6000.62489	-0.75923014	9.5277E-05
104099	Itga9	1033.74222	-0.72927841	0.00013047
19229	Ptk2b	304.121767	1.30165334	0.00013887
244895	Peak1	484.176471	-0.6686128	0.0002058
16420	Itgb6	612.294395	1.26887358	0.00024388
19684	Rdx	4653.16369	-0.38409019	0.00037194
107684	Coro2a	420.491942	-0.74424846	0.0003818
14786	Grb7	458.351556	1.20393157	0.00045696
234214	Sorbs2	1936.77744	-0.62333556	0.00051026
319939	Tns3	11396.5471	-0.62680195	0.00061294
16971	Lrp1	1733.31814	-0.65183862	0.00062585
102866	Pls3	4762.31644	-0.45571309	0.00075618
211914	Asap2	809.219518	-0.70310809	0.00080248
20469	Sipa1	845.325364	-0.64408018	0.00120857
19268	Ptpnf	883.772517	1.2224048	0.00121065
16331	Inpp5d	233.124718	-0.71318672	0.00148706
20779	Src	293.844502	0.59885963	0.00203152
108101	Fermt3	217.166747	-0.75056534	0.00275827
170736	Parvb	482.893073	-0.72000409	0.0033227
16419	Itgb5	8575.1238	-0.6196877	0.0034668
58194	Sh3kbp1	319.960652	-0.59362228	0.00440582
73341	Arhgef6	307.390336	-0.47587412	0.00728867
21817	Tgm2	1570.07165	0.79888295	0.00776824
241639	Fermt1	187.590972	1.07047922	0.00846583
218952	Fermt2	3678.56939	-0.43486803	0.0089387
20411	Sorbs1	1696.29792	-0.33742243	0.01359718
16709	Ktn1	1443.49108	-0.3449138	0.01458154
19248	Ptpn12	1255.82821	-0.40520977	0.01510099
18479	Pak1	3721.81507	-0.62401804	0.01533818
22330	Vcl	2880.37887	-0.47622677	0.01797749
68606	Ppm1f	1010.09979	-0.40794182	0.0214487
14083	Ptk2	1066.61968	-0.31486773	0.02160838
22323	Vasp	1492.66197	-0.40575057	0.02429089
218397	Rasa1	795.095622	-0.32953877	0.02973864
67905	Ppm1m	536.707427	-0.48313618	0.03215779
23897	Hax1	931.444475	0.44719953	0.03403027
110829	Lims1	1684.15184	-0.41362497	0.03681409
58800	Trpm7	1547.77795	0.35336982	0.04511415
17974	Nck2	1163.20799	-0.35827389	0.05384206
18453	P4hb	7716.88037	0.33863796	0.05625536
18763	PKd1	1012.94934	-0.36394761	0.06435734
192176	Flna	4019.30641	-0.42443934	0.06891673
17698	Msn	4519.13516	-0.29500757	0.0764897
16400	Itga3	7161.00307	-0.31249341	0.07660437
19247	Ptpn11	2069.73767	-0.26186045	0.07768291
71302	Arhgap26	517.653526	-0.38166504	0.09833671
11350	Abl1	745.25083	-0.33667266	0.1045778
12928	Crk	2952.40822	-0.20157372	0.12208071
17254	Slc3a2	2564.29509	0.30567571	0.12280253
68810	Nexn	366.453813	-0.40992319	0.12539311
109700	Itga1	430.170492	0.26686436	0.14095021
13430	Dnm2	1758.28223	-0.22279175	0.14341645
18750	Prkca	1191.17951	-0.3473916	0.14878218
20163	Rsu1	1182.25567	-0.29482262	0.1505932
18187	Nrp2	397.87702	-0.39947592	0.15073952
225341	Lims2	1135.69937	-0.22862245	0.15420691
66254	Dimt1	138.542565	-0.36576769	0.16655118
66942	Ddx18	587.6284	-0.22740416	0.17495347
74202	Fblim1	123.497168	-0.51957264	0.17791805

14784	Grb2	1197.91516	-0.18325489	0.20261956
12476	Cd151	5416.2346	-0.26323364	0.21657859
68520	Zfyve21	485.640322	0.24633624	0.21703866
243362	Stard13	163.352171	-0.3650071	0.21809129
16412	Itgb1	15844.2635	-0.19466306	0.22300933
320910	Itgb8	112.401836	0.49913281	0.2259214
16404	Itga7	200.710152	-0.28830257	0.23675786
73826	Poldip3	1072.19893	-0.25604524	0.24289405
11461	Actb	20591.3107	-0.2378461	0.26628966
56403	Syncrip	1661.66881	-0.18966315	0.27124861
16202	Ilk	2877.05254	-0.2124026	0.27136418
12798	Cnn2	1954.02697	-0.27907598	0.28335703
15441	Hp1bp3	2457.96292	-0.177998	0.29614732
21681	Alyref	484.206573	-0.19627073	0.30191185
21753	Tes	296.102017	0.2363034	0.30936964
20409	Ostf1	1872.00845	-0.15710176	0.31160903
18803	Plcg1	474.244134	-0.29377989	0.31728802
23789	Coro1b	1886.59113	-0.15623608	0.32913446
21961	Tns1	6927.76319	0.19113298	0.33015591
16410	Itgav	3164.68123	0.1441385	0.34990951
69902	Mrto4	225.237824	0.20565195	0.34990951
21804	Tgfb1i1	438.148622	-0.21466339	0.37690645
12389	Cav1	1072.05949	-0.14823946	0.39056523
19052	Ppp2ca	3120.93961	0.12590009	0.40333683
20410	Sorbs3	1177.20927	-0.19260885	0.41669514
14201	Fhl3	163.529447	-0.28008085	0.41845889
16413	Itgb1bp1	445.953509	0.17253393	0.42178789
14388	Gab1	695.315656	-0.14458229	0.42965725
72333	Palld	527.655671	-0.1574777	0.47708832
12317	Calr	12342.2365	0.19107004	0.48579143
67399	Pdlim7	378.258405	-0.23016818	0.49328169
230837	Asap3	100.893024	0.23995817	0.49772292
18003	Nedd9	1481.13944	-0.12262778	0.50527348
53378	Sdcbp	2524.77955	-0.09061588	0.53757321
18607	Pdpk1	807.547412	-0.12437186	0.54138754
12988	Csk	823.765607	-0.10595538	0.55420251
67832	Brix1	504.056111	-0.11354983	0.56227993
12631	Cfl1	6424.0218	-0.11477052	0.57421849
22793	Zyx	785.470287	0.16221045	0.58537737
140580	Elmo1	254.25753	-0.21155245	0.60228813
231532	Arhgap24	6832.78496	-0.10303157	0.61283201
13043	Cttn	1706.48587	0.08089441	0.63522624
16796	Lasp1	2849.38203	-0.08656632	0.64138548
29806	Limd1	1010.50659	0.09667592	0.64298849
21894	Tln1	4190.13759	-0.08277291	0.66743487
16402	Itga5	326.70617	-0.14193867	0.67124979
109624	Cald1	8459.74667	-0.12181666	0.67338276
12929	Crkl	338.392565	-0.1521886	0.67870943
60595	Actn4	12989.6307	-0.08952215	0.67950689
109711	Actn1	1164.92072	0.13451918	0.67950689
14156	Fen1	128.133381	0.13896619	0.68123311
16332	Inpp1	1661.20952	-0.07663182	0.68480678
56376	Pdlim5	1317.02634	-0.08292278	0.68493066
216963	Git1	898.376489	-0.07962378	0.69020985
19035	Ppib	3267.73896	0.07599525	0.69334629
26431	Git2	526.710478	-0.08667769	0.69830345
330662	Dock1	804.56482	-0.09167668	0.71483573
50868	Keap1	903.61678	-0.06643362	0.72933506
268656	Sptlc1	862.278611	0.07011132	0.73507916
225115	Svil	356.20007	-0.08382485	0.74517751
52118	Pvr	246.452211	0.08002517	0.74561524
228889	Ddx27	505.33197	-0.06815663	0.74957461
81489	Dnajb1	605.3283	0.0882712	0.76258529
20848	Stat3	1326.18834	-0.06472347	0.76614078
22350	Ezr	6205.22594	0.05172029	0.77383732
12927	Bcar1	1552.58079	0.04735821	0.77614666
29875	Iqgap1	3111.45529	0.04637359	0.82430797
238871	Pde4d	366.528914	-0.09282208	0.82468598
14109	Fau	3447.22191	0.0514832	0.82884676
210126	Lpp	1034.04667	-0.04723014	0.82894515

13800	Enah	334.547896	0.0493594	0.84654295
66911	Nudt16l1	716.040713	0.04229223	0.86143298
83431	Ndel1	1533.55698	0.03197235	0.86559377
71766	Raver1	611.405179	-0.04525463	0.86718619
22051	Trip6	812.189521	0.03279988	0.89118082
19262	Ptpa	2008.23546	-0.02416944	0.89151871
20399	Sh2b1	723.190262	0.02934029	0.89942596
20971	Sdc4	16279.3075	-0.0290581	0.90558943
268449	Rpl23a	3205.07701	0.02381264	0.91156847
18016	Nf2	1316.28775	-0.01936463	0.92540603
16403	Itga6	618.64444	-0.04067243	0.92574878
54126	Arhgef7	991.914285	0.01830341	0.93451996
16952	Anxa1	4211.15128	0.01741756	0.96972538
67733	Itgb3bp	135.463726	-0.01001518	0.97802312
233977	Ppfia1	798.658012	0.00638091	0.97877225
19303	Pxn	479945.138	0.52352664	NA

1. Horton, E., Byron, A., Askari, J. et al. Definition of a consensus integrin adhesome and its dynamics during adhesion complex assembly and disassembly. *Nat Cell Biol* 17, 1577–1587 (2015).

2. Winograd-Katz SE, Fässler R, Geiger B, Legate KR. The integrin adhesome: from genes and proteins to human disease. *Nat Rev Mol Cell Biol*. 2014 Apr;15(4):273-88.

Table S2. Additional data corresponding to main Figure 5. RNA-sequencing of glomeruli from 8-9 weeks old animals with starting proteinuria was performed and filtered for podocyte-adhesome genes (Analysis for 3 wild type and 3 Parva knockout animals is shown).

Table S3. Correlation analysis

		Spearman's correlation									
Spearman-Rho		CDKN1C	DACH1	NPHS1	PODXL	PTPRO	WT1	NPHS2	SYNPO	PARVB	PARVA
PARVB	correlation coefficient	-0.199**	-0.399**	-0.229**	-0.291**	-0.165*	-0.384**	-0.110	-0.016	1.000	-0.173*
	Sig. (2-sided)	0.004	0.000	0.001	0.000	0.016	0.000	0.112	0.819		0.012
	N	211	211	211	211	211	211	211	211	211	211
	Bootstrap ^c distortion	0.001	-0.002	-0.003	-0.002	-0.002	-0.001	-0.004	0.000	0.000	-0.004
	standard error	0.067	0.059	0.066	0.063	0.069	0.061	0.070	0.074	0.000	0.068
	95% CI minus	-0.324	-0.519	-0.353	-0.411	-0.297	-0.505	-0.259	-0.162	1.000	-0.312
plus	-0.073	-0.288	-0.100	-0.162	-0.030	-0.271	0.020	0.123	1.000	-0.047	
PARVA	correlation coefficient	0.597**	0.262**	0.560**	0.525**	0.621**	0.498**	0.377**	0.460**	-0.173*	1.000
	Sig. (2-sided)	0.000	0.000	0.000	0.000	0.000	0.000	0.000	0.000	0.012	
	N	211	211	211	211	211	211	211	211	211	211
	Bootstrap ^c distortion	0.000	-0.001	-0.001	-0.003	-0.003	-0.003	-0.001	-0.002	-0.004	0.000
	standard error	0.051	0.066	0.051	0.054	0.046	0.055	0.065	0.057	0.068	0.000
	95% CI minus	0.488	0.123	0.459	0.406	0.526	0.381	0.247	0.342	-0.312	1.000
plus	0.691	0.384	0.659	0.623	0.706	0.601	0.498	0.565	-0.047	1.000	

** .significance level < 0,01

*.significance level < 0,05

c. if not stated otherwise, bootstrapping was applied to obtain 1000 times resampling

Table S3. Additional analysis corresponding to main Figure 1. Decrease of PARVA and increase of PARVB significantly correlated with podocyte damage assessed by decrease of specific marker genes. Correlation analyses were performed using spearman correlations. Bootstrapping was applied to obtain 1000 times resampling and derive the corresponding 95% confidence interval for the correlation coefficient. A p-value below 0.05 was considered to be statistically significant.

Table S4. Statistical Methods

Statistical Methods		
Figure panel	Unit of analysis	Statistical tests
Figure 1d	human samples	see methods
Figure 2c	animals animals per timepoint	Kruskal-Wallis test Dunn's multiple comparisons test
Figure 2e	animals per timepoint	Mann Whitney test
Figure 2g	animals KO timepoints vs pooled ctrl.	Kruskal-Wallis test Dunn's multiple comparisons test
Figure 2h	animals animals per timepoint	Kruskal-Wallis test Dunn's multiple comparisons test
Figure 2i	animals animals per timepoint	Kruskal-Wallis test Dunn's multiple comparisons test
Figure 2j	animals animals per timepoint	Kruskal-Wallis test Dunn's multiple comparisons test
Figure 3c	animals	Unpaired t test with Welch's correction
Figure 3d	glomeruli	Mann Whitney test
Figure 3e	glomeruli	Mann Whitney test
Figure 3j	animals 8w animals 10w animals 12w	Unpaired t test Unpaired t test with Welch's correction Unpaired t test with Welch's correction
Figure 3k	animals 8w animals 10w animals 12w	Unpaired t test Unpaired t test Unpaired t test with Welch's correction
Figure 4c	ILK: cell clones PARVB: cell clones; 2 replicates	Unpaired t test with Welch's correction Unpaired t test with Welch's correction
Figure 4e	ILK: cell clones PARVB: cell clones	Unpaired t test with Welch's correction Unpaired t test
Figure 4g	IAC density: pooled cells WT vs KO clones IAC mean area: pooled cells WT vs KO clones IAC MFI ILK/PXN: pooled cells WT vs KO clones IAC MFI PARVB/VCL: pooled cells WT vs KO clones	Unpaired t test Unpaired t test Unpaired t test Unpaired t test with Welch's correction
Figure 5b	animals per timepoint	Unpaired t test with Welch's correction
Figure 5c	glomeruli	-
Figure 5d&e	animals	DESeq2; see methods
Figure 5g	pooled WT & KO pre-prot. vs KO prot.	Unpaired t test with Welch's correction
Figure 6c	cell clones cell clones	Ordinary one-way ANOVA Tukey's multiple comparisons test
Figure 6d	cells cells	Brown-Forsythe ANOVA test Dunnett's T3 multiple comparisons test
Figure 6f-1	cells cells	Ordinary one-way ANOVA Dunnett's multiple comparisons test
Figure 6f-2	cells cells	Brown-Forsythe ANOVA test Games-Howell's multiple comparisons test
Figure 6g-1	cells cells	Ordinary one-way ANOVA Dunnett's multiple comparisons test
Figure 6g-2	cells cells	Brown-Forsythe ANOVA test Games-Howell's multiple comparisons test
Figure 6j-1	cells cells	Brown-Forsythe ANOVA test Games-Howell's multiple comparisons test
Figure 6j-2	cells cells	Brown-Forsythe ANOVA test Games-Howell's multiple comparisons test
Figure 7a	cell clones; 3 replicates per clone cell clones; 3 replicates per clone	Ordinary one-way ANOVA Dunnett's multiple comparisons test
Figure 7b	cell clones; 3 replicates per clone; sKO vs dKO	Unpaired t test with Welch's correction
Figure 7c	cell clones; 3 replicates per clone cell clones; 3 replicates per clone	Brown-Forsythe ANOVA test Games-Howell's multiple comparisons test
Figure 7d	cells	Unpaired t test
Figure 7g	cell clones; 3 replicates per clone and exp. condition cell clones; 3 replicates per clone and exp. condition	Two-way ANOVA Tukey's multiple comparisons test
Figure 8b	animals 10w	Unpaired t test with Welch's correction
Figure 8d	glomeruli	-
Figure 8e	human samples	see methods

Figure S5e	animals 8w animals 10w animals 12w	Unpaired t test with Welch's correction Unpaired t test with Welch's correction Unpaired t test with Welch's correction
Figure S5f	animals 8w animals 10w animals 12w	Unpaired t test Unpaired t test with Welch's correction Unpaired t test with Welch's correction
Figure S6c	IAC MFI PXN: pooled cells WT vs KO clones IAC MFI VCL: pooled cells WT vs KO clones IAC MFI PARVB: pooled cells WT vs KO clones IAC MFI ILK: pooled cells WT vs KO clones	Unpaired t test with Welch's correction Unpaired t test with Welch's correction Unpaired t test with Welch's correction Unpaired t test with Welch's correction
Figure S7c	animals animals	Two-way ANOVA Sidak's multiple comparisons test
Figure S7d	animals	Unpaired t test
Figure S7e	animals	Unpaired t test with Welch's correction
Figure S7f	pooled cells WT vs KO animals	Unpaired t test
Figure S7g	animals	Unpaired t test
Figure S7h	animals	Unpaired t test with Welch's correction
Figure S7i	animals	Unpaired t test
Figure S7j	animals	Unpaired t test
Figure S7k	animals	Unpaired t test with Welch's correction
Figure S7l	animals animals WT vs KO per size class	Brown-Forsythe ANOVA test Dunnett's T3 multiple comparisons test
Figure S7m	cells cells	Ordinary one-way ANOVA Tukey's multiple comparisons test
Figure S7n	animals	Unpaired t test
Figure S8a	glomeruli	-
Figure S8b	glomeruli	-
Figure S8c	glomeruli	-
Figure S8e	glomeruli	-
Figure S9d	cells cells	Brown-Forsythe ANOVA test Games-Howell's multiple comparisons test
Figure S9e	cells cells	Brown-Forsythe ANOVA test Games-Howell's multiple comparisons test
Figure S9f-2	cell clones	Unpaired t test with Welch's correction
Figure S9g-2	cell clones cell clones	Brown-Forsythe ANOVA test Dunnett's T3 multiple comparisons test
Figure S10a	cells	-
Figure S10b	cell clones; 3 replicates per clone	-
Figure S10d	cell clones cell clones	Brown-Forsythe ANOVA test Dunnett's T3 multiple comparisons test
Figure S12a	pooled WT vs KO cell clones; 3 replicates per clone	Unpaired t test
Figure S12c	cells cells	Brown-Forsythe ANOVA test Games-Howell's multiple comparisons test
Figure S12f	cell clones cell clones	Brown-Forsythe ANOVA test Dunnett's T3 multiple comparisons test
Figure S13a	animals	Unpaired t test with Welch's correction